Title: LASER INTERFERENCE LITHOGRAPHY FOR APPLICATIONS IN BIOMEDICINE

Name: Wenjun LI

LASER INTERFERENCE LITHOGRAPHY FOR APPLICATIONS IN BIOMEDICINE

Wenjun LI

Ph.D

2018

UNIVERSITY OF BEDFORDSHIRE

LASER INTERFERENCE LITHOGRAPHY FOR APPLICATIONS IN BIOMEDICINE

by

Wenjun LI

A thesis submitted to the University of Bedfordshire in partial fulfilment of the requirements for the degree of Doctor of Philosophy

October 2018

Declaration Of Authorship

I, Wenjun LI declare that this thesis and the work presented in it are my own and has been generated by me as the result of my own original research.

[Laser interference lithography for applications in biomedicine]

I confirm that:

1. This work was done wholly or mainly while in candidature for a research degree at this University;
2. Where any part of this thesis has previously been submitted for a degree or any other qualification at this University or any other institution, this has been clearly stated;
3. Where I have cited the published work of others, this is always clearly attributed;
4. Where I have quoted from the work of others, the source is always given. With the exception of such quotations, this thesis is entirely my own work;
5. I have acknowledged all main sources of help;
6. Where the thesis is based on work done by myself jointly with others, I have made clear exactly what was done by others and what I have contributed myself;
7. Either none of this work has been published before submission, or parts of this work have been published as indicated on [PUBLISHED WORK AS PARTS OF THIS THESIS (See pages III)].

Name of Candidate: Wenjun Li Signature: Wenjun Li

Date: 1 October 2018

LASER INTERFERENCE LITHOGRAPHY FOR APPLICATIONS IN BIOMEDICINE

Wenjun Li

ABSTRACT

Surface modification of implant biomaterials has become the commonly used methods for the long life artificial implants and successful orthopaedic implantation. Numbers of technologies have been developed to improve the performances of artificial implants in biological systems. However, most of the technologies are associated with complex, time-consuming and not fully controllable processes, resulting in undesirable micro and nano structures. DLIL provides an effective method for nanomanufacturing of well-designed structures with controllability. The research reported in this thesis tackles the issues with particular focus on DLIL for the fabrication of well-designed micro and nano structures with functionalities including superhydrophobic, wear resistant property and biocompatibility on various biomaterials.

Four-beam DLIL was developed to design and fabricate the micro and nano convex structures on silicon surfaces. Parameters such as incident angle, azimuthal angle and polarisation direction were adjusted to simulate micro patterns in period of 5.5 μm for structure design, and laser fluence and exposure duration were set to fabricate micro

and nano hierarchical structures with the aspect ratio of 2-3. The CA value of 153.2° was obtained with excellent superhydrophobic property.

Three-beam DLIL was used to design and fabricate micro circular dimpled structures on Co-Cr-Mo alloy. The optimal setting of incident angle, azimuthal angle and polarisation direction for three interference beams was developed to form the circular dimpled patterns in period of 8 μm. Laser fluence and exposure duration were properly adjusted to fabricate circular dimpled structures with the optimal area density of 14.8%. The modified surfaces performed the improved wear resistant property with a 64% reduction of friction coefficient and 42% enhancement of hardness.

Two-beam DLIL was employed to fabricate micro grooved structures and three-beam DLIL was used to form micro dotted and dimpled structures on Ti6-Al-4V alloy by adjusting incident angle, azimuthal angle and polarisation direction. Microstructures in grooves, dots and dimples with roughness value ranged from 0.6 μm to 1.7 μm were achieved by the proper setting of laser fluence and exposure duration. MG-63 osteoblast cells were used to culture on modified Ti6-Al-4V alloy surfaces and the biocompatibility was improved by promoting cell proliferation, spreading and adhesion.

In this work, DLIL were developed to modify the biomaterials including silicon, Co-Cr-Mo alloy and Ti6-Al-4V alloy for their specific functions in artificial joint. The wear resistant property has been studied on modified Co-Cr-Mo alloy for the bearing surface of artificial femoral head and the biocompatibility of modified Ti6-Al-4V alloy has been investigated for the interfaces of artificial joint stem and bone tissue. The silicon has been also used to achieve the superhydrophobic performance for the foundation preliminary study of anti-bacteria property and bacteria infection.

PUBLISHED WORK AS PARTS OF THIS THESIS

- ✧ Research described in **Section 4.2** (Simulations and experiments of fabrication of superhydrophobic surfaces on silicon) and **Section 4.3** (Results and discussions) have been published in the paper: **Wenjun Li**, Zuobin Wang*, Dapeng Wang, Ziang Zhang, Le Zhao, Dayou Li, Renxi Qiu, and Carsten Maple. (2014) Superhydrophobic dual micro- and nano- structures fabricated by direct laser interference lithography, Optical Engineering, 53: 0341091-0341096.
- ✧ Research described in **Sections 5.2** (Circular dimpled structures fabrication) and **Section 5.3** (Tribological tests) have been published in the paper: Xiaofeng Wei*, **Wenjun Li**, Bojian Liang, Binglin Li, Jinjin Zhang, and Zuobin Wang*. (2016) Surface modification of Co-Cr-Mo implant alloy by laser interference lithography, Tribology International, 97: 212-217. And paper: Binglin Li, Xiaofeng Wei, Xu Di, Linshuai Zhang, Zuobin Wang and **Wenjun Li**. (2015) Effects of laser interference parameters on surface modification of Co-Cr-Mo implant alloy,Proc. 3M-NANO 2015, 325-328.
- ✧ Research described in **Section 6.2** (Fabrication of microstructures in grooves, dimples and dots on Ti-6Al-4V implant alloy), **Section 6.3** (Roughness and wettability) and **Section 6.4** (Biological experiments) have been published in the paper: Qi Liu, **Wenjun Li**, Liang Cao, Jiajia Wang, Yingmin Qu, Xinyue Wang, Rongxian Qiu, Xu Di, Zuobin Wang and Bojian Liang. (2017) Response of MG63 osteoblast cells to surface modification of Ti-6Al-4V implant alloy by laser interference lithography, Journal of Bionic Engineering, 14: 448-458.

ACKNOWLEDGEMENTS

I would like to express the deepest grateful to my families and my colleagues, for their support, encouragement and selfless love throughout my PhD.

I would like to extend sincere thanks to my supervisors Professor Zuobin Wang and Professor Dayou Li for providing a large amount of guidelines and useful information. They are both outstanding advisors. I have learned a tremendous amount from them, not only in science, but also about ideas and skills that will be invaluable in my professional life. Without his help, I would not have achieved my study goals. I would like to express extreme gratitude to Doctor Renxi Qiu, for his help and support throughout my PhD study.

True appreciation is given to the International Research Centre for Nano Handling and Manufacturing of China (CNM) for providing me an opportunity to carry out the experiments. Many thanks for the members of CNM, including Professor Zhengxun Song, Doctor Dapeng Wang, Doctor Ziang Zhang, Miss Xiaofeng Wei, Miss Qi Liu, Mr Liang Cao, Miss Miao Yu, Mr Li Li and all the members for helping me during my studies.

LIST OF CONTENTS

LIST OF PUBLICATIONS

Journal Papers

1. **Wenjun Li**, Zuobin Wang*, Dapeng Wang, Ziang Zhang, Le Zhao, Dayou Li, Renxi Qiu, and Carsten Maple. (2014) Superhydrophobic dual micro- and nanostructures fabricated by direct laser interference lithography, Optical Engineering, 53: 0341091-0341096.
2. Xiaofeng Wei*，**Wenjun Li**, Bojian Liang, Binglin Li, Jinjin Zhang, and Zuobin Wang*. (2016) Surface modification of Co-Cr-Mo implant alloy by laser interference lithography, Tribology International, 97: 212-217.
3. Qi Liu, **Wenjun Li**, Liang Cao, Jiajia Wang, Yingmin Qu, Xinyue Wang, Rongxian Qiu, Xu Di, Zuobin Wang and Bojian Liang. (2017) Response of MG63 osteoblast cells to surface modification of Ti-6Al-4V implant alloy by laser interference lithography, Journal of Bionic Engineering, 14: 448-458.

International Conference Papers

1. **Wenjun Li**, Liang Cao, Qi Liu, Miao Yu, Zuobin Wang, Dong Li, Jiao Meng and Dayou Li. (2017) Surface texturing on stainless steel by direct laser interference lithography, Proc. IEEE 3M-NANO 2017, 119-123.
2. Xiaofeng Wei, Binglin Li, Zuobin Wang and **Wenjun Li**. (2015) Reducing friction of an artificial hip joint by laser surface texturing, Proc. 3M-NANO 2015, 282-285.
3. Binglin Li, Xiaofeng Wei, Xu Di, Linshuai Zhang, Zuobin Wang and **Wenjun Li**. (2015) Effects of laser interference parameters on surface modification of Co-Cr-Mo implant alloy, Proc. 3M-NANO 2015, 325-328.

LIST OF TABLES

LIST OF FIGURES

LIST OF ABBREVIATIONS

B	beam splitter
CA	contact angle
CBD	chemical bath deposition
CNC	computer numerical control
Co-Cr	cobalt-chromium
Co-Cr-Mo	cobalt-chromium-molybdenum
CVD	chemical vapour deposition
DLIL	direct laser interference lithography
EE	electrolytic etching
gf	kilograms-force
HAZ	heat-affected zone
HAZ	heat-affected zone
HF	hydrofluoric acid
HV	Vickers hardness
LIL	laser interference lithography
M	high-reflective mirror
MEMS	micro-electromechanical system
MG63	Humanosteoblast-like osteosarcoma cell
MOP	metal-on-polyethylene
MTT	3- (4, 5-dimethyl-2-thiazolyl) -2, 5-diphenyl-2-H-tetrazolium bromide
OD	optical density
PBS	phosphate buffer saline

PDM	polydimethylsiloxane
PSM	plasma-surface modification
PVD	physical vapour deposition
RIE	reactive ion etching
RUM	rotary ultrasonic machining
SiO_2	silicon dioxide
TE	transverse electric wave polarisation mode
THR	total hip replacement
Ti6-Al-4V	titanium-6 aluminium-4 vanadium
TM	transverse magnetic wave mode
W	wave plate
XRD	X-ray diffraction

LIST OF NOMENCLATURE

$\vec{E}_n$	electric field vector
A_n	amplitude
$\vec{p}_n$	polarisation vector
$\vec{k}_n$	wave vector
$\vec{r}_n$	position vector
$\vec{n}_n$	unit vector in the wave propagating direction
ω	angular frequency
$\phi_{m,n}$	initial phase
k	wave number
θ_n	incident angle
φ_n	azimuthal angle
ψ_n	polarisation angle
p	period
λ	wavelength
r_i	distance from irradiation area to high-reflective mirror
I	intensity
A	contact area
A_{sl}	solid-liquid contact area
A_{lv}	liquid-vapour contact area

A_c	area of unit cell
A_0	apparent contact area
A_d	top area of single micro dot
A_f	flat projection
f_{sl}	factional solid-liquid area
f_{lv}	fractional liquid-vapour area
$R_{f,}$	surface roughness factor
$\alpha_{0,1,2}$	contact angle
γ_{sv}	solid/vapour interfacial free energy
γ_{sl}	solid/liquid interfacial free energy
γ_{lv}	liquid/vapour interfacial free energy
$P(X, Y)$	non-dimensional local bearing pressure
$H(X, Y)$	non-dimensional local bearing spacing
p_0	air pressure
p_d	average bearing pressure
c	minimum bearing spacing
U	relative sliding velocity
μ	dynamic viscosity
r_p	radius of dimple
τ	average shear stress
V_d	volume of a dimple
f	friction coefficient
W	cumulative volume of material worn

K	wear coefficient
L	sliding distance
w	normal load
H	hardness
n	applied normal load
D_0	mean diameter of abrasive particles
d	Average grain size
H_0, K_H	materials constants
ρ_s	density of silicon
T_e	exposure duration
T	temperature
k	thermal conductivity
u_r	vaporisation velocity
η	absorption coefficient of silicon
x, y, z, r	spatial coordinates
T_c	cleanout time
V	contrast of stripes
I_{max}	maximum intensity
I_{min}	minimum intensity
t	a given point in time
R_a	arithmetic mean surface roughness
h	height of droplet contour
D	diameter of the cross-section area of the microstructure and the droplet

δ	rotation angle of protractor
R	proliferation rate
OD_1	optical density at the beginning of culture time
OD_2	optical density at the end of culture time

CHAPTER 1

INTRODUCTION

1.1 Motivation

The increased average human age accompanied by reduced organ functions and regenerative potential of tissues has attracted global attention in the development of implant materials with good biocompatibility, suitable for artificial organs components, for example, heart valves, vessels, bones, teeth, cartilages, and ligaments. Numbers of various impressive materials have been used for such applications, including metals, ceramics and polymers [1]. Joint damage has become one of the most common diseases in the modern society. Prosthetic replacement is the best method to treat the damaged joints for the unremitting pain induced by function loss. At present, total hip replacement (THR) is recognized as a relative safe and effective approach for the treatment of end-stage arthritis, and improves the functional capability and quality of life of patients who suffer from arthritic disease by releasing the pain. In United States, over 285 thousands total hip replacement arthroplasties are conducted and more than 1 million prosthetic replacements are conducted in one year all over the world. European database shows that the mean revision rates of post primary THR for using 5, 10 and 20 years are increased as 6.45%, 12.9% and 16.7%. A joint prosthesis with high life quality is greatly restricted to around 15years [2–5]. Bearing wear of artificial joint induced the implant loosening, and caused osteolysis and bacterial infection by local host biological responses, which were the commonly

occurred inducements of revision [6, 7]. Wear and friction occurred during the relative motion of contacted surfaces and the deformation and energy losses usually caused by increased friction coefficients in the biomedical system [8]. A successful implantation depends on two main critical issues. The first is the loosening related to the interaction of insert implant material with bone which is dependent on the surface functionality of biocompatibility and the other is the deformation and corrosion caused by wear of the articulating surfaces (femoral head/cup surfaces) and the debris generated during wear process which are related to the functional surfaces with superhydrophobic performance and wear resistant property [9]. Surface engineering provides effective methods to produce surfaces of the artificial components with functional properties such as superhydrophobic performance, wear resistance and biocompatibility between the materials with their physiological surroundings. Surface modification is the key in surface engineering. It implements the surface functional properties of the components to allow the components to be better adapted to physiological surroundings, leading to the improved performances in biological systems [10]. Surface modification is attracting the global attentions.

Research suggests the impact of the functional properties on the interaction and the strong influence of surface characteristics, including topography, geometrical characteristics, roughness, hardness, and surface energy, on the surface functions [11-13]. The research also suggests that the surface characteristics can be controlled by surface modification [14]. The impacts of surface functions have been well studied in the interactions between implants and the surrounding physiological environment [12]. However, the role of surface modification in realising specific surface functions via implementing certain surface characteristics requires a better understanding.

A variety of surface modification techniques have been developed in different applications of the materials in biomedicine [15-22]. Among them, nanomanufacturing is recognised powerful for the surface modification of implant biomaterials. Its capabilities of fabricating micro and nano structured surfaces with specific functional properties have greatly pushed forward the developments in biomaterials for implantation.

Numbers of research efforts has been attributed to the surface modification techniques, focusing on the functional properties such as superhydrophobicity, wear resistance and biocompatibility of implant biomaterials. Plasma-surface modification (PSM), laser processing, laser interference lithography (LIL), heat treatment and photolithography have been developed in recent years. The preparatory step is required before actual treatment for PSM method and for LIL and photolithography technologies the optical mask is used to transfer the pattern to the surface. For the , heat treatment is usually used for metal and alloy materials to alter the mechanical properties which required a long processing time. So, most of the techniques are associated with complex, time-consuming and not fully controllable processes, resulting in undesirable micro and nano structures.

The research reported in this thesis tackles the problems with the particular focus on controllability in nanomanufacturing using direct laser interference lithography (DLIL). DLIL has two phases, namely, simulation and fabrication. The first phase aims at DLIL systems configuration setup to achieve the desired interference patterns. A DLIL system consists of optical components such as high-reflective mirrors (M), beam splitters (B), wave plates (W) and polarisers (P). The system configuration in the sense of optical setup geometry (relative positions of optical components) is

depended on the incident angle of each coherent beam which is determined in the simulation phase. Therefore, simulations are undertaken at this phase in the manner of manipulating the wavelength of laser source, incident angle of each coherent beam and polarisation direction and observing the effects on the interference patterns with different feature sizes. The fabrication process parameters such as laser fluence and exposure duration are also determined via simulations. In the second phase, the multi-beam DLIL system configuration obtained in the first phase is set up to fabricate the structures.

DLIL provides a highly controllable way to fabricate well-designed structures with different feature sizes on various materials. The interference laser beams irradiate on the surface and the melt and vaporisation are occurred with removing the materials away to form the structures directly on the surface by one step. The processing area can achieve over 0.5 cm^2 in a few seconds [23]. It is a maskless, noncontact technology without pre-treatment processes and, hence, is easy to implement. It also has relative short process time. These advantages make DLIL particularly suitable for effectively fabrication of controllable patterns with two-dimension or three-dimension structures from the micro to nano scale.

1.2 Aim and Objectives

The aim of this research is to develop DLIL-based techniques for realising functional properties such as superhydrophobicity, wear resistance and biocompatibility in implant biomaterials surface modification. These functional properties are essential to

long-life artificial components in orthopaedic. The wear resistant property has been studied on modified Co-Cr-Mo alloy for the bearing surface of artificial femoral head and the biocompatibility of modified Ti6-Al-4V alloy has been investigated for the interfaces of artificial joint stem and bone tissue. The silicon has been also used to achieve the superhydrophobic performance for the foundation preliminary study of anti-bacteria property and bacteria infection. A successfully implantation depends on two main critical issues. One is the loosening related to the interaction of inserted implant material and bone and the other is the deformation and corrosion caused by wear of the articulating surfaces (femoral head/cup surfaces) and the debris generated during wear process.

To realise the potential of DLIL in surface modification, the following objectives must be achieved:

- To discover the optimal micro and nano structures for superhydrophobicity, wear resistance and biocompatibility, respectively.

- To fabricate optimal micro and nano structures with proper asperities density, aspect ratio and geometrical structure on silicon by four-beam DLIL to achieve the superhydrophobic surface with increasing contact angle (CA) value.

- To fabricate optimal micro circular dimpled structures with proper dimple shape, size and density on cobalt-chromium-molybdenum (Co-Cr-Mo) alloy by three-beam DLIL to improve wear resistant property with the decreased friction coefficient and enhanced hardness.

- To fabricate optimal micro grooved, dotted and dimpled structures with roughness around 1 μm ontitanium-6 aluminium-4 vanadium (Ti6-Al-4V) alloy

by two- and three- beam DLIL to improve the biocompatibility by promoting cell proliferation, spreading and adhesion to Humanosteoblast-like osteosarcoma cells (MG63).

1.3 Methodology of the Research Work

The methodology applied to this research can be described as theoretical investigation informed experiments and qualitative analysis guided system design, which is summarised in Fig. 1.1.

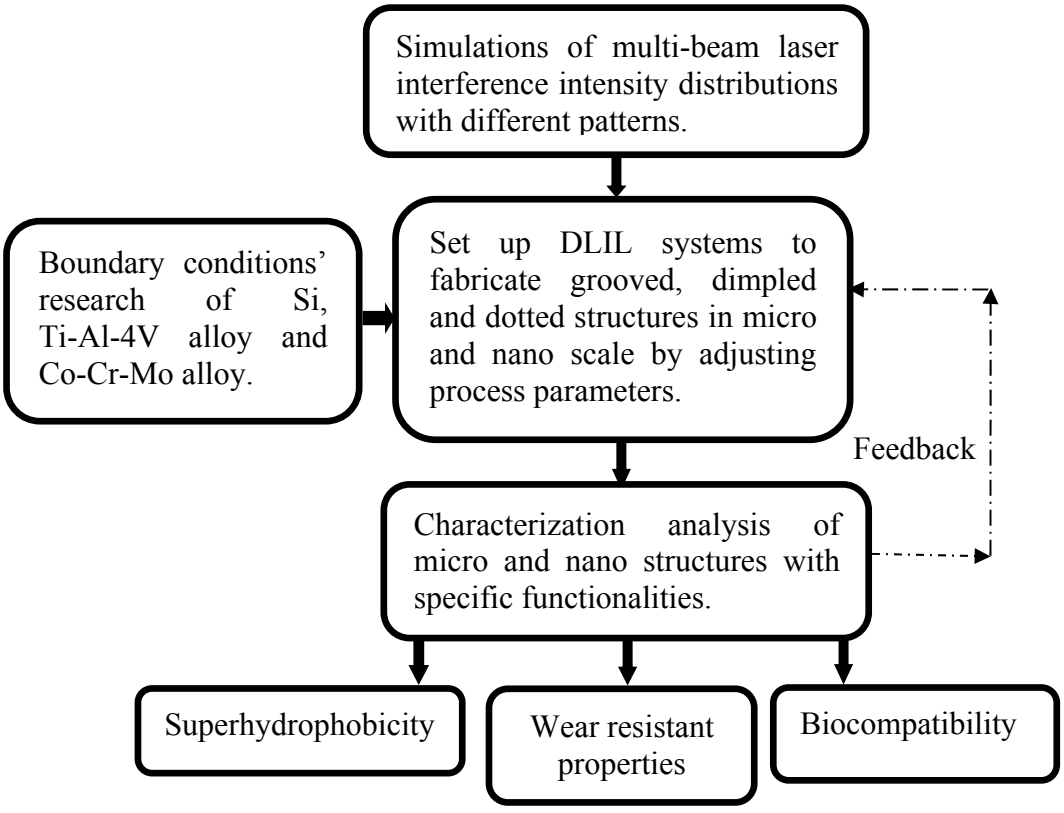

Fig. 1.1 Framework for research methodology.

The theoretical investigation into the relation between surface functional characteristics such as superhydrophobicity, wear resistant property and

biocompatibility, and the formation of multi-beam direct laser interference patterns were undertaken firstly. Based on the theory, simulations were carried out. In the simulations, the specific number of beams, incident angles and wavelength were selected to create the patterned structures for the design of micro and nano structures with the different characteristics. The aim of the simulations is to achieve micro grooved, convex and dimpled structures with different geometric shapes using the multi-beam interference. Based on the theoretical investigation and the simulation, qualitative analysis was performed to identify the boundary conditions of different materials and optimise the parameters of cross-scale multi-beam interference patterns, including incident angles, azimuthal angles, polarisation directions, laser fluences and exposure durations for the fabrication of simulated patterns with specific functionalities on different materials.

In this work, the use of multi-beam DLIL technology for the cross-scale structured surfaces with superhydrophobicity, wear resistant property and biocompatibility of various materials were studied in detail. The simulation results were carried out for fundamental analysis of generation of interference intensity patterns. Experimental research of interaction with different biomaterials and boundary conditions was carried out to fabricate the micro and nano structures according with the simulated patterns. DLIL is developed for the surface modification of various materials with superhydrophobicity, wear resistant property and biocompatibility. High absorbance of different materials at a specific wavelength of laser source allows the reduction of the laser intensity required to obtain a determined structure depth. The high power nanosecond laser with the wavelength of 1064 nm was used to setup the direct laser interference systems, aiming to directly fabricate cross-scale and large-area micro and

nano structures on silicon, Co-Cr-Mo alloy and Ti-6Al-4V alloy. The laser intensity redistributed by interference beams is transferred to the irradiated area on the material surface and the specific periodic structures can be formed directly through the high-power laser. The structures can be fabricated by controlling DLIL process parameters including laser wavelength, incident angle, azimuthal angle, polarisation direction, laser fluence and exposure time. The feature sizes such as height, depth, period and roughness of structured surfaces were studied with respect to the superhydrophobicity, wear resistant property and biocompatibility. The boundary conditions for the cross-scale structuring or modification of biomaterials under the action of two, three and four coherent beams of radiation of a laser were investigated. The modification thresholds of Co-Cr-Mo, Ti-6Al-4V alloys and silicon were determined. The laser fluence and exposure duration have a significant effect on the roughness and structured feature size such as diameter, height and depth of dimples and dots. When the laser fluence exceeds a certain level, the structures are molten and destroyed. Since the threshold of different materials ablation determines the energy of single pulses to be used, the impacts of different laser fluences and exposure durations were investigated on silicon, Co-Cr-Mo alloys and Ti-6Al-4V alloys, respectively. The optimal values of laser fluence and exposure duration of different materials were experimentally studied. With the investigation of the two-beam, three-beam and four-beam laser interference, the structured surfaces with specific feature sizes and geometrical characteristics such as shape (circular and elliptical), diameter, period, height and depth were well-designed and controlled through the DLIL technology which was both analytically and experimentally to modify the biomaterials. In the experimental research, DLIL as a maskless technique without pre-treatment processes and pattern transfer procedures is employed to fabricate the micro and nano structures

with specific functionalities via controlling the process parameters due to that the intensity redistributed by the superposition of interference beams is transferred to the substrate surfaces as a result of formatting periodic structures directly. The superhydrophobic surfaces with hierarchical micro and nano structures were fabricated on silicon using four-beam DLIL. The micro and nano dimpled structured surfaces with different geometrical shapes were obtained by three-beam laser interference lithography on Co-Cr-Mo alloy to improve the wear resistant property. The two- and three- beam laser interference systems were setup to fabricate micro structures in grooves, dimples and dots on Ti-6Al-4V alloy surfaces to investigate the cell behaviours.

The methodology is effective in this research. The theoretical research is corresponded with the experiment results with the help of the methodology which indicates that the DLIL has the advantages for the fabrication of highly controlled structures with the well-designed functional surfaces and specific feature sizes.

1.4 Achievements

This research focuses on the development of one-step DLIL for new applications in biomedicine on micro and nano scales. DLIL was used for the design and fabrication of micro and nano surface patterns with different well-defined functionalities to modify silicon and artificial joint including Co-Mo-Cr alloy (femoral head) and Ti-Al-4V alloy (joint stem).

Four-beam direct laser interference simulation was carried out to design micro and nano dotted patterns and the convex structures were formed on silicon surface by setting up the laser interference systems to achieve the superhydrophobic property.

Three-beam DLIL was developed to design and fabricate dimpled structures on Co-Cr-Mo alloy to improve the wear resistant properties by reducting the friction coefficient and increasing the hardness.

Two- and three-beam DLIL were developed to fabricate grooved, dimpled and dotted structures on Ti-Al-4V alloy to improve the proliferation, spreading and adhesion of osteoblast cells for the good biocompatibility.

As for the experiments, the high power nanosecond laser with the wavelength of 1064 nm was used to setup the laser interference systems, aiming to directly fabricate cross-scale and large-area micro and nano structures on alloys and silicon. The control of the substrate topographical structures in fabrication were also carried out for the investigation of the surface modification of biomaterials. These investigations pave an avenue for further development of one-step DLIL for the applications in biomedicine.

The achievements of my PhD research work have been published in 3 journal papers and 3 conference papers. A number of experiment results demonstrated in Chapters 4, 5 and 6 are related to the previously published work. Chapter 4 cites the study of "Superhydrophobic dual micro- and nanostructures fabricated by direct laser interference lithography" which was published in the journal of Optical Engineering. Chapter 5 cites the study of "Surface modification of Co-Cr-Mo implant alloy by laser interference lithography" was published in the journal of Tribology International. Chapter 6 cites the study of "Response of MG63 osteoblast cells to surface

modification of Ti-6Al-4V implant alloy by laser interference lithography" which was published in Journal of Bionic Engineering.

1.5 Organisation of Thesis

According to the methodology, the structure of the thesis is well established. Seven chapters described the motivation, theoretical analyses, experimental research for process parameters and fabrication of functional surfaces respectively. So this thesis is divided in two sections: theories and experiments & applications. The introductory Chapter 1 revealed the motivation of my PhD research work and the aim and objectives were extracted. In Chapter 2, the theoretical analysis of DLIL and a literature review of surface modification technology for the applications in biomaterials were shown to emphasize the importance of development of DLIL. Methodology of this research was also demonstrated in this chapter. In Chapter 3, the functional surfaces including superhydrophobicity, wear resistant property and biocompatibility were described related to the background and literature review. Multi-beam interference systems were developed to study the process parameters of different materials. Various novel simulation results such as dual micro and nano patterns and periodic dimple patterns were found. The research efforts of this work were the development of one-step surface modification technology, which focused on the functionalities such as superhydrophobicity, wear resistant property and biocompatibility. The simulated and experimental researches were carried out in Chapters 4, 5 and 6. Four-beam interference system was set up to fabricate

hierarchical micro and nano structures and obtain the superhydrophobic surfaces. Different laser fluences and exposure durations were studied to investigate the wettability of dual structures. As for the high-resolution and high controllable characteristics, the most usually used hard implant materials were selected as the experiment objects in Chapter 5 to improve the wear resistant property for the long life implant materials. It is worth to mention that DLIL offers a highly controllable way to do the experimental research for biomedical applications. Chapter 6 deals with the cell behaviour of modified implant materials fabricated by two- and three- beam DLIL with different structure feature sizes in micro and nano scale. Therefore, the methodology plays an important role in the integrity throughout the whole thesis.

CHAPTER 2

FUNDAMENTAL THEORIES AND METHODOLOGY

2.1 Direct Laser Interference Lithography

DLIL uses the interference intensity pattern generated from two or more interference laser beams for the modification of materials. The interference pattern is the superposition of electric field vectors of interfering beams and can be transferred to the substrate surfaces as a result of formation of periodic structures directly [23]. Arrays of laser beam lines, dimples or various distributions can be formed on the surfaces. Different complex patterns with various geometrical shapes can be produced on target materials using different intensity distributions and the optimal intensity distributions can be adjusted by controlling the exposure beam intensity over the material modification threshold [24, 25]. DLIL technology can increase the peak light intensity over the ablation threshold of materials by adjusting the laser distribution instead of the focusing system. It is a parallel fabrication method and a primary processing area can achieve over 0.5 cm^2 and even more so that the periodic patterns in micro and nano scales with a well defined cross-scaled fabrication can be implemented in a few seconds [26, 27].

In the irradiation area, the intensity distribution of a general form of N-beam laser interference can be expressed as [28]

$$\vec{E}_n = A_n \vec{p}_n \exp[i(\vec{k}_n \cdot \vec{r} - \omega \cdot t + \phi_n)] \text{ n=1, 2……, N} \qquad (2.1)$$

In Eq. (2.1), $\vec{E}_n$ is the electric field vector. A_n is the amplitude. $\vec{p}_n$ is the polarisation vector. $\vec{k}_n$ is the wave vector. $\vec{r}_n$ is the position vector. ω is the angular frequency. ϕ_n is the initial phase. The polarisation vector and the wave vector can be written as [28]

$$\begin{aligned}\vec{p}_n = &-(\cos\theta_n \cos\varphi_n \cos\psi_n - \sin\varphi_n \sin\psi_n)\cdot\vec{x} \\ &-(\cos\theta_n \sin\varphi_n \cos\psi_n + \cos\varphi_n \sin\psi_n)\cdot\vec{y} \\ &-(\sin\theta_n \cos\psi_n)\cdot\vec{z}\end{aligned} \tag{2.2}$$

$$\vec{k}_n = k(\sin\theta_n \cos\varphi_n \cdot\vec{x} + \sin\theta_n \sin\varphi_n \cdot\vec{y} - \cos\psi_n - \cos\theta_n \cdot\vec{z}) \tag{2.3}$$

where $\vec{x}$, $\vec{y}$ and $\vec{z}$ are the unit vectors in the three coordinate directions. k is the wave number ($k = 2\pi/\lambda$). θ_n is the incident angle. φ_n is the azimuthal angle. ψ_n is the polarisation angle.

The interference intensity distribution for N-beams can be computed by [28]

$$\begin{aligned}I(r) &= \sum_{n=1}^{N}\left|\vec{E}_n\right|^2 = \sum_{n=1}^{N}\sum_{m=1}^{N}\left|\vec{E}_n\right|\left|\vec{E}_m\right|\cos(\vec{E}_n\cdot\vec{E}_m) \\ &= \sum_{n=1}^{N}\sum_{m=1}^{N} A_n\vec{p}_n\cdot A_m\vec{p}_m\cdot e^{[i(\vec{k}_n-\vec{k}_m)\vec{r}+\varphi_n-\varphi_m]}\end{aligned} \tag{2.4}$$

The difference between the pair of wave vectors ($\vec{k}_n - \vec{k}_m$), where n, m=1,2,3... and n<m, determines the spatial periodicity of interference pattern. According to Eqs. (2.2) and (2.4), various interference patterns with different shapes, sizes, periods, contrasts and intensity peaks can be achieved by setting up multi-beam laser interference

systems which depend on optical setup geometry and used laser wavelength. The period of interference pattern decreases with the decrease in the wavelength of laser source, and distance between the mirror planes to substrate plane.

A DLIL system consists of a high power laser source, several optical mirrors and beam splitters. Beam splitters (B) and high-reflective mirrors (M) are used to divide the laser source into two, three, or more beams. Additionally, wave plates (W) and polarisers (P) are used to control the phase and polarisation of each coherent beam. The high power nanosecond pulsed laser allows a direct, periodically local heating of substrate surfaces through the local-thermal interaction between laser and material in the irradiation area which is always used to fabricate structures directly on metals alloys, and various polymers. The physical reactions take place in the following three phases:

(1) Surface melting caused by laser energy absorption;

(2) Surface vaporisation leads to material removal;

(3) Plasma plume evolution and phase explosion.

The process of DLIL technology can be seen in Fig. 2.1.

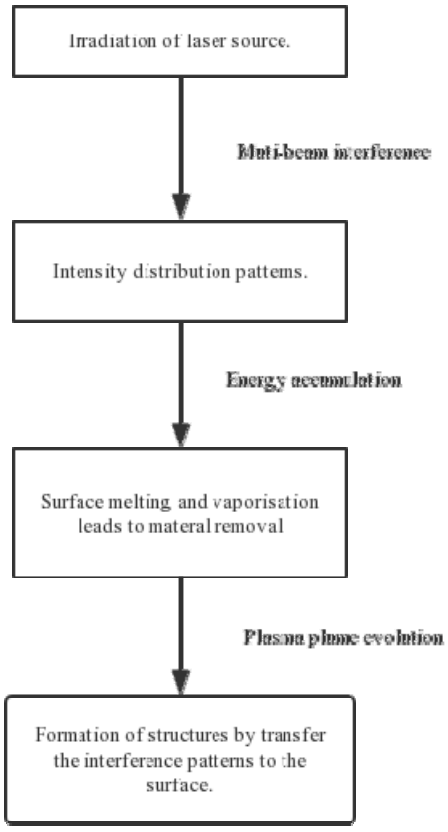

Fig. 2.1. Diagram of DLIL process.

Materials absorb laser energy when being heated and becomes melting, and then vaporisation occurs because the materials accumulate more and more energy. The process parameters including the laser fluence and exposure duration have influence on the formation of microstructures.

Laser fluences and exposure durations are crucial to the physical reactions. Increasing the laser fluence will cause part of the laser energy to be absorbed by the vapour for the vaporisation breakdown and cause complicated gas dynamic evolution to occur in silicon vapour and the ambient air above the substrate. When vaporisation occurs, the process of thermal transportation in materials can be described by [29-31]

$$\rho_s \frac{\partial h}{\partial t} + \rho_s u_r \frac{\partial h}{\partial z} = \frac{1}{r}\frac{\partial}{\partial r}(rk\frac{\partial T}{\partial r}) + \frac{\partial}{\partial z}(k\frac{\partial T}{\partial z}) + \alpha_s I \tag{2.5}$$

In Eq. (2.5), z and r are the perpendicular spatial coordinates, h is the enthalpy, which depends on temperature, ρ_s is the density of silicon, T_e is the exposure duration, T is the temperature at time t, k is the thermal conductivity, u_r is the vaporisation velocity (velocity of surface recession), I is the intensity of laser beam approaching to the silicon surface, which has a Gaussian spatial profile in the r direction, and α_s is absorption coefficient of silicon, which is a function of temperature.

The exposure duration and laser fluence determine the vaporisation velocity u_r [32, 33]. Given the exposure duration, an increase in the laser fluence can reduce the relaxation time of vaporisation, leading to increases in the velocity of surface recession (vaporisation) and temperature evolvement. It has been found that the vaporisation velocity is not a linear function of laser fluence and exposure duration due to the effect of Gaussian distribution of laser beam [34].

When the laser fluence approaches to the energy threshold (the energy for phase explosion) of silicon, the vapour breaks down and plasma plump forms. The part of laser energy is absorbed by plasma plump resulting in the reduction of vaporisation velocity along with the increase of laser fluence. Vaporisation and plasma plump are the critical factors in the ablation process [34]. The increased velocity of surface recession with the proper exposure duration can produce high aspect ratio. However, with the increase of exposure duration, the silicon absorbs the exceed energy to melt and destroy the ablated structures [35]. High absorbance of different materials at a specific wavelength of laser source allows the reduction of the laser intensity required to obtain a determined structure depth.

2.1.1 Two-Beam Laser Interference Lithography

The typical configuration of two-beam interference lithography is splitting a laser beam into two coherent beams then overlapping the beams to make interference pattern. The grooved structures are obtained by irradiating the substrates using a two-beam laser interference setup. Two-beam interference forms an intensity modulation in sryiped pattern. It is demonstrated that two coherent plane waves are propagating in air with vectors in the x-z plane incident onto the x-y plane at symmetric angles with respect to the z axis. According to Eqs. (2.1) to (2.4), the electric field vectors are expressed below [29]:

$$\vec{E}_1 = A \cdot e^{[ik(\sin\theta_1 \cdot x - \cos\theta_2 \cdot z) - \omega t]} \tag{2.6 a}$$

$$\vec{E}_2 = A \cdot e^{[ik(-\sin\theta_2 \cdot x - \cos\theta_2 \cdot z) - \omega t]} \tag{2.6 b}$$

where $\vec{E}_n$ (n=1, 2) is electric field vector corresponding to each beam, A is the amplitude of the electric field vectors, i is the unit vector in x directions, θ_n (n=1, 2) are incident angles of each beam, ω is the angular frequency. $k = 2\pi\lambda^{-1}$ is the wave number. t is a given point in time. The intensity distribution is given by [28]

$$I = A^2\{2 - 2\cos\varphi \cdot \cos[k \sin\theta \cdot (x\cos\varphi + y\sin\varphi) + x]\} \tag{2.7}$$

where θ is the incident angle and φ is the azimuthal angle. x and y are the positions. The resulted micro grooved pattern with best contrast can be achieved by symmetrical two-beam incident. The intensity distribution of two-beam interference

with $\theta_1 = \theta_2 = \theta$, $\varphi_1 = 0^0$, $\varphi_2 = 180^\circ$,and $\psi_1 = \psi_2 = 90^\circ$ is written as [29]

$$I = A^2[2 - 2\cos(2k\sin\theta \cdot x)] = A^2[2 - 2\cos(2\pi\frac{2\sin\theta}{\lambda}x)] \tag{2.8}$$

It can be seen from Eq. (2.8) that the period of two-beam interference grooved pattern is determined by

$$p = \frac{2\pi}{2\pi \cdot \frac{2\sin\theta}{\lambda}} = \frac{\lambda}{2\sin\theta} \tag{2.9}$$

in the case of symmetrical two-beam incident. The resulting spatial period or fringe-to-fringe spacing (p) depends on the laser wavelength (λ) and half of the beam intersection or named as incident angle (θ). It is indicated that the period of the patterns is a function of the laser wavelength and incident angle of coherent beams and the incident angle depends on the distance between the mirror plane and substrate plane.

For a two-beam interference pattern, the intensity distribution ratio of total intensity of coherent beams I and individual intensity of each interference beam I_0 is given by [28]

$$\frac{I}{I_0} = 4\cos^2(\frac{\pi(r_1 - r_2)}{\lambda}) \tag{2.10}$$

where r_1 and r_2 are the distances from the irradiation area to M1 and M2, respectively. The maximum intensity ratio is $I / I_0 = 4$ when r_1=r_2.

A beam splitter (B) and two high-reflective mirrors (M) are sufficient for dividing the laser source into two interference beams. The polarisers (P) and wave plates (W) can

be placed before the substrate. The simple paths of the two coherent lights can be described as follows:

(1) Laser-B1-M1- Irradiation area.

(2) Laser-B1-M2- Irradiation area.

2.1.2 Three-Beam Laser Interference Lithography

For the fabrication of three-dimension structures, three-beam laser interference is much more flexible than two-beam laser interference, which can form the dotted and dimpled patterns with different geometrical shapes in one step and suitable for large-area fabrication. The dimple/dot density of the interference pattern depends on the incident angle and the wavelength of the laser source. The polarisation angle also has an influence on the formation of the interference patterns, pattern contrasts and periods in three-beam interference lithography. According to Eq. (2.1), the intensity distribution of three interfering field can be described by [30]

$$I = \sum_{n=1}^{3} \left| \vec{E}_n \right|^2 + \sum_{n \neq m}^{3} \vec{E}_n^{\,*} \cdot \vec{E}_m \exp\{n[(\vec{k}_m - \vec{k}_n) \cdot \vec{r}_n + (\phi_m - \phi_n)]\} \tag{2.11 a}$$

$$\vec{k}_n = k(\sin\theta_n \cos\varphi_n \cdot \vec{x} + \sin\theta_n \sin\varphi_n \cdot \vec{y} - \cos\theta_n \cdot \vec{z}) \tag{2.11 b}$$

$$\vec{r} = x \cdot \vec{i} + y\,\vec{j} + z \cdot \vec{k} \tag{2.11 c}$$

$$\vec{p}_n = -(\cos\theta_n \cos\varphi_n \cos\psi_n - \sin\varphi_n \sin\psi_n)\cdot\vec{i}$$
$$-(\cos\theta_n \sin\varphi_n \cos\psi_n + \cos\varphi_n \sin\psi_n)\cdot\vec{j}$$
$$-(\sin\theta_n \cos\psi_n)\cdot\vec{k} \qquad (2.11\ \text{d})$$

where $\vec{E}_n$ (n=1, 2, 3) is the electric field vector corresponding to each beam, A_n is the amplitude of electric field vectors, $\vec{p}_n$ is the vector of polarisation, $\vec{i}$, $\vec{j}$ and $\vec{k}$ are the unit vectors in the three coordinate directions, $\vec{k}_n$ is the wave vector, θ_n is incident angle, ϕ_n is the phase, ψ_n is the polarisation angle, $k = 2\pi\lambda^{-1}$ is the wave number, φ_n is the azimuth angle, $\vec{n}_n$ is the unit vector in the wave propagating direction, ω is the frequency, and $\vec{r}_n$ is the position vector. The first part of Eq. (2.11 a) is the background intensity and the second part contains the periodic variations. The difference between the pair of wave vectors ($\vec{k}_n - \vec{k}_m$), where *n*, *m*=1,2,3 and *n*<*m*, determines the spatial periodicity of interference pattern. According to Eq. (2.11 b), the incident angle and azimuth angle influence the uniformity and symmetry of periodic pattern. It is known that multi-beam laser interference patterns can be considered as superposition of multiple parallel stripes which are cosine distributed. The contrast of stripes *V* can be defined by [155]

$$V = \frac{I_{\max} - I_{\min}}{I_{\max} + I_{\min}} \qquad (2.12\ \text{a})$$

$$V_{nm} = \frac{2}{3}\cos(\varphi_n - \varphi_m)[\cos^2\theta \cos\psi_n \cos\psi_m + \sin\psi_n \sin\psi_m] -$$
$$\frac{2}{3}\cos\theta \sin(\varphi_n - \varphi_m)\sin(\psi_n - \psi_m) + \frac{2}{3}\sin^2\theta \cos\psi_n \cos\psi_m \qquad (2.12\ \text{b})$$

Where I_{max} and I_{min} are the maximum intensity and minimum intensity of superposed distribution, respectively. The equation clearly shows that the azimuthal angle, incident angle and polarisation angle have the effect on the intensity distribution of superposed field. The dimple/dot density is related with the size of dimple/dot and dimple/dot period (dimple-to-dimple spacing). The dimple/dot period p of three beams DLIL is calculated by

$$p = \frac{2\lambda}{3\sin\theta} \tag{2.13}$$

where λ is the wavelength and θ is the incident angle.

The more complicated formula is given to express the intensity distribution ratio of three coherent beams [28]

$$\frac{I}{I_0} = 4[\cos^2(\frac{\pi(r_1 - r_2)}{\lambda}) + \cos^2(\frac{\pi(r_1 - r_3)}{\lambda}) + \cos^2(\frac{\pi(r_2 - r_3)}{\lambda})] - 3 \tag{2.14}$$

where r_1, r_2 and r_3 are the distances from the irradiation area to M1, M2 and M3, respectively. The maximum intensity ratio is $I / I_0 = 9$ when r_1=r_2=r_3.

Two beam splitters (B) and three high-reflective mirrors (M) are sufficient for dividing the laser source into three interference beams. The simple paths of the three coherent lights can be described as follows:

(1) Laser-B1-M1-Irradiation area.

(2) Laser-B1-B2-M2-Irradiation area.

(3) Laser-B1-B2-M3-Irradiation area.

2.1.3 Four-Beam Laser Interference Lithography

More complex three dimensional structures can be patterned by four beams depending on the relative positions of coherent beams. The intensity distribution of three coherent beams is demonstrated by [28]

$$\frac{I}{I_0} = 4[\cos^2(\frac{\pi(r_1 - r_2)}{\lambda}) + \cos^2(\frac{\pi(r_1 - r_3)}{\lambda}) + \cos^2(\frac{\pi(r_1 - r_4)}{\lambda}) + \cos^2(\frac{\pi(r_2 - r_3)}{\lambda}) + \cos^2(\frac{\pi(r_2 - r_4)}{\lambda}) + \cos(\frac{\pi(r_3 - r_4)}{\lambda})] - 8 \quad (2.15)$$

where r_1, r_2, r_3 and r_4 are the distances from the irradiation area to M1, M2, M3 and M4, respectively. The maximum intensity ratio is $I / I_0 = 16$ when $r_1=r_2=r_3=r_4$.

Two beam splitters (B) and three high-reflective mirrors (M) are sufficient for dividing the laser source into three interference beams. The simple paths of the three coherent lights can be described as follows:

(1) Laser-B1-B2-M1-Irradiation area.

(2) Laser-B1-B2-M2-Irradiation area.

(3) Laser-B1-B3-M3-Irradiation area.

(4) Laser-B1-B3-M4-Irradiation area.

2.2 The Current Micro and Nano Fabrication Technologies for Biomaterial Surface Modification

Applications of biomaterials in the areas such as tissue engineering and implantation

suggest the surface topography and roughness to be optimised to achieve functional requirements of biomaterial surfaces [37-39]. Optimising surface topography and geometrical characteristics for the functionalities was investigated in physics and chemistry [40, 41]. The rapid developments in biomaterials for implantation have resulted in the fabrication of micro and nano structured surfaces achieving specific functionalities using a variety of methods. Particular emphasis has been placed on the role of DLIL in fabricating micro and nano cross-scale structured surfaces for the applications in biomedicine. Advances in biological implant modification and tissue engineering are motivating the development of three-dimensional structures in micro and nano scale. The design and fabrication process of structured surfaces are investigated to implement the specific functionality according to the requirements of practical applications in biomaterials. Nano patterns have impacts on cell behaviour, e.g. regularity and symmetry [42], geometric characteristic [43, 44] and surface energy [45]. There are different fabrication techniques that are capable of realizing the patterns. More precisely, there are different ways to control the colloidal deposition, resulting in the patterning of specific areas of a substrate. Therefore, it is necessary to select fabrication techniques that are appropriate to specific applications. In this chapter, modern surface modification techniques are described according to the three categories that are classified. Critical analysis regarding the key criteria is also presented.

2.2.1 Adding Material Techniques

The physically and chemically based technologies have been used to form thin films

with micro and nano structures on various materials. The chemical deposition methods such as chemical vapour deposition (CVD) and electro deposition technique are based on chemical conversion between the substrate material and the reactants. For any chemical reaction or deposition modified process, the preparatory step is required before the actual treatment that the target pattern of special ink is printed directly on the substrate materials [46].

The physical deposition methods are based on the processes including aggregation, evaporation, solidification and sputtering. Inkjet printing as the commonly used method was employed to fabricate wear resistant surfaces by depositing the structured polymers, metals and ceramics which were transferred to the substrate material in order to form microstructures with the solidification and evaporation of precursor [47-50]. Physical vapour deposition (PVD) methods were used to create the films with the improvement of tribological performances. [51-54]. The common methods of chemical surface modification are hydrogen peroxide treatment, acid treatment and thermal oxidation treatments. The hierarchical structures from micro to nano scale with large-area production can be obtained on biomaterials by chemical reactions [55]. TiO_2 nanostructures were formed on the metallic titanium by hydrothermal treatment with H_2O_2 solution at 80℃ [56]. The reaction time from 6 h to 72 h was performed to study the development of the top layer with nanostructures of the substrates. The TiO_2 nanostructure has the negative surface potential which is the critical reason for the good biocompatibility and anti-bacteria property. The key advantages consist in the variety of pattern geometry that can be obtained by CVD and PVD, even though provide qualitative coating films without substrate damage.

Plasma-deposited films can change the characteristics of material surfaces such as

mechanical properties and biocompatibility. In plasma-based methods, proper plasma sources are used for specific requirements on different materials. Rieu et al. modified the Ti alloy, stainless steel and polyethylene with a thin layer less than 1μm thickness by ion implantation in order to improve the mechanical properties and wettability [57]. Three-dimensional plasma titanium coatings with capillary-porous were fabricated on the implant by Kalita et al. They investigated the shear strength values of the interfaces between the coated implant surfaces and osseous block [58]. Plasma-grafting co-polymerization is considered to provide existing polymers with specific functionalities such as hydrophilicity, biocompatibility and lubrication [59]. Plasma-based technique is applicable to various materials such as alloys, metals, polymers and composites.

Pattern formation is required for both chemical, physical and plasma deposition methods which are based on the mask shield created by micro contact printing technique. Fig. 2.2 showed the plasma-based process. For instance, photolithography is an attractive method for low cost nanopatterning method. It is suitable for the large-area fabrication in a one-step high effective way with the advantages for the biological applications [60]. However, the mask is required for the primary pattern in contact lithography methods.

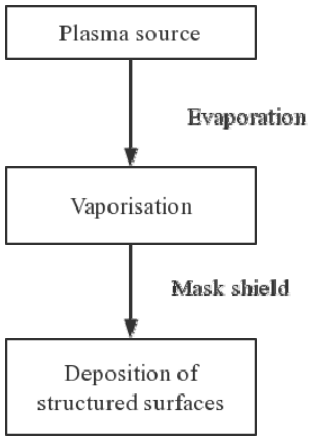

Fig. 2.2. Diagram of plasma-based process.

2.2.2 Removing Material Techniques

Laser texturing, mechanical texturing methods and chemical etching methods are the most common used methods to form structured surfaces with removing the local materials away. During laser processing, melting and vaporisation of the substrate material occurred in contact with the laser beam, and in consequence removing the molten material away from the patterned area. The depth and aspect ratio of micro and nano structures are highly depended on the laser pulse duration, wavelength, and laser energy. Higher power and longer wavelengths were used to increase the texture dimensions and pattern complexity. Another important characteristic in laser techniques is the thermal effect of the radiation area on the substrate with the contact of laser beam, resulting in the metallurgical properties of the substrate material

changed through the heating of laser beam.

A variety of different laser technologies were employed for the surface modification of kinds of implant materials. Laser-based machining was reported for the modification of dental implants by investigators. For instance, Minamizato manufactured many tunnels with the same feature size in zirconia blades to achieve the implant dental roots by the use of Nd:YAG laser machining [61]. As noted by Kasemo et al., the controlled structures with the feature size of 1 μm were fabricated on implant surfaces by laser machining. The topographical attributes affected the morphology and response of cells at the tissue formation [62]. Pulsed laser deposition was employed to deposit hydroxyapatite coatings on metal surfaces which improved the mechanical properties and the biological properties of implant biomaterials [63]. However, pulsed laser deposition is hardly to fabricate structures with high aspect ratios or complex geometries uniformly [64]. Laser texturing technologies provide the methods for the modification of various substrate materials such as metal, alloy, stainless steel, silicon and polymers with variety of patterned structures. On the other side, laser texturing methods have the limitation of expensive equipment and high controllable operating process.

Chemical etching is an efficient way for the material removal in order to texture various materials such as silicon [65], Cu [66], steel [67] and Ni, the process was shown in Fig. 2.3. Dry etching methods such as reactive ion etching (RIE) [68], plasma etching [15], and gas-phase etching require expensive equipment and more complicated procedures. In contrary, wet etching is a low cost method to etch the substrate area without mask protection with only chemical reactions taking place. However, the processing time of chemical etching is based on both mask formation

and etching speed.

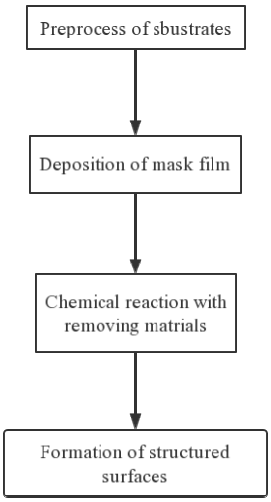

Fig. 2.3. Diagram of chemical etching process.

Methods based on mechanical removing action are usually preferred to high temperature technologies due to the thermal damage reduction of the substrates. Rotary ultrasonic machining (RUM) is sometimes employed to texture hard and brittle materials such as Ti alloys and ceramics to reduce the manufacturing cost comparing with laser technologies. One of the key disadvantages is the limitation of materials selection, as very hard materials could not be modified due to the micro-drill. The other is the texture dimension. They are both strongly depended on the micro-drill dimension.

2.2.3 Heat Treatment Techniques

Heat treatment is an effective method to alter the mechanical properties of implant alloys. It is noted by Zheng that the micro structured surfaces have a strong effect on the mechanical properties of β Ti–Mo alloys depending directly on alloy composition and the processing methods to which the alloys are subjected [69]. The tribological behaviour of Ti alloys strongly depends on the microstructures of the surfaces and the heat treatment. Composition and cooling rate were investigated on the microstructures and mechanical performance [70]. The suitable heat treatment processes could achieve the strengthening effect in alloys, which induced the transformation of metastable phases into α phase [71]. The correlation between composition, aging heat treatments, microstructure feature sizes and mechanical properties of implant alloys has been investigated by lots of researchers because it is the foundation for developing and improving new alloys for implant biomaterials [72].

A great deal of research efforts of micro and nano fabrication have been attributed towards realizing the surface modification technologies which depend on the specific requirements and productivity. It should be noted that in numbers of methods, multiple processes were implemented to achieve the target functionalities of the implant materials. Each method has its limits and advantages and they must make choices based on the various applications. With boundaries of biomedicine constantly being challenged and modified, Table 2.1 shows advantages, disadvantages and special potential of each technology.

Table 2.1 Advantages and disadvantages of the technologies.

Technologies	Key criteria						Applications
	Various materials	High resolution	Flexible pattern	High controllable	Low cost	High efficiency	
Heat treatment					√	√	Mechanical properties
Laser technologies		√	√				Biocompatibility and mechanical properties
PSM	√		√				Biocompatibility and mechanical properties
CVD	√	√					Mechanical properties, electronics and photovoltaics
PVD	√		√				Tribological and microelectronic applications
Chemical etching	√				√		Tribological applications and self-cleaning properties

As description of the mentioned technologies for their applications, they should be split into two categories: improving mechanical properties and altering chemical performances. It is significant to demonstrate that for a specific application, the fabrication technique should be properly selected in order to satisfy cost-effectiveness and texture geometric parameters. The selected manufacturing technology for implant materials surface modification should be considered in according with the following criteria: compatibility with the geometrical characteristic and feature dimensions of processed work pieces; compatibility with the structured design and fabrication process; high controllable and good repeatability compared with the above methods, DLIL nanomanufacturing technology can alter the mechanical properties and chemical performances at the same time on various materials over large areas. Due to

the unique capabilities provided by DLIL, it is necessary to be researched and further developed.

2.3 Laser Interference Lithography

Laser interference lithography (LIL) is a maskless, noncontact lithography technology. It is, in particular, suitable for large-area fabrication of controlled patterns with two-dimension or three-dimension functional structures in micro and nano scales. Laser interference lithography uses the interference pattern generated from two or more coherent laser beams for the modification of materials. The interference pattern is the superposition of electric field vectors of interfering beams. Arrays of laser beam lines, dots or various distributions can be formed on the biomaterial surface to achieve specific surface properties. Different patterns can be achieved by LIL via controlling the process parameters, such as incident angles of beams and wavelength, polarisation directions, laser fluencies and exposure durations. The period of the structures can be determined by the incident angles [73]. Nano gratings can be achieved by two-beam interference lithography. According to the principle of two-beam LIL, the period of the grating is given by $p = \lambda / 2\sin\theta$. So the feature size in the nanoscale can be achieved by using a laser source of short wavelength and large incident angles

For fabrication of three-dimension structures, the multi-beam laser interference is much more flexible than two-beam laser interference with double exposures, which can form a pattern in one step and suitable for large-area applications. With respect to multi-beam LIL, the polarisation also plays an important role in interference patterns.

Three different polarisation modes of four-beam LIL were demonstrated in order to investigate the effects of polarisation on multi-beam laser interference according to the theoretical analysis, simulations and experiments [74]. The moth-eye structures were fabricated by six-beam LIL on silicon by our research group [75]. Zhang et al. fabricated the micro and nano structures with excellent antireflection performance by four-beam LIL on silicon for the application in optoelectronic devices [76]. It is realized that more and more innovative and significant applications will be found in functional surfaces.

LIL can be divided into two categories: Direct laser interference lithography and indirect interference lithography. Indirect interference lithography required a pretreatment of coating a photosensitive resist thin film which is used to transfer the geometric pattern to on substrates. It is always applied on polymer materials. DLIL can be used to modify various biomaterials for investigation of cell response and tissue engineering. Compared with indirect interference lithography, DLIL is a more effective method for the surface modification of materials for the applications in biomedicine. For biomedical applications, control of the distribution of the nanomaterials onto substrates is as essential as precisely controlling their size. One interesting market is that the well designed structures can improve significantly the performance of the materials, which do not have the required topography and perfect surface properties. Structured surfaces in micro and nano scales do not only exhibit unique properties, but also act as intelligent surfaces capable of selective influencing multiple functionalities of applications in biological implants. The two-beam direct laser interference patterns have been fabricated to mask the electro-deposition of platinum nanoparticles into periodic arrays [77]. The direct laser interference

patterning technique was also employed in creating topographical architectures on the surfaces of the multi-walled carbon nanotube-based coatings deposited on borosilicate glass [78]. The method allows the production of nanostructured patterns that are useful in various research fields with the advantages of the well defined cross-scale structures in the micro and nano scales which can be achieved in a few seconds. Surface topography design by direct laser interference structuring on titanium and polyimide represents a facile method to gradually and endurably tailor the wettability of metals and polymers [79]. It could be demonstrated that direct laser interference structure has great potential in sustainably tuning wetting characteristics by structured surfaces. Periodic patterned surfaces were fabricated by direct laser interference patterning on metals to investigate the tribology property for the applications in industry [80]. Surface engineering techniques provide effective methods to fabricate advanced topographies that can be used to study the cell response and tissue engineering in biomaterials. Polymers and copolymers are the widely used materials in biomedicine, which have been developed with the functional topographies fabricated by direct laser interference patterning [81, 82]. Thermal properties of polymers were measured for the simulation in order to analyze the target polymers. Additionally, single laser pulse experiments were carried out to calculate the optical parameters of the polymer surfaces which are needed to develop the analytical model and the thermal simulations. Polymer surfaces with patterned structures were investigated to control biological cell growth and orientation [82].

In the mentioned applications of DLIL, surface topography design by one-step DLIL represents a facile method to gradually and endurably tailor the mechanical performances, chemical properties, cell responses and tissue engineering of biological

implants. The brief literature review of DLIL revealed that it has a few advantages compared with the forementioned technologies which are highlighted in the following points. The advantages of DLIL for surface modification can be concluded as follows:

- High production rate - DLIL technology can increase the peak light intensity over the ablation threshold of materials by adjusting the laser distribution instead of the focusing system. It is a parallel fabrication method and a primary processing area can achieve over 0.5 cm^2 and even more so that the periodic patterns in micro and nano scales with a well-defined cross-scaled fabrication can be implemented in a few seconds.

- Simple processes - As mentioned previously, a direct laser interference system consists of a high power pulsed laser source and several optical components including beam splitters and high-reflective mirrors which are used to divide the laser source into two, three, four or more coherent beams. Additionally, wave plates and polarisers are employed to control the phase and polarisation of each interference beam. The system can be set up in air condition and the fabrication process requires only single technological procedure compared with other methods.

- Highly controllable - Various interference patterns with different shapes, sizes and periods can be achieved by setting up multi-beam laser interference systems which depend on optical setup geometry and used laser wavelength. By adjusting the process parameters, DLIL is able to create different structured surfaces with specific feature sizes according to the required functionalities in target applications. In addition, the 3D structured process is flexible to modify materials

on irregular surfaces with high resolution positioning. The highly controllable patterns and positioning are the unique advantages of DLIL for surface modification in biomedicine.

- Suitable for various materials - The high power pulsed laser and semiconductor laser can be used to fabricate structures directly on metals, alloys, semiconductor materials and various kinds of polymers. High absorbance of different materials at a specific wavelength of laser source allows the reduction of the laser intensity required to obtain a determined structure depth.

2.4 Summary

This research focuses on developing DLIL technology for controllable, low cost and high efficient manufacturing of micro and nano structure surfaces and components with proper functionalities for applications in biomedicine. Coverage includes the structure design, process control and characterization of the modified surfaces. DLIL can alter the surface composition and properties of biomaterials in a well-designed and highly controllable way, which makes it efficient and cost-effective for surface modification. Compared with other methods, laser interference lithography has relative short processing time and is suitable for large-area surface modification on the micro and nano scales.

The laser intensity distribution modulated by coherent beams is transferred to the substrate surface to form periodic structures directly by a high-power laser. The

structures can be fabricated by controlling DLIL process parameters such as the wavelength, incident angle, polarisation direction, laser fluence and exposure time. DLIL offers its innovation to fabricate controllable micro and nano structures with well-defined cross-scale patterns and functionalities on various materials, which allows the production of very precise structures from the nano scale to micro scale uniformly and over large areas.

CHAPTER 3

FUNCTIONAL SURFACES FOR BIOMATERIALS

3.1 Superhydrophobicity

3.1.1 Background Knowledge

Superhydrophobic surfaces found in nature, for example, the surface of lotus leaves, demonstrate excellent water-repellent and self-cleaning properties, and have inspired the development of artificial superhydrophobic surfaces for various applications. Research has found the hierarchical structures formed with micro structured papilla cells covered by a nanostructure of hydrophobic wax crystals on the surface of the leaves [83-86]. The structures force water droplet to form almost spheres. Research also found that the papillae cells were in random distributions (as shown in Fig 3.1 (A)), the diameter of the cell ranges from 5 μm to 9μm (as shown in Fig 3.1 (B)), and the contact angle (CA) was about 161° [87].

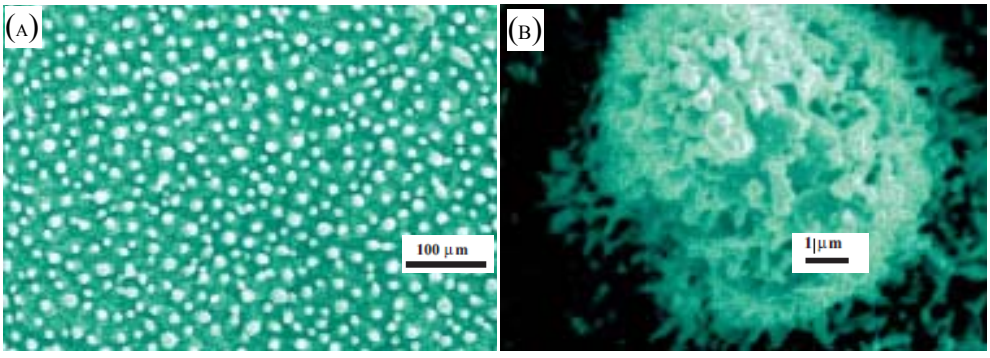

Fig. 3.1 (A) Scanning electron microscope (SEM) image (low magnification) of the surface of a lotus leaf; (B) Close-up image of a single papilla selected from (A) [87].

Further research has been undertaken on the effect of the micro and nano structures on water-repellent. It has been discovered that the rough solid surfaces consisting of hierarchical micro and nano structures trap air films between the droplet and the surface, leading to the reduced solid-liquid contact area and shear stress of the liquid. Fig. 3.2 illustrates such effect of the structures. The contact area can be divided into two areas. One is the convex-shaped areas where the liquid contacts the solid surface, known as the solid-liquid interface. The other is the flat areas above the valleys, known as liquid-vapour interface because the air is trapped in the valleys. The existence of the trapped air reduces the contact area of solid and liquid or equivalent and the adhere force between the two, causing the liquid more easily moving away from the surface. More precisely [85],

$$A=A\times f_{sl}+A\times f_{lv} \tag{3.1}$$

where A is the contact area, and f_{sl} and f_{lv}, called factional solid-liquid area and fractional liquid-vapour area, stand for the portions of solid-liquid interface and liquid-vapour interface, respectively. $f_{sl}+f_{lv}=1$.

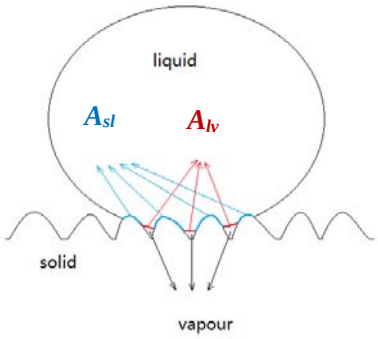

Fig. 3.2 Diagram for rough composite interface of solid, liquid and vapour: A_{sl} is solid-liquid contact interface and A_{lv} is liquid-vapour contact interface.

Fig. 3.2 also implies the relationship between f_{sl} and f_{lv} and the density of asperities, aspect ratio (defined as the ratio between the height and the width of aspects), and the

geometrical structure (meaning the shape including cone, cylindrical-shape, rectangular-shape, etc.). f_{lv} is proportional to the density of asperities, aspect ratio. The first item of (3.1) can be further expanded as

$$f_{sl} \times A = (A_{sl}/A_f) \times A \tag{3.2}$$

where A_{sl} is the convex-shaped solid-liquid contact area and A_f is its projection. The ratio of A_{sl}/A_f is called surface roughness factor, denoted as R_f, as it reflects the roughness of the surface. R_f, is related to the aspect ratio and the geometrical structure.

CA is the measure used to evaluate wettability of surfaces. On a perfect smooth solid surface, CA as denoted as α_0 in the diagram is the angle between the solid surface and the tangent line of the droplet as shown in Fig. 3.3. The shape of the droplet is determined by the interfacial tension of the three forces.

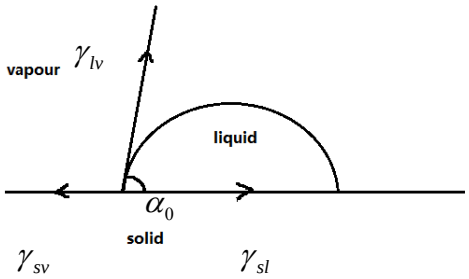

Fig. 3.3 Contact angle (CA) of a droplet on a smooth solid surface.

Given a perfect smooth solid surface, CA can be calculated using Young' equation [88].

$$\cos\alpha_0 = \frac{\gamma_{sv} - \gamma_{sl}}{\gamma_{lv}} \tag{3.3}$$

Where α_0 is the Yong CA, γ_{sv} , γ_{sl} and γ_{lv} are the solid/vapour, solid/liquid and liquid/vapour interfacial free energies, respectively.

Young's equation has the limitation on perfect smooth solid surfaces. Wenzel model

[89] is an attempt of determining CA for rough solid surfaces. The model was developed based on the so-called Wenzel model [90] which considers liquid contacting all parts of the surface, as shown in Fig. 3.4 [90].

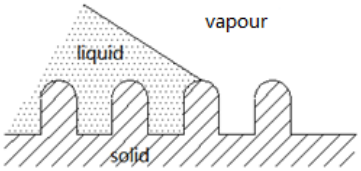

Fig. 3.4 Wenzel model: liquid is wetting on a rough surface.

With this model, CA is calculated as the followings [89]:

$$\cos\alpha = \frac{dA_{lv}}{dA_f} = \frac{dA_{sl}}{dA_f}\frac{dA_{lv}}{dA_{sl}} = R_f \cos\alpha_0 \tag{3.4}$$

$$R_f = \frac{A_{sl}}{A_f} \tag{3.5}$$

where A_{lv} is the contact area of liquid and vapour, A_{sl} is the contact area of solid and liquid, R_f is the roughness factor defined as the ratio of the contact area of solid and liquid A_{sl} to its flat projection A_f. α_0 is the Young CA defined for a perfect flat surface.

Cassie-Baxter model [83] describes a composite surface where air pockets are formed because air is trapped between liquid and solid, as illustrated in Fig. 3.5 [90].

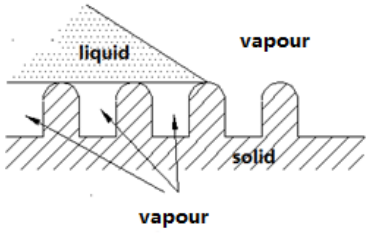

Fig. 3.5 Cassie-Baxter model: air pockets formed in cavities between rough surfaces and liquid.

Given a rough solid surface composed of f_{sl} with contact angle of α_1 and f_{lv} with contact angle of α_2, CA is calculated as below [91]:

$$\cos\alpha = f_{sl}\cos\alpha_1 + f_{lv}\cos\alpha_2 \tag{3.6}$$

Let $\alpha_1 = \alpha_0$ and $\cos\alpha_2 = -1$ to have CA of the air film to be 180°. Cassie-Baxter model can be rewritten as

$$\cos\alpha = R_f\cos\alpha_0 - f_{lv}(R_f\cos\alpha_0 + 1) \tag{3.7}$$

It can be seen from Eq. (3.7), CA increases with an increase in f_{lv}. Nosonovsky and Bhushan demonstrated that an increase in the density of asperities led to the increase of CA and higher aspect ratios caused CA to increase faster [92].

Table 3.1 gives the classifications of wettability of solid surfaces according to CA. Surfaces with CA greater than 150° has the superhydrophobic property which provides excellent repellence and self-cleaning functions.

Table 3.1 Different contact angles and their corresponding wettability.

Contact angle	Wettability
$0° < \alpha \leq 5°$	Superhydropholicity
$5° < \alpha < 90°$	Hydropholicity
$90° \leq \alpha < 150°$	Hydrophobicity
$150° \leq \alpha < 180°$	Superhydrophobicity

3.1.2 Realisation of Superhydrophobicity

Previous studies have found that surface wettability has a significant role in the early stages of cell response, adhesion, spread, proliferation and differentiation [93]. Superhydrophobicity as the highest anti-wetting ability has been recognized as a crucial surface property of implant materials. Superhydrophobic surfaces have a number of specific functions for biomedical applications, including antibacterial and anticorrosion performances [94, 95]. Most implant materials currently in clinical use have hydrophobic surfaces according to the recent research [96]. Superhydrophobic surfaces have become particularly desirable because of their stable antibacterial property. Their excellent water-repellence and self-cleaning performances make it possible to prevent bacteria to grow and to spread on the surfaces. Freschauf demonstrated that superhydrophobic surfaces, obtained via structural modification reduced bacterial growth on flat surfaces [97].

Techniques that fabricate rough solid surfaces with micro and nano hierarchical structures to implement superhydrophobicity for the surfaces can be classified into 3 categories, namely chemical-based techniques, physical-based techniques and physical-chemical conbined methods.

Chemical-based methods

Chemical-based techniques such as electropolymerization [98], chemical vapour

deposition [99], sol-gel method [100], galvanic cell reaction [101] and chemical etching [102] have been developed for the fabrication of superhydrophobic surfaces. The electropolymerization method was used to prepare large-area superhydrophobic films by adjusting the process parameters including cycle numbers, applied voltage and monomer concentration. For the process of electropolymerization method, counter and reference electrodes were used to electrolyze the electrolyte, and the monomer was added to the electrolyte. Electropolymerization of polymer was then carried out on the working electrode surfaces (target surfaces) by cyclic voltammetric sweeps with the applied voltages of electrode. The thickness of the deposited polymer was depended on the cycle numbers, applied voltage and monomer concentration [98]. For CVD method, the selected precursor is heated to vapour and the monomer molecules are activated to generate the radicals which undergo chemical absorption and bonding for the polymerization reactions. The dielectric barrier discharge micro jet system is employed for the hydrophobic coating. The deposition conditions including electrode-substrate gap distance and reacted time have their effect on the size and shape of the film surface which influences the CA of coatings [99]. In the process of sol-gel method, the organic, inorganic and organic-inorganic hybrid sol-gel materials have been used to fabricate the superhydrophobic coatings on various materials. A high temperature is needed to burn out the sol-gel materials used to induce the phase separation and coagulate the colloidal materials for the coatings covered with organic groups which make them hydrophobic. The formulation of reagent for coagulation and the reaction time have its effect on asperity density of microstructures [100]. The galvanic cell reaction as one of the electroless method is used to create metal nanostructures through the formation of local galvanic cells between the materials and the metallic ions in hydrofluoric acid (HF) solution. The

asperity density of nanostructures can be controlled by the reaction time and the concentration of the metallic ion [101]. The chemical etching method is the process of removing the materials on a metal surface by a chemical reaction between the metal materials and etchant for the creation of rough surfaces with superhydrophobicity. The density of asperity of rough surfaces is depended on the reaction time and concentration of the etchant [102].

An et al. [90] fabricated the hierarchical multi-scale mimetic lotus leaf structures on a stainless steel mesh surface. As shown in Fig. 3.6, the electropolymerization and chemical polymerization were used to coat the micropapilla structure and nanofiber on mesh surface. With the Teflon treatment, the multi-scale hierarchical structures showed the superhydrophobic property. Hosono et al. [103] provided the bottom-up process to obtain a superhydrophobic surface with CA value of 178° on metal hydroxide combined with chemical bath deposition (CBD). The controlled growth of aligned carbon nanotube arrays were used to achieve hydrophobic surface with coating fluorocarbon and ZnO films [104, 105]. Shirtcliffe et al. demonstrated the chemical etching and electro deposition method to obtain the rough copper surface with nanostructures. The mask was used to etch the copper surface for the micro structure and electro deposition was employed for the nanostructure [105]. The galvanic cell reaction was provided to deposit Ag nanostructures on the silicon wafer through a chemical way to achieve the surface with the superhydropbobic property [101]. The roughness silica film was obtained using coagulated colloidal silica [100]. Qian et al. developed chemical method to etch polycrystalline metals and fluoroalkylsilane was used for hydrophobization. [102]. Guo et al. fabricated the flower-like nanostructures on copper surfaces through a two-step self-generation

method with the process period of about 15 days [106].

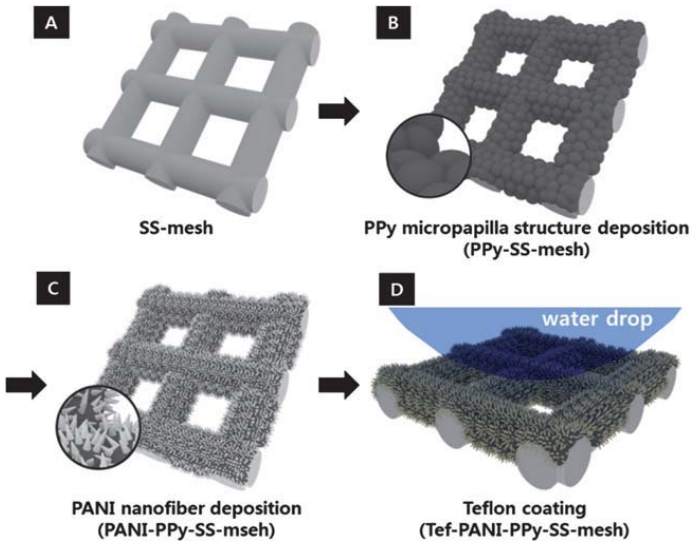

Fig. 3.6 Schematic of fabricated process of superhydrophobic surface consisted of stainless steel mesh covered by multi-scale hierarchical structures. (A) Stainless steel mesh fabricated by organic cleaning; (B) Polymerizing polypyrrole microstructures deposition by electropolymerization; (C) Polyaniline nanofiber deposition by chemical polymerization; (D) Teflon modification by dip coating [98].

A lot of chemical-based methods have been used to achieve the superhydrophobic property. However, the complex process control, multi-step procedures are required in many cases. It is hard to modify the irregular-shaped surfaces with the controllable geometrical shape and aspect ratio of roughness for most of the methods.

Physical-based methods

The rough surface with micro structures also can be obtained by photolithography [33] and electroplate [107], combined with plasma etching [33] and physical vapour deposition [108], and the nano scale structures have been created on microstructures in order to achieve the superhydrophobic hierarchical micro and nano structures. Photolithography is a process used to transfer the geometric pattern by the photo mask (optical mask) to a photoresist (photosensitive resist) thin film. The size and shape of geometric structures are depended on the optical mask (expensive cost) and operation conditions including exposure time and releasing force. In the electroplate process, the high purity metal plate was set as the counter electrode, and the electroplating solution was used for the electrodeposition of metal ions for the formation of metal film. The current power, current density and reaction time influence the size and shape of the structures of film surfaces. For the plasma etching, the substrate is exposed to the plasma source (bombardment ions), the vaporisation occurs with removing materials for the fabrication of micro and nano structures. The main factors that influence the plasma etching are the concentration of plasma source, pressure, vacuum and etching time. PVD methods are used to produce thin films and coatings by sputtering and evaporation. The source is heated to the vaporisation temperature by a high-power electric arc discharge and electron beam, and the highly ionized vapour is generated and deposited by the variety of vapour pressures on the target surfaces. The process can be seen in Fig. 3.7. The pressure and processing time are the critical factors for the thickness of film.

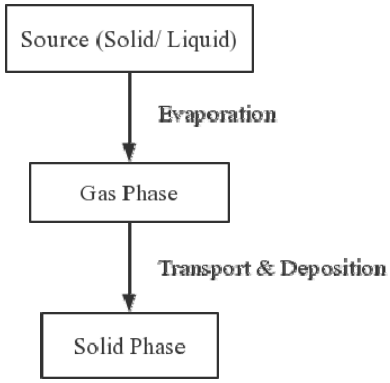

Fig. 3.7 Diagram of PVD process.

Sun et al. proposed interference lithography method to fabricate hierarchical polydimethylsiloxane (PDMS) microstructures with plasma treatment procedures [33]. Wu et al. used laser interference lithography to modify the surface with controllable anisotropic wettability [109]. They studied the wettability of grooves with different feature sizes and achieved the hydrophobic surface with the CA of 131°.

Physical-chemical combined methods

Laser texturing technologies [109] and photolithography [33, 109] were used to fabricate micro and nano structures combined with the low surface energy treatment to achieve the superhydrophobic surfaces. Laser texturing is the process of using the laser beam to irradiate the target materials and fabricate structures by melting and vaporisation. The size of the structure is depended on the laser source, wavelength and

processing time. The low surface energy treatment was employed on the hydrophobic structures by modification of low surface energy functional groups to obtain the superhydrophobic surfaces. E. Stratakis modified artificial surfaces with the superhydrohpobic property of the natural lotus leaf. A femtosecond laser was used to fabricate hierarchical structures on a silicon surface under a reactive gas atmosphere combined with a proper hydrotreatment [109]. The aligned carbon nanotube films were coated on the silicon surface and created the rough silicon surface by chemical vapour deposition, respectively, the schematic description has been shown in Fig. 3.8. It is demonstrated that the nanoscale structures have the positive effect on reducing the strict requirements for the asperities density and aspect ratio design of micro structures for the superhydrophobic surfaces [104].

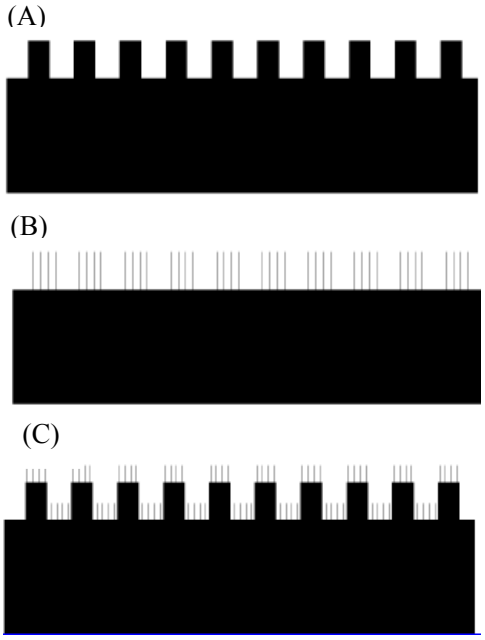

Fig. 3.8 Schematic of (A) micro structures fabricated by photolithography; (B) Aligned carbon nanotube grown on silicon surfaces according the model of (A); (C) Aligned carbon nanotube grown on the patterned silicon surfaces [104].

Previous research makes efforts on the superhydrophobic performance of hierarchical micro and nano structures. Further chemical treatments are required after the process for fabricating superhydrophobic surfaces to reduce the surface energy. Table 3.2 compares the technologies for the formation of superhydrophobic surfaces. The chemical-based methods are developed for various materials which required stringent conditions and complex process control during the multi-step procedures. The preprocess is also required for both chemical- and physical-based methods. Most of the methods require complicated conditions or multi-step processes to obtain the uncontrollable or undesirable structures. Therefore, a cost-effective approach for the creation of well-designed dual structures with superhydrophobic property is expected.

Table 3.2 Comparison of techniques for the fabrication of superhydrophobic surfaces.

Technique / Criteria	Chemical-based techniques	Physical-based techniques	Chemical-physical combined techniques
Fabrication processes	Multi-step procedures	Multi-step procedures	Relative short procedures
Process conditions	Complicated	Simple	Relative simple
Materials	Various materials	Limitations of materials	Various materials
Controllable of structures	Not good	Not good	Good
Stability of structures	Not good	Good	Good

3.2 Wear Resistant Property

3.2.1 Background Knowledge

In biomedicine applications, implant materials need to possess the property of wear resistance. Most implant applications may be classified to the artificial bone for joint replacement and the artificial tooth as “dental implant”. Artificial bones in orthopaedic applications are often used as structural enforcement which is inserted inside corpus [117]. They lay more weights on mechanical properties such as strength, toughness, and torque which have special requirements for abrasion resistance in the sense of tribology. Such implantations face two critical issues. One is loosening and the other is corrosion. The motions of artificial bones relative to natural parts of human body cause wear on the surfaces of implant materials. Debris are generated during the wear process [9]. Corrosion causes human suffering and reduces the life of artificial bones. The micro dimples (cavities or pockets) were formed in a distributed pattern on the bearing surfaces for the formation of a lubricant film to separate the contacted surfaces in relative motions [110, 111]. Numbers of research indicated that surface modification with micro dimpled structures plays the role as miniature hydrodynamic bearings and separating the sliding surfaces by creating a net pressure resulting in the increased thin lubricant film. The lubricant film provides the additional pressure and increases the separation between the sliding surfaces, resulting in the reduction of friction [112]. For the identical dimple shape of circle and with the condition that the lubricant is air at room temperature, the hydrodynamic lubrication regime can be expressed by Reynolds stress equation [113].

$$\frac{\partial}{\partial X}(PH^3\frac{\partial P}{\partial X})+\frac{\partial}{\partial Y}(PH^3\frac{\partial P}{\partial Y})=\frac{6\mu r_p U}{p_0 c^2}\frac{\partial (PH)}{\partial X} \tag{3.8}$$

In Eq. (3.8), $X=x/r_p$, $Y=y/r_p$, $P(X, Y)$ is the non-dimensional local bearing pressure, and $H(X, Y)$ is the non-dimensional local bearing spacing. p_0 is the air pressure, c is the minimum bearing spacing, U is the relative sliding velocity, μ is the air dynamic viscosity, and r_p is the radius of dimple, as shown in Fig. (3.9) [113].

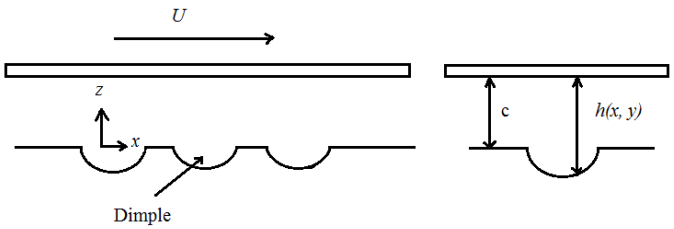

(A)

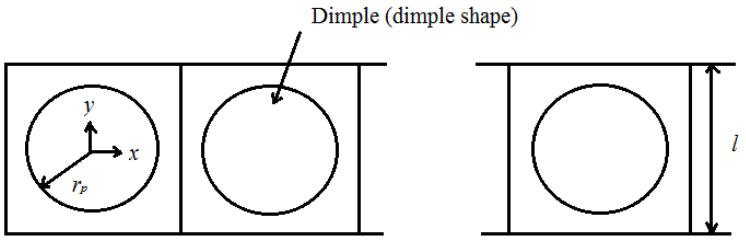

(B)

Fig. 3.9 Model of a dimpled structured slider bearing diagram. (A) A cross-sectional view; (B) Top view [113].

The friction in the air bearing process for sliding surfaces is driven by the shear stress and the average shear stress τ is approximated by [113]

$$\tau=\frac{\mu U}{c+\frac{V_d}{A_d}} \tag{3.9}$$

In Eq. (3.9), V_d is the volume of a dimple and A_c is the area of its unit cell.

The presence of the dimple structures causes the formation of extra bearing spacing between the sliding surfaces which have the effect of reducing the friction coefficient by means of the dimple structures . The friction coefficient f is expressed as [110]

$$f = \frac{\tau}{p_d - p_0} \tag{3.10}$$

where p_d is the average bearing pressure. The dimple sizes including area density (defined as the ratio of area of dimple shape and area of its unit cell) and shape are the critical factors for the magnitude and trend of the friction coefficient [110].

The abrasive wear occurs when the modified surfaces with micro dimpled structures slid across a surface that is relatively softer in which the real contact area between sliding surfaces is small compared with the apparent area of contact, being limited to the contacts between surfaces [114]. The wear rate can be expressed by the following expression and the cumulative volume of material worn W is given by [115]

$$W = \frac{KLw}{3H} \tag{3.11}$$

where K is the wear coefficient, L is the sliding distance, w is the normal load and H is the hardness of material. It is found that the increased hardness can reduce the wear of the surface.

Both experimental research and theoretical analysis indicates that in the process of abrasive wear, the real number of contacts n is a function of the applied normal load, apparent contact area, hardness of the materials and mean diameter. The relationship

can be expressed by [114]

$$n = K_H D_0^{-2} \{w/H\}^{1/2} A_0^{1/2} \tag{3.12}$$

Where w is the normal load, H is the hardness of materials, D_0 is the mean diameter of abrasive particles, A_0 is the apparent contact area and K_H is a constant. The real contact areas are related to the number of contacts which is depended on the hardness of surface structure and the abrasive particles. The micro dimpled structures with different shape and density also have the effect on reducing the real contact area and trapping wear debris in contact zones. Fig. 3.10 shows the schematic diagram of the abrasive wear within the lubricant film. During the sliding process, dimples have the function of trapping the abrasive wear particles to make the particle removal action resulting in the reduction of the friction and wear [116].

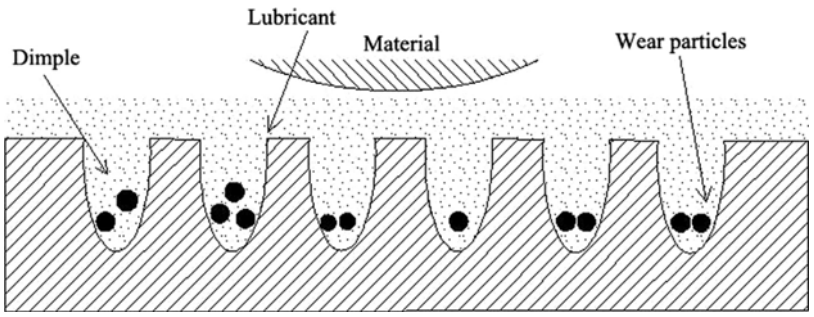

Fig. 3.10 Schematic ofthe abrasive wear for dimple structures with trapping particles.

3.2.2 Literature Review of Wear Resistant Property in Implants

For orthopaedics, implants are usually used as structurally enforced artificial bone which is inserted inside the corpus as so that the implants support more weight in

biological mechanical systems and require the wear resistant property [117]. Although the artificial bone has a relatively low friction coefficient, severe wear usually occurs on the bearing surface. Experiments have been carried out in order to reduce the artificial hip joint friction by the micro dimpled structures into ultra-smooth femoral heads [118,119]. Chyr et al. fabricated the dimple structures on the cobalt-chromium (Co-Cr) femoral head with the area density from 5% to 20% to investigate the friction reduction of metal-on-polyethylene (MOP) artificial hip joint. As shown in Fig. 3.11, the micro dimpled structures were fabricated on the femoral head of hip joint to reduce the friction between the acetabular and femoral head [4].

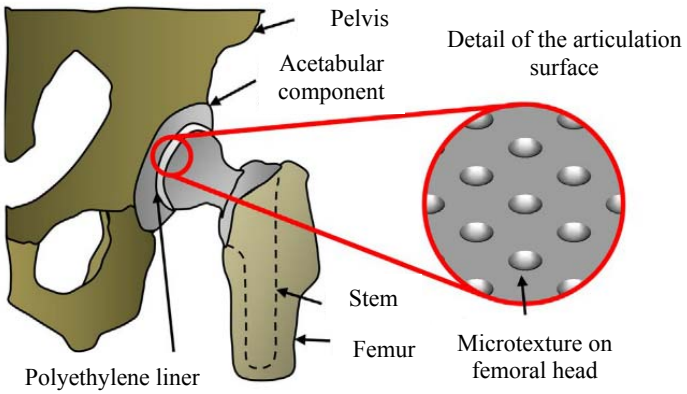

Fig. 3.11 Metal-on-polyethylene (MOP) artificial hip joint with dimple structured surfaces on the Co-Cr femoral head [4].

Ito et al. conducted the friction and wear rate tests to study the influence of a circular dimple structures on Co-Cr-on-polyethyene hip joints with the resulting that a 30% reduction of friction coefficient and 68% decrease of wear with the area density of 13.6% [120]. Roy et al. studied the tribological effects of micro dimpled structures with the purpose of applying it in total hip joint prostheses. The ceramic surfaces were modified by computer numerical control (CNC) micro-drilling to obtain dimpled

structures. The modified surfaces with the area density of 15% showed a significant improvement of metal-on-polyethylene wear resistant property, achieving 22% reduction of friction and 53% reduction of wear [121]. The previous experimental results indicate that for the given applied load and dimple shape, a higher area density leads to higher friction coefficient reduction. For different bearing materials, when the area density exceeds a certain value, the limit stress concentration effects occur and induce the surface damage [111].

Recent studies indicate that manufacturing methods for creating dimple structures aim to improve the wear resistant property by reducing the friction coefficient to overcome the friction for the applications in implants [122]. Various manufacturing techniques are developed including CVD [123, 124], shot peening method, and laser treatments [125-128]. Chemical vapour deposition can be used to form films with micro dimpled structures by exposing the substrate to the heated precursors, and the monomer molecules are activated to generate the radicals which undergo chemical absorption and bonding for producing a thin film on the substrate [123]. The mask shields are used during the deposition procedure to form the micro dimpled structures. The shape and density of dimples are depended on the reaction time and patterns of mask. For the process of shot peening method, the surface is bombarded by shaped media with sizes in micro and nano scales. This method is similar to blasting treatments but more controllable on peening power, intensity and direction which can be controlled for the desired sizes of dimple structures [129]. Laser treatment is the process of using the high power laser to strike the substrate and the dimple structures are formed by melting and vaporisation. The size of the dimple is depended on the laser source, wavelength and processing time [130].

Table 3.3 Comparison of techniques for the fabrication of micro dimpled structured surfaces.

Technique / Criteria	CVD	Shot peening method	Laser treatments
Fabrication processes	Multi-step procedures	Simple	Simple
Process conditions	Complicated	Simple	Simple
Materials	Various materials	Limitations of materials	Various materials
Controllable of dimple sizes	Good	Not good	Not good
Stability of structures	Not good	Good	Good

These studies have all successfully demonstrated that the micro dimpled structures can significantly overcome the friction in artificial joints. Different dimple shapes of structures have been studied and designed to reduce the friction coefficient of bearing surfaces which can be attributed to the fact that the dimples of the structured surfaces provide the additional hydrodynamic pressure. Although the design principle of micro dimpled patterns based on hydrodynamic theory has been well accepted, experimental and analytical studies carried out by different researchers suggest that in order to obtain the desirable wear resistant performance with a low friction coefficient, the well-designed micro dimpled structures need to be conducted on different materials

[122]. Table 3.3 compares the methods for the fabrication of dimple structures. The structured surfaces fabricated by most of the techniques have low stability and the processes of these methods required multi-step procedures with low controllable dimple sizes. Therefore, a proper manufacturing method for micro dimpled structures is imperative.

3.3 Biocompatibility

3.3.1 Background and Knowledge

Metallic biomaterials are usually used as the implant materials for various medical applications, as shown in Table 3.4. The stability or failure of the bone implants relies on a complicated combination of biological and mechanical factors which are closely related to the interaction between the implant surface and the surroundings [134]. Recently, efforts have been made to reduce the factors that lead to implant loosening [132]. The factors are mainly determined by the surface chemistry, composition and biomaterial surface texture [131, 132].

Table 3.4 Metallic biomaterials usually used in implant applications [133].

Metallic biomaterials	Applications
Cobalt-Chromium-Molybdenum (Co-Cr-Mo)	Artificial joints, heart valves and dental prostheses
Stainless steel	Vascular stents and orthopedic fixation

	plates
Titanium alloys	Dental prostheses, artificial joint components, heart valves, vascular stents, orthopedic screws and pacemaker cases
Gold or platinum	Dental fillings and cochlear implants
Silver-tin-copper alloys	Dental amalgams

Ti-6Al-4V alloys have been commonly used in orthopaedic and dental replacement due to their advantages in biological compatibility and corrosion resistance [135]. However, the incompatibility of cells caused the infection which induced the failure of the implants, leading to revision surgery or disability [136]. Cell behaviours including cell proliferation, cell spreading and cell adhesion are investigated to evaluate the biocompatibility of implant materials. Numbers of biological molecules including carbohydrates, cell-extracellular matrix proteins or their components such as arginine-glycine-aspartic acid and poly-L-Lysine have been considered to investigate cell behaviours at the molecular level, and research related on cells and the bottom surface in the micro and nano scales are needed to improve the biocompatibility of implant materials. Roughness micro and nano structures can have positive impact to the biocompatibility of materials, including cell proliferation, adhesion, spreading, morphology and orientation significantly. Grooved structures in micro and nano scale have the effect of cell spreading to reduce the formation of scar tissue and to promote bone bonding degree [137,138]. Micro and nano dimpled and dotted structures influence the cell proliferation and cell adhesion for the ability of cells to invade and colonize the artificial bone [139]. The roughness of structured surface is defined as the

microscopic geometrical property formed by the small clearance and the rises and falls on the machined surface. The arithmetic mean surface roughness (R_a) is commonly used to evaluate the surface roughness. As shown in Fig. 3.12, R_a is the absolute arithmetic mean of profiles deviated distance between each point of the surface profiles and the base line within a sample range of the part surface. The R_a can be calculated by [139]

$$R_a = 1/L \int_0^1 |Y(x)| dx \approx 1/n \sum_{i=1}^{n} |Y_i| \tag{6.8}$$

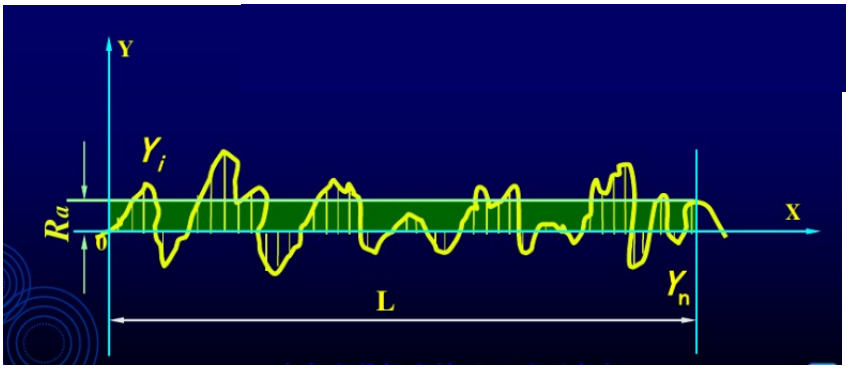

Fig. 3.12 Calculation of R_a [164].

It can be seen that the roughness of structured surface related to depth and topography of microstructures. In order to study the effects of micro and nano structures and surface roughness, various technologies have been developed to fabricate roughness structures in micro and nano scale on biomaterials.

3.3.2 Literature Review of Biocompotibility in Implants

The interaction of bone tissue and implant interface is attributed to three main principles. The first principle is the mechanotransduction concepts in bones. It is reported that the micro surface can improve the mechanical inter locking strength and the mechanical properties of the implant. At the same time, the micro surface increases the superficial area of the implant. The implant-bone interfacial shear strength can be improved because of a rough micro surface. The mechanical adaptation is a bioprocess. It requires a biosystem sensing the applied loading force. The force information is communicated to osteoblasts which produce new bionesor osteoclasts and destroy old bones [134,140]. The second principle is the theory of bone formation. The micro dimpled structure can help the fibrin blood clot deposit and fix the extracellular matrix on the implant surface. Micro dimpled structures create the stable micro environment which helps cell migration and grow tha long the extracellular matrix to the implant surface [141]. Meanwhile, the rough surface would contribute to the bone-implant interface orientated growth and adhesion of osteoblasts [142]. The third principle is the hypothesis of surface signals. Some researchers have proposed that extracellular matrix protein integrin could deliver the topography signals to the attached cells [143].

Many approaches have been made to alter implant surface topography and investigate the biocompatibility. Different methods including micromachining, polishing, surface blasting, surface coating [144], shot peening [145], acid etching, photolithography and laser texturing were used to produce micro textured patterns on implant surfaces. Omayra et al. obtained Ti-6Al-4V and TiAl disks with various surface roughness

values using the grit paper and diamond paste [146]. Chen et al. used laser to obtain micro grooved structures with required periods and depths [147]. Havlikova et al. combined the electric discharge machining, chemical milling and shot peening to treat the surfaces of orthopaedic implants [148]. Dalby et al. fabricated controlled patterns of 160 nm high nanocolumns using colloidal lithography [149]. Matsuzaka et al. obtained multi-grooved patterns on the 18-karat gold alloy with an ultra precise machine [150]. Meng et al. obtained hierarchical micro and nano structured titanium surfaces via electrolytic etching (EE) [151]. Li et al. proposed a method for the fabrication of bionic superhydrophobic zinc coatings with crater-like structures on steel surfaces [152]. However, most of the methods still have the potential of the osteoblast orientation that could lead to the scar tissue formation. The limitation of recent reviews is that researchers have tried to give a broader overview related to implant surface modification on biocompatibility but does not give any conclusion regarding the specific excellent biocompatible implant surface modification studied till now. In order to tailor desired interactions actively, the complicated processes and time consuming procedures with uncontrollable and undesirable structures are still challenges.

3.4 Summary

In this chapter, the conventional theory and applications in biomaterials for functional properties including superhydrophobicity, wear resistant and biocompatibility were briefly described, respectively. With the investigation of modification technologies of

functional surfaces in this chapter, apart from the complex procedures or multiple processes with the current methods, it is still quite challenge able to obtain a long term use of the artificial joints in terms of high wear resistance and biocompatibility. For a specific functional property, the design of optimum structures is complicated and unpredictable without the highly controllable fabrication method. Therefore, a proper effective manufacture of patterned micro structures is highly expected for the specific requirements. As mentioned in Chapter 2, DLIL has been developed to modify the stiff materials including metals, alloys and soft materials. Structured feature sizes including the geometrical shape, diameter, period and dimple density can be well-designed and controlled by adjusting the process parameters during the DLIL. With the efforts on functional modified surfaces on different materials [140-144], DLIL technology is being considered and evaluated for other artificial materials in biological applications. In this PhD research work, effects of different micro and nano structures with specific feature size and the superhydrophobic property, wear resistant performance and biocompatibility are demonstrated in the following chapters. The different functionalities are developed in the following 3 chapters according to the specific implant applications. In Chapter 4, the superhydrophobic property on silicon surfaces was obtained by DLIL. The deformation of bearing surfaces was caused by wear process during the relative motion. Therefore, in Chapter 5, the commonly used implant materials Co-Cr-Mo alloy (used for femoral head) was selected to study the improvement of the wear resistant properties with the modification technology of DLIL. The adverse reaction of biological surrounding cells and tissues with artificial implant caused fixation of artificial components. So the significance of cell behaviour for the improvement of biocompatibility to prevent implant loosening comes rather straightforward. In Chapter 6, the Ti alloy as the one of the most usually used insert

implant material for arthroplasty and dental implant was modified to obtain micro and nano structures to investigate the cell behaviours of MG63 osteoblasts cell.

CHAPTER 4

SUPERHYDROPHOBIC SURFACES ON SILICON BY DLIL

4.1 Principle

The fabrication of micro and nano structures with different aspect ratios (ratio of height/depth and width) and geometrical structures can be implemented by DLIL, also known as laser interference lithography patterning. The process contains the pattern formation step and the fabrication step.

In the first step, patterns in the sense of aspect ratios and the geometrical structure are formed by controlling the parameters of four-beam DLIL system such as azimuthal angles, polarisation directions and incident angles. Equations (2.1)-(2.3) give theoretical relations from the parameters of DLIL system to the parameters of micro and nano structures. Simulations are often run to adjust DLIL parameters for practical applications. Incident angle and wavelength play dominant roles to period which affects the width of pattern, whilst polarisation is major influential to geometrical structures.

In the second step, laser beams, generated by high power nanosecond laser, irradiate on the silicon surface, causing physical and chemical reactions which lead to ablation.

During the ablation of silicon, oxidation also happens between Si and O_2 which generates silicon dioxide (SiO_2) on the structures. SiO_2 can be removed by applying chemicals on the surface. When HF is applied to the surface in this work, the following chemical reaction takes place

$$SiO_2+4HF=SiF_4\uparrow+2H_2O \quad (4.1)$$

The reaction cleans out SiO_2 in such a way that it produces SiF_4 as gas and water. The duration of applying the chemical, known as cleanout time, is proportional to the amount of SiO_2 generated which is determined by exposure duration of laser process. However, no quantitative relation from exposure duration and cleanout time is reported, rather, cleanout time is decided by the rule of thumb in experiments.

4.2 Simulations and Experiments [153]

4.2.1 Simulations

Simulations were run with Matlab software which provides means to manipulate simulated laser beams in terms of incident angles, polarisation angles and azimuthal angles of DLIL to form interference patterns with different intensity distributions.

Four-beam interference was used to obtain the micro convex periodic structures due to its higher intensity distribution ratio of interference structures compared with three-beam interference. According to Eq. (2.8) and Eq. (2.9), the intensity distribution ratio of four-beam inference is 16, whilst that of three-beam is 9. A high intensity distribution ratio induces high aspect ratio of interference convex structures. Simulations were performed to optimize incident angle, azimuthal angle and polarisation angle and produce the desired convex structures. Different

microstructures can be obtained by adjusting the polarisation angles of coherent beams [74]. Micro convex structures can be obtained with the TE-TE-TE-TE mode. TE stands for transverse electric wave polarisation mode for interference beams which are presented by polarisation angles of $\psi = 90^\circ$. On the other hand, micro dimpled structures can be formed by the TE-TE-TM-TM and TE-TE-TE-TM modes. TM represents transverse magnetic wave mode with $\psi = 0^\circ$. Fig. 4.1 shows the simulated results. The intensity scale 1 to 7 is represented with colours from blue to red, as shown in the diagram. The areas with high intensity distribution will be removed and the blue areas with low intensity will be remained. Fig. 4.1 (A) shows the intensity distribution under the TE-TE-TE-TE mode. The convex structures will be formed by removing the areas with high intensity quantitatively according with the intensity variations, and (C) and (E) give the intensity distributions under the TE-TE-TM-TM and TE-TE-TE-TM modes, with the resulting that the dimple structures will be obtained, respectively.

Figs. 4.1 (B), (D) and (F) display intensity variations of the three structures, respectively. It can be seen in Fig. 4.1 (D), the intensity distribution under the TE-TE-TM-TM mode shows the best contrast and highest intensity, and the fringe-to-fringe spacing (spatial period) of modulation period of 6 μm was generated in the TE-TE-TE-TM mode as shown in Fig. 4.1 (F). It is demonstrated that interference patterns with different geometrical structures such as dots and dimples can be achieved by adjusting the polarisation modes. The TE-TE-TE-TE mode is suitable for the formation of convex structures and the TE-TE-TM-TM mode can be used to generate the dimple structures with high aspect ratios.

Different interference convex patterns of intensity distributions were obtained by

adjusting azimuthal angles. Simulation results are given in Fig. 4.2. Figs. 4.2 (A) and (C) are the results of non-centrosymmetric interference beams with the azimuthal angles of $\varphi_1 = 0^\circ, \varphi_2 = 80^\circ, \varphi_3 = 170^\circ$ and $\varphi_4 = 260^\circ$, and with the azimuthal angles of $\varphi_1 = 0^\circ$, $\varphi_2 = 100^\circ$, $\varphi_3 = 170^\circ$ and $\varphi_4 = 270^\circ$, and (E) is the result of centrosymmetric interference beams with the azimuthal angles of $\varphi_1 = 0^\circ$, $\varphi_2 = 90^\circ$, $\varphi_3 = 180^\circ$ and $\varphi_4 = 270^\circ$, respectively. Fig. 4.2 (B), (D) and (F) are the corresponding intensity variations..

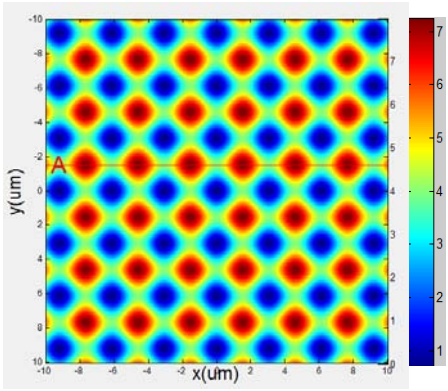

(A)

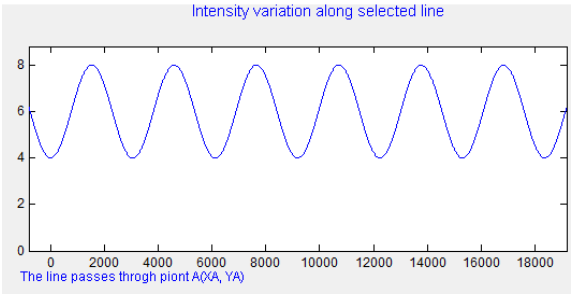

（B）

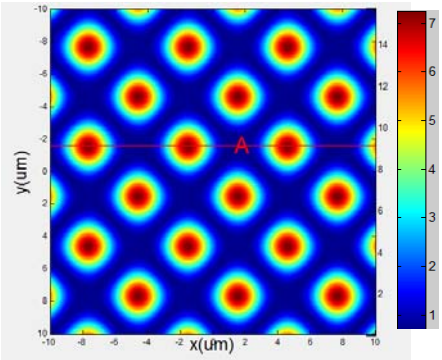

(C)

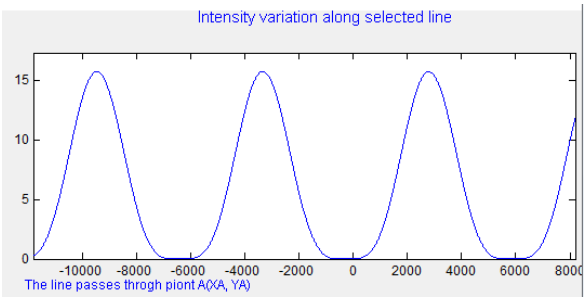

（D）

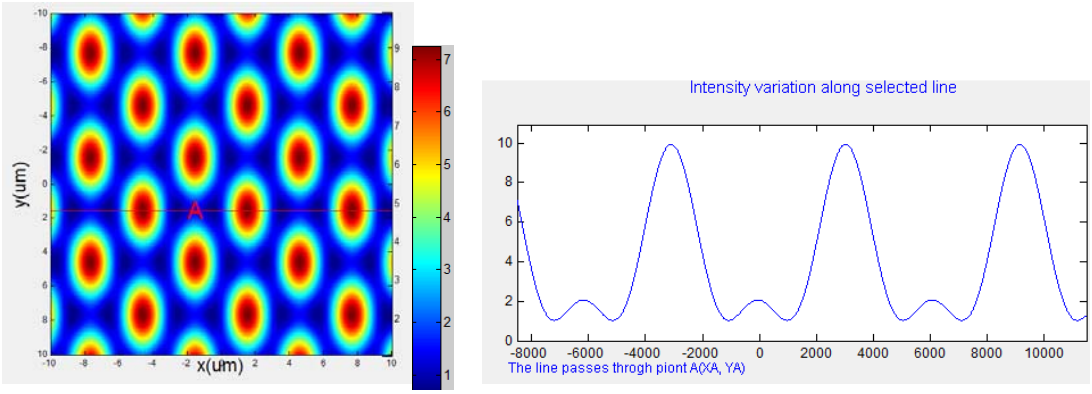

（E） （F）

Fig. 4.1 Four-beam interference simulated results.

As shown in Figs. 4.2 (A) and (C), obvious modulations are formed in the patterns and the period of the modulations is about 6 μm which can be seen in the corresponding intensity curves. According to the simulation results, the intensity modulations were generated when the four interference beams were non-centrosymmetric. The uniform intensity distribution patterns without modulations were formed due to a perfectly symmetric configuration of interference beams.

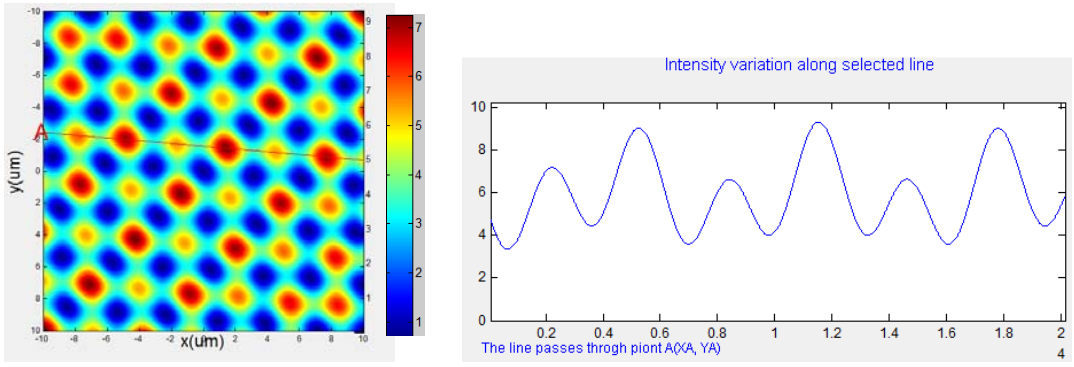

(A) (B)

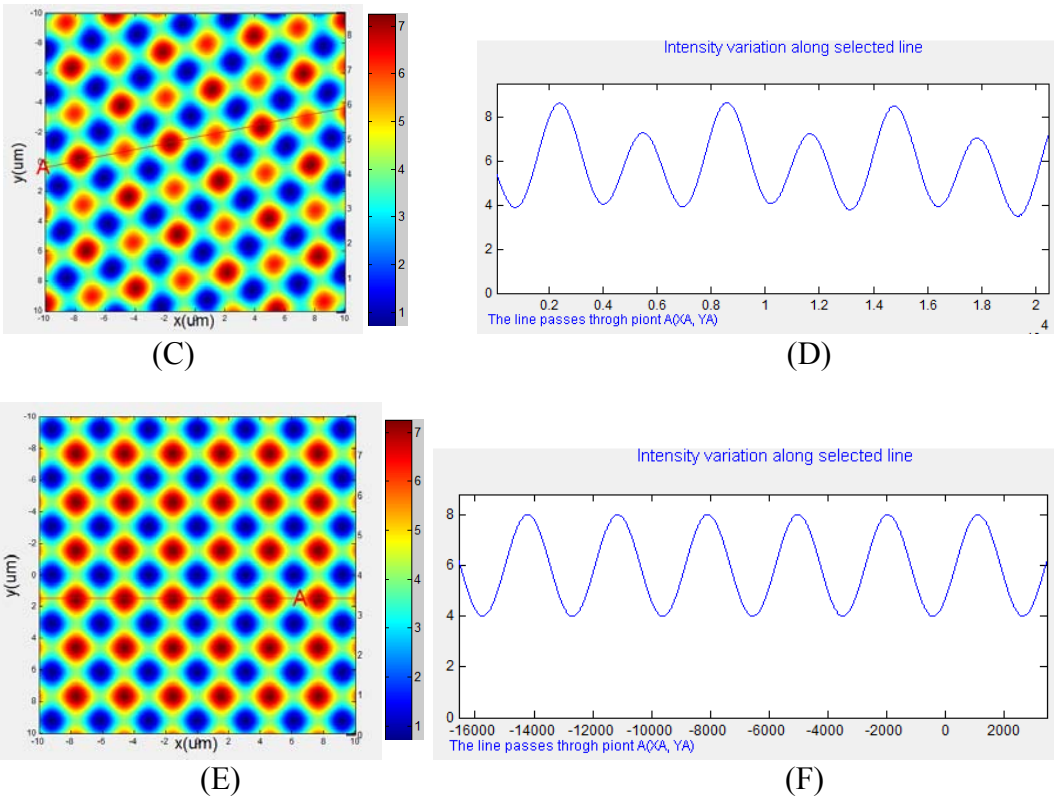

Fig. 4.2 Four-beam interference simulation results with different azimuthal angles in the TE-TE-TE-TE mode.

In order to obtain the convex structures with the cell diameter of 5.5 μm, the incident angle of 5.6°, which was calculated from Eq. (2.6), was used. The incident angles of 8° and 10° were used to simulate for comparison. The simulation results of uniform interference convex intensity distributed patterns with different incident angles were shown in Fig. 4.3. It can be seen that the spatial periods of x and y directions depend on the incident angles of interfered beams, and the different values of setting the incident angles induce the changes of shape and size of structure cells. The intensity distributed patterns with cell diameter of 5.5 μm were achieved by setting the identical incident angle of $\theta_1 = \theta_2 = \theta_3 = \theta_4 = 5.6^\circ$, which was in accordance with the theoretical value.

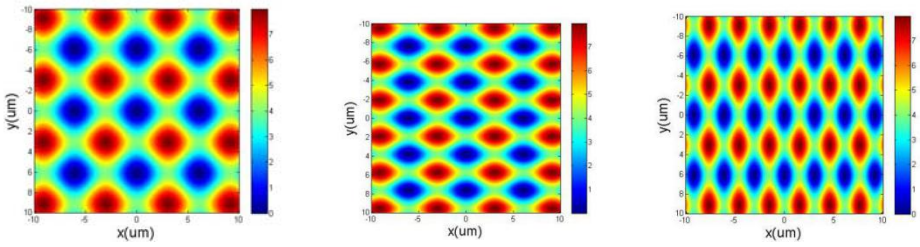

(A) (B) (C)

Fig. 4.3 Four-beam interference intensity distributed patterns with different incident angles of: (A) $\theta_1 = \theta_2 = \theta_3 = \theta_4 = 5.6^\circ$; (B) $\theta_1 = \theta_3 = 5.6^\circ$ and $\theta_2 = \theta_4 = 8^\circ$; (C) $\theta_1 = \theta_3 = 10^\circ$ and $\theta_2 = \theta_4 = 5.6^\circ$.

With the respect to the simulation results, it can be concluded that the optimal settings for fabricating convex structures with the cell diameter of 5.5 μm are:

- The TE-TE-TE-TE mode with polarisation angles: $\psi_1 = \psi_2 = \psi_3 = \psi_4 = 90^\circ$.
- The azimuthal angles of four-beam interference: $\varphi_1 = 0^\circ$, $\varphi_2 = 90^\circ$, $\varphi_3 = 180^\circ$ and $\varphi_4 = 270^\circ$.
- The incident angles of $\theta_1 = \theta_2 = \theta_3 = \theta_4 = 5.6^\circ$.

Under the settings, convex intensity distribution patterns with the cell diameter of 5.5 μm were simulated, as shown in Fig. 4.4.

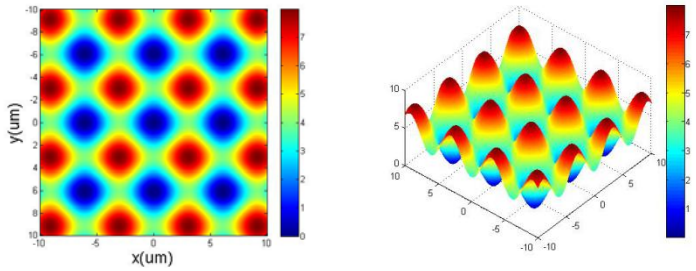

(A) (B)

Fig. 4.4 (A) 2D and (B) 3D plots of four-beam laser interference simulation results with the incident angle of 5.6° and the period of 5.5 μm.

The proper incident angles, azimuthal angles and polarisation angles were achieved to form micro dotted pattern with period of 5.5 μm by simulation which can be used for four-beam DLIL system set up.

4.2.2 Experiments

In experiments, a four-beam laser interference system using the optimal setting parameters as found in the simulations was employed to fabricate the micro and nano structures on the top of the microstructures, called hierarchical micro and nano hydrophobic structures. Single crystal p-doped (100) and polished silicon wafers with the electrical resistivity of 10 Ωcm were used. Single crystal silicon, as a semiconductor material, was chosen to fabricate superhydrophobic surfaces due to its applications in solar cells, micro-electromechanical systems (MEMS) and cell sensing devices in biomedicine [154, 155]. The laser source was a high-power pulsed Nd:YAG laser with the wavelength of 1064 nm, frequency of 10 Hz and pulse duration of 7 ns [31]. The couples of wave plates and polarisers were used before the substrate to adjust the energy and polarisation of each coherent beam. All the experiments were conducted in the air.

As shown in Fig. 4.5, the beam from the laser source was divided into four interference beams from four high-reflective mirrors (M) and three beam splitters (B) with the azimuthal angles of $\varphi_1 = 0^\circ$, $\varphi_2 = 90^\circ$, $\varphi_3 = 180^\circ$ and $\varphi_4 = 270^\circ$, and the incident angles of $\theta_1 = \theta_2 = \theta_3 = \theta_4 = 5.6^\circ$. The spatial located positions of the Ms

and the Bs were determined to achieve the azimuthal angles and incident angles, according to the simulation results. The four couples of wave plates (W) and polarisers (P) were used to adjust the polarisation angles of $\psi_1 = \psi_2 = \psi_3 = \psi_4 = 90^\circ$. Fig. 4.5 (C) show the four-beam DLIL setup. The laser power and energy meter (Coherent Lab Max-top) was used to measure the energy of coherent beams. The structured silicon was immersed in the hydrofluoric acid with a concentration of 5% for 180 s. The CA was measured with a contact angle system (JGW-360A).

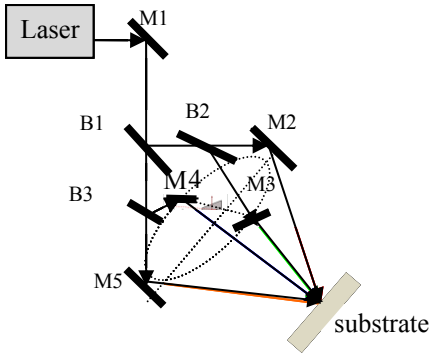

(A)

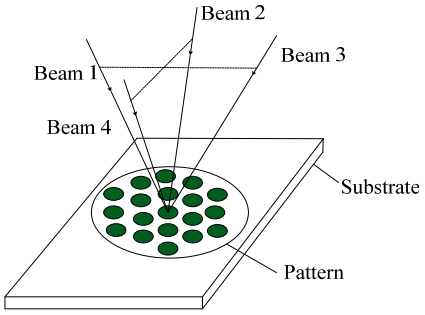

(B)

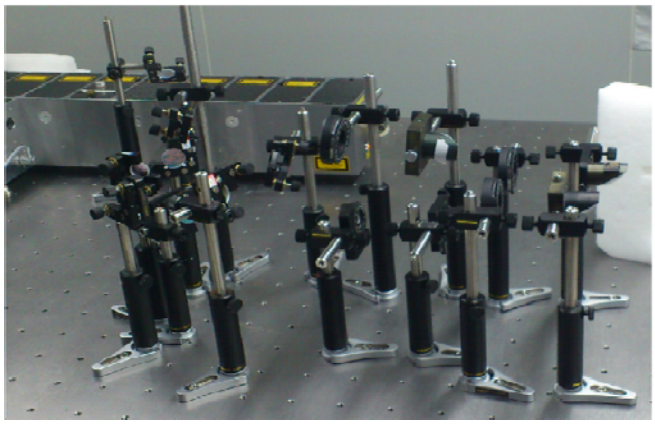

(C)

Fig. 4.5 (A) Schematic of a four-beam laser interference system; (B) 3D drawing of four-beam laser interference; (C) Four-beam DLIL setup.

In the experiments, the laser fluences of 0.64 J/cm^2, 0.71 J/cm^2 and 0.92 J/cm^2 and exposure durations of 20 s, 30 s, 60 s and 90 s were applied to form micro convex

structures which had different aspect ratios but the same average period of 5.5 μm on the silicon to obtain the CA values of corresponding surfaces for the superhydrophobic surfaces. In the case of four-beam DLIL fabrication on the silicon, the silicon vapour and plasma plump were produced with the threshold fluence of 0.64 J/cm^2, resulting in the largest bottom diameter of single convex structures [31]. Therefore, in the experiments, the range of laser fluences above the threshold fluence of 0.64 J/cm^2 was adjusted for the fabrication of convex structures on silicon surfaces with different aspect ratios. The micro convex structures obtained under the setting are as shown in Fig. 4.6.

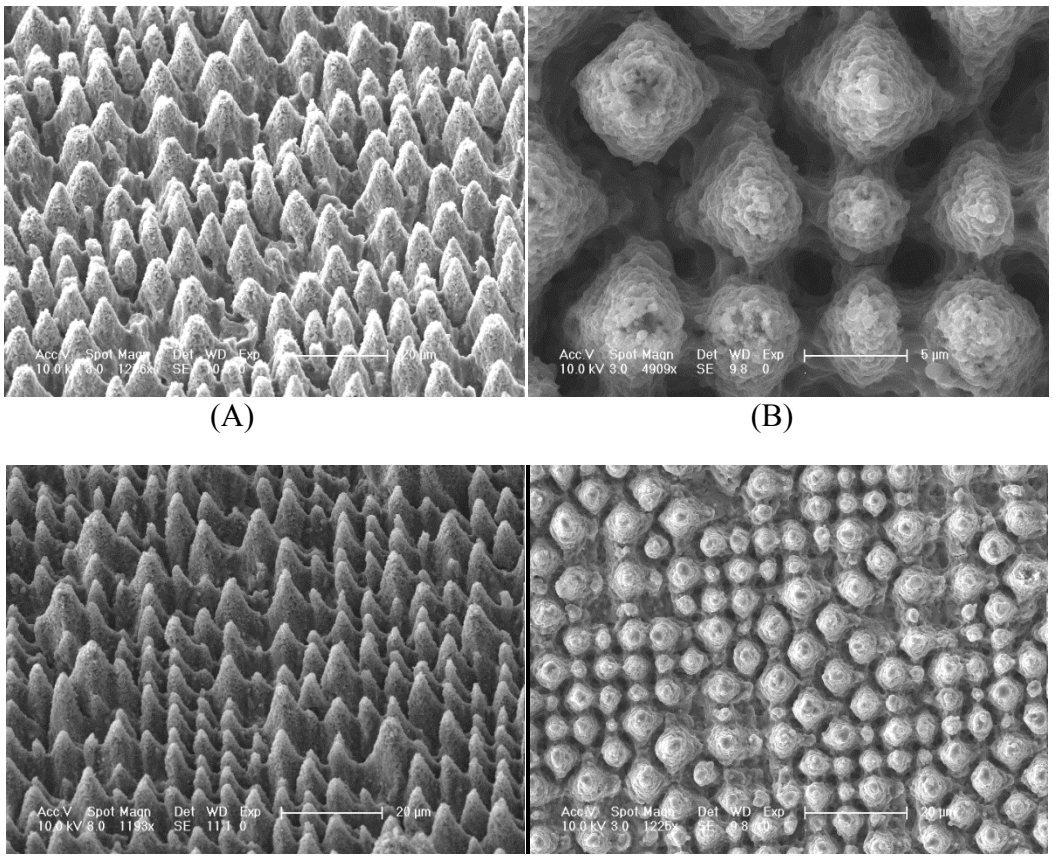

(A) (B)

(C) (D)

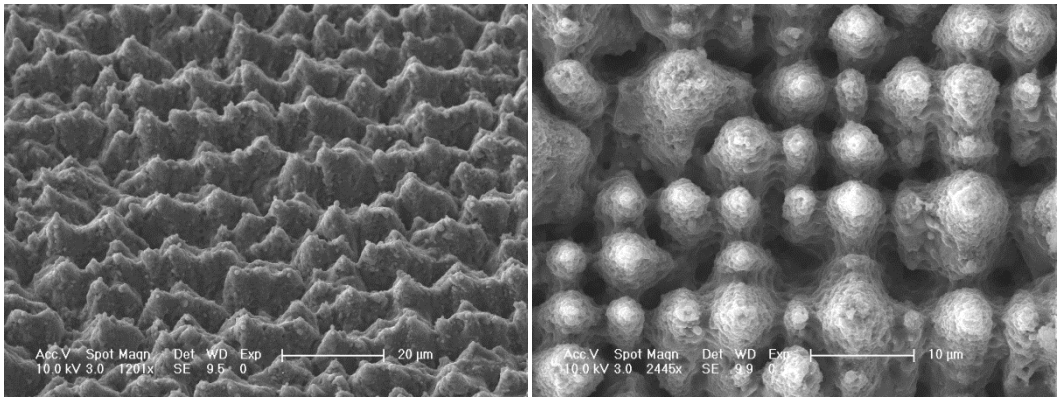

(E) (F)

Fig. 4.6 SEM images of convex micro and nano structures fabricated on silicon surface; (A) With laser fluence of 0.64 J/cm^2; (B) Vertical view of (A); (C) With laser fluence of 0.71 J/cm^2; (D) Vertical view of (C); (E) With laser fluence of 0.92 J/cm^2; (F) Vertical view of (E).

Due to the interactions of laser beams on the silicon, mainly thermal reactions, nano structures were also formed on the top of the micro convex structures. The nano structures were generated by the thermocapillary waves travelling along the phase boundary of the molten silicon. The wave-like nanostructures were formed on the top of the micro structures at the end of the ablation process [160].

As the silicon was oxidised during the etching process in the air, silica (SiO_2) was formed on the surface of fabricated hierarchical structures. To remove the silica, the surface was processed with HF in the experiments. As seen in Eq. (4.3), when HF was applied to the surface of fabricated structures, chemical reaction took place between the SiO_2 and HF, generating SiF_4 which was in the form of gas and water.

The cleanout time of HF was studied on the treated surfaces combining with the CA measurement. As the most commonly used reagent for wiping out the SiO_2, the cleanout time durations of HF were one to a few min based on the previous

experiments. The CA of treated surfaces was increased with the removing of SiO_2. The optimal cleanout time of 180 s was obtained when the CA reached the maximum value.

4.3 Results and Discussions [153]

Simulation results are shown in Figs. 4.1-4.4 and also discussed in the previous section. It was discovered that the optimal settings for fabricating convex structures with the cell diameter of 5.5 μm were:

- The TE-TE-TE-TE mode with polarisation angles: $\psi_1 = \psi_2 = \psi_3 = \psi_4 = 90^\circ$.
- The azimuthal angles of four-beam interference: $\varphi_1 = 0^\circ$, $\varphi_2 = 90^\circ$, $\varphi_3 = 180^\circ$ and $\varphi_4 = 270^\circ$.
- The incident angles of $\theta_1 = \theta_2 = \theta_3 = \theta_4 = 5.6^\circ$.

The optimal settings were confirmed in the experiments carried out in this research. Fig. 4.7 shows the micro and nano structures on the SEM images of one experimental result. It can be seen that the distance between two convex structures is 5.5 μm, which indicates the convex cell diameter is 5.5 μm.

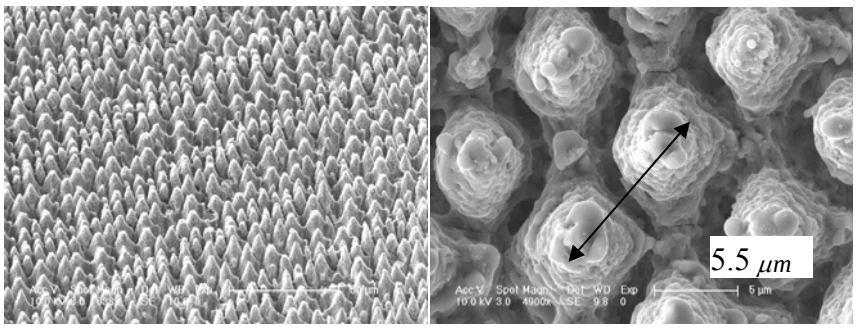

(A) (B)

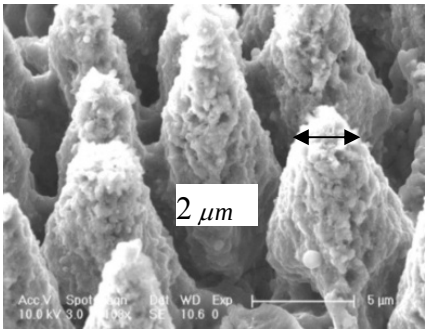

(C)

Fig. 4.7 (A) SEM image (low magnificent) of hierarchical structures fabricated on silicon surface; (B) Top view image of convex structures with cell diameter of 5.5 μm; (C) Close-up image of top of the single convex structure with diameter of 2 μm.

The theoretical CA value can be calculated according to the Cassie-Baxter model. The number of convex structures of the image in Fig.4.7 (B) is 6 in the area of 20×16 μm^2. As shown in Fig. 4.7 (C), the top of the convex structure is sharp, with the diameter of 2 μm. The result value of f_{sl} is about 0.06, as shown in

$$f_{sl} = 6 \cdot \pi / 20 \times 16 \approx 0.06 \tag{4.4}$$

The water contact angle α_1 of the untreated Si surface is 84.46°. According to Eq. (3.6), the calculated water CA is about 159.1°, as shown in the following.

$$\cos\alpha = f_{sl} \cos\alpha_1 + f_{lv} \cos\alpha_2 = 0.06 \times \cos\alpha_1 - 0.94 \tag{4.5}$$

In this case, α_1 =84.4° and α is 159.1°. The experiments show strong influence of the laser fluence, exposure duration T_e and cleanout time T_c to CA. Since the threshold of silicon ablation determines the energy of a single pulse of laser, impacts of different fluences were investigated in the manner of increasing the laser fluence whilst

keeping T_e fixed as 60 s. The results are given in Table 4.1. When the laser fluence was 0.64 J/cm^2 and T_e=60 s, CA value was measured as 153.2^o, as depicted in Fig.4.8, which was in a good agreement with the theoretical calculation. With the fluence increased, CA decreased slightly. This phenomenon can be explained to the decrease of the structure height caused by the melt and destroy of structures when the energy density exceeds a certain level.

Table 4.1 Different fluences versus the CA values on the resulted substrates.

Samples	Laser fluences (J/cm^2)	Exposure durations (s)	CA (°)
1	0.64	60	153.2
2	0.71	60	150.4
3	0.92	60	144.4

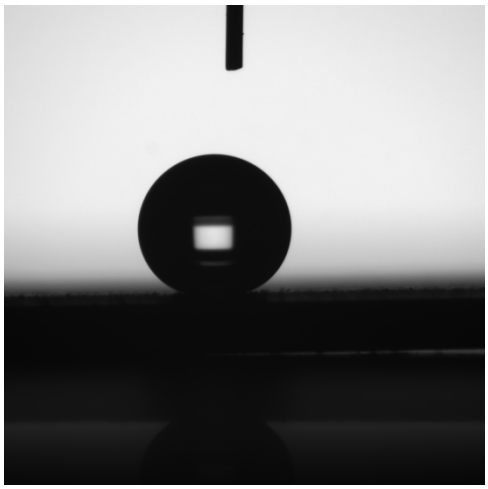

Fig. 4.8 Photography of a spherical water droplet on the treated silicon surface. The corresponding water CA is 153.2 ^{o}.

The samples with laser fluence of 0.64 J/cm^2 were chosen to analyse the effect on CA

with different exposure and cleanout time durations, as it leads to the CA value close to the theoretical calculation. It can be seen from Fig. 4.9, with the same T_c, CA value increases when T_e increases from 20 s to 90 s. The changes of CA value along with T_c when T_e is fixed roughly follow the same pattern, indicated in Fig. 4.9. The CA did not change much while the cleanout time increased (the ups and downs are within the measure offset.) It was because HF effectively cleaned out SiO_2 on the surface of silicon within a short period of time which was 60 s to 180 s, and, therefore, longer cleanout time did not contribute more to the chemical reaction. The optimal superhydrophobic surface where CA=153.2^o was achieved with T_e=60 s and T_c=180 s.

T_e also plays an important role in affecting the aspect ratio of the periodic patterns. The samples processed with different T_e of interference beams were characterized with SEM, as shown in Fig.4.10. The heights of the convex structures in Figs. 4.10 (A), (B) and (C) are 2 μm-3 μm, 5 μm-6 μm and 10 μm-14 μm, and the diameter of the base of convex structures is about 5 μm, with the results that the aspect ratios of them are 0.4-0.6, 1-1.2 and 2-3, respectively. The experimental results show that the increased aspect ratio caused CA increasing which can be explained by the reduction of the fraction of solid/liquid contact area due to the larger aspect ratios. Within a range of laser fluences, the aspect ratio was increased with the exposure duration. The highest aspect ratios of 2-3 were obtained with the exposure duration of 60 s and the laser fluence of 0.64 J/cm^2.

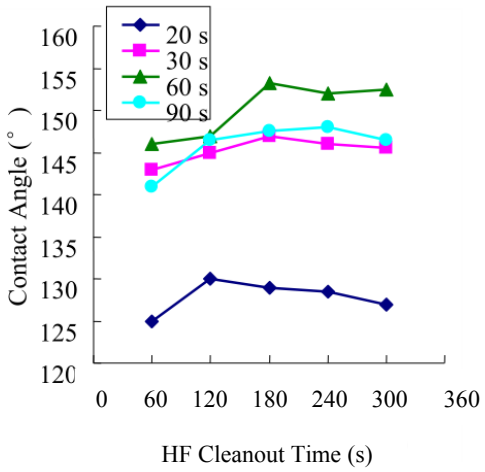

Fig. 4.9 Variations of CA values with different cleanout time durations of HF for the sample exposure durations of 20 s, 30 s, 60 s and 90 s, respectively.

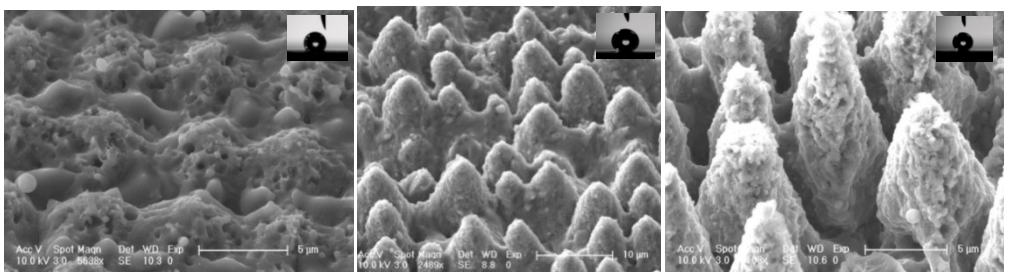

(A) (B) (C)

Fig. 4.10 SEM microstructures with different aspect ratios and contact angle measurement of the silicon samples: (A) Aspect ratio of 0.4-0.6 with T_e =20 s, CA=125.8°; (B) Aspect ratio of 1-1.2 with T_e=30 s, CA=145°; (C) Aspect ratio of 2-3 with T_e =60 s, CA=153.2°.

The high peak power of a nanosecond laser source provided a high temperature for the reaction of silicon and oxygen in the experiment process. According to the experimental results, the contact angle of the etched silicon surface was 5.6 °, and the contact angle of the untreated silicon surface was 84.46°, which was sharply decreased.

With the measurement of surface energy of the untreated silicon surface and the structured surface without HF cleaning, the latter was about two times higher than the former. SiO_2 that attached to the surface of silicon makes the material hydrophilic. The experimental result of the hydrophilic structured surface with a low contact angle was the evidence of SiO_2 generating on the surface during the process of etching. In order to wipe off it and the dust on the surface, the samples were immersed in HF with a concentration of 5％ for 180 s. Fig. 4.11 shows the surface structures treated by HF for different time durations. The roughness increased with the removing of SiO_2 by HF resulted in the reduction of the surface energy. Numerous nanoscale papillae were generated on the micro scale convex structures which formed the hierarchical superhydrophobic surface.

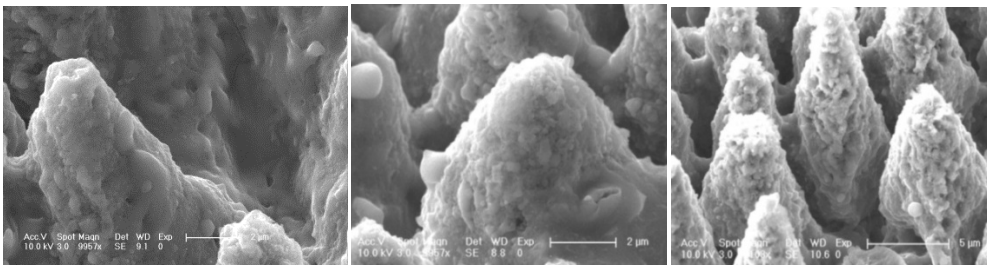

(A) (B) (C)

Fig. 4.11 SEM images of the topography fabricated by DLIL without and with HF processing: (A) Without HF processing; (B) With HF treatment for 60 s; (C) With HF treatment for 180 s.

The experimental results show the hierarchical structures with the period of 5.5 μm and aspect ratio of 2-3, which were designed and fabricated by four-beam DLIL with the optimal laser fluence of 0.64 J/cm^2 and exposure duration of 60 s. The HF treatment time was 180 s to achieve the relatively good result of the water CA of 153.2 ^{o}.

4.4 Summary

In this chapter, Matlab was used to simulate the four-beam laser interference intensity distributions in dotted patterns by adjusting the incident angles, azimuthal angles and polarisation angles for the design of convex structures with period of 5.5 μm. The proper incident angles, azimuthal angles and polarisation angles were used to set up the four-beam DLIL system to fabricate the periodic hierarchical micro and nano superhydrophobic structures formed by numerous micro convex structures covered by nanostructures on the silicon surface. During the fabrication process, parameters including the laser fluence, exposure duration and cleanout times were adjusted to obtain the optimal value of the CA. The periodic convex hierarchical structures with the period of 5.5 μm and the aspect ratio of 2-3 were fabricated in this work. The values of the incident angle, azimuthal angle, polarisation angle, laser fluence and exposure duration were optimized for the design and formation of interference structures on silicon.

The method offers its innovation that the well-designed periodic hierarchical superhydrophobic micro and nano structures can be fabricated directly by controlling the process of four-beam laser interference lithography and the use of HF to wipe off the SiO_2. Compared with others, this is a highly controllable and efficient method with its significant feature for the macroscale fabrication of hierarchical superhydrophobic micro and nano structures.

CHAPTER 5

REALISATION OF WEAR RESISTANT SURFACES ON ARTIFICIAL HIP JOINT USING THREE-BEAM DLIL

Chapter 5 presents research in the realisation of wear resistant surfaces using DLIL with its emphases on Co-Cr-Mo alloy which is the commonly used implant material for the femoral head of artificial hip joint.

It is known in theory that an array of micro circular dimples on the surfaces of artificial bones can reduce the real contact area in order to improve the wear resistance of the surfaces [8, 111, 120, 121]. However, the effects of dimple shape, size and density on HV and friction of Co-Cr-Mo alloy has been yet to be determined. This research investigated the effects and also the realisation of dimple arrays with various shapes, sizes and densities on the surfaces of Co-Cr-Mo alloy using DLIL.

5.1 Principle

Three-beam DLIL was suitable to fabricate the micro circular dimpled structures compared with four-beam DLIL, because the three-beam DLIL system is relatively easier to avoid errors during setup process, which leads to the modulation of structures [29]. Three-beam DLIL is, therefore, used to fabricate micro dimpled structures with circular shapes, and different sizes and area densities. The process has two steps,

namely, micro dimpled structure pattern creation and micro dimpled structure fabrication. Pattern creation refers to the shape, size (in terms of radius) and area density. All depend on the parameters of DLIL such as azimuthal angles, polarisation directions and incident angles. In the fabrication process, re-deposition and re-crystallisation take place in the phase changes of melting, vaporisation and plasma plume evolution [161]. Surface ablation by nanosecond laser is applied to the local annealing to stimulate the transition of phase in a few nanoseconds within the laser influenced area. For the nanosecond high power laser, the laser beams provide the energy for the heat diffusion of irradiated area, leading to the formation of micro dimpled structures. The variations of dislocation and residual stress distributions, generation of various carbide kinds, shape and size modifications of hardening effects and austenitic grains are caused by laser heating [162]. It is known that the grain size is the diameter of individual grains of sediments which are strongly linked to the hardness of materials [163]. The relationship between hardness and grain size can be expressed by Hall-Petch's equation [164]

$$H = H_0 + K_H d^{-1/2} \tag{5.1}$$

where H is the hardness, and H_0 and K_H are the material constants, d is the average grain size. It can be seen from the equation that the higher hardness is corresponding to the smaller grain size. The laser fluence and exposure duration have the effect on the heat diffusion which can influence the hardened region and the grain size of structured materials. When the laser fluence approaches to the energy threshold of Co-Cr-Mo alloy, the phase change occurs and the grain size is reduced. With the increased laser fluence, the vapour breaks down and plasma plump forms and the laser

energy is absorbed by the plasma plump resulting in preventing the heat diffusion. For the given laser fluence, the exposure duration has the effect on the dimple radius.

The best contrast dimpled patterns can be achieved by symmetrical three-beam interference according to Eqs. (2.12 a) and (2.12 b). Therefore, for the given symmetrical azimuthal angles and identical amplitude, the effects of polarisation and incident angle on the interference intensity can be described by

$$I = A^2\Big\{3 + 2\left|\vec{p}_1 \cdot \vec{p}_2\right|\exp[kx(\sin\theta_1 + \sin\theta_2)] + 2\left|\vec{p}_1 \cdot \vec{p}_3\right|\exp[k(x\sin\theta_1 - y\sin\theta_3)] \\ + 2\left|\vec{p}_2 \cdot \vec{p}_3\right|\exp[k(x\sin\theta_2 + y\sin\theta_3)]\ \Big\} \tag{5.2}$$

In the TE-TE-TM mode of three-beam DLIL, polarisation vector $\vec{p}_n (n = 1,2,3)$ in Eq. (2.11 d) can be expressed as

$$\vec{p}_1 = \sin\varphi_1\ \vec{i} - \cos\theta_1\ \vec{j} \tag{5.3 a}$$

$$\vec{p}_2 = \sin\varphi_2\ \vec{i} - \cos\varphi_2\ \vec{j} \tag{5.3 b}$$

$$\vec{p}_3 = -\cos\theta_3\cos\varphi_3\ \vec{i} - \cos\theta_3\sin\varphi_3\ \vec{j} + \sin\theta_3\ \vec{k} \tag{5.3 c}$$

The intensity distribution in Eq. (2.11 a) of three-beam interference can be written as [159]

$$\begin{aligned} I_3 = I_0\{&3 + 2(\sin\kappa_1\sin\varphi_2 + \cos\varphi_1\cos\varphi_2)\cdot\cos[k(A-B)] \\ &+ 2(-\sin\varphi_1\cos\theta_3\cos\varphi_3 + \cos\varphi_1\cos\theta_3\sin\varphi_3)\cos[k(C-B)] \\ &+ 2(\sin\varphi_2\cos\theta_3\cos\varphi_3 + \cos\varphi_2\cos\theta_3\sin\varphi_3)\cos[k(B-A)]\} \end{aligned} \tag{5.4 a}$$

$$A = \sin\theta_2 \cos\varphi_2 x + \sin\theta_2 \sin\varphi_2 y + \cos\theta_2 z \qquad (5.4\ b)$$

$$B = \sin\theta_1 \cos\varphi_1 x + \sin\theta_1 \sin\varphi_1 y + \cos\theta_1 z \qquad (5.4\ c)$$

$$C = \sin\theta_3 \cos\varphi_3 x + \sin\theta_3 \sin\varphi_3 y + \cos\theta_3 z \qquad (5.4\ d)$$

Matlab has a powerful tool to visualise the influences. According to the aforementioned formulas, the shape and size of dimples can be determined from simulation results displayed.

5.2 Circular Dimpled Structures Fabrication [156, 174, 175]

5.2.1 Simulation to Identify the Optimal Settings of Three-beam DLIL Systems

The aim of simulations is to identify the best setting, namely, incident angles, polarisation and azimuthal angles of three-beam laser interference for generating micro circular dimpled patterns with the periods of 5 μm and 8 μm. Because of the limitation of optical table, the achievable periods of LIL systems are in the range of 5 μm to 8 μm). Matlab software was used to conduct the simulations.

Three-beam laser interference was used to form the micro circular dimpled patterns because of its stability compared with four-beam DLIL, which leads to the less strict accuracy requirement for the system setting according to the error analysis of multi-beam DLIL implementation [29]. When three coherent laser beams are superposed together, the light intensity in the interference field is redistributed according to Eqs. (2.11) and (2.12), as described in Section 2.1.2. Fig. 5.1 shows the simulation results of the intensity distribution with different polarisation angles. As

shown in the diagram, intensity scale 1 to 7 is represented with colours from blue to red. The red areas indicate the high intensity and the blue areas show the low intensity. The convex intensity distribution patterns were formed under the TE-TE-TE and TE-TM-TM modes as the material in other areas-shown in red in Figs. 5.1 (A) and (B) -was removed due to the high light intensity. Fig. 5.1 (C) displays the intensity distribution under the TE-TE-TM mode, with the resulting of the dimple structures obtained. This indicates that the TE-TE-TM mode is suitable for forming dimple structures.

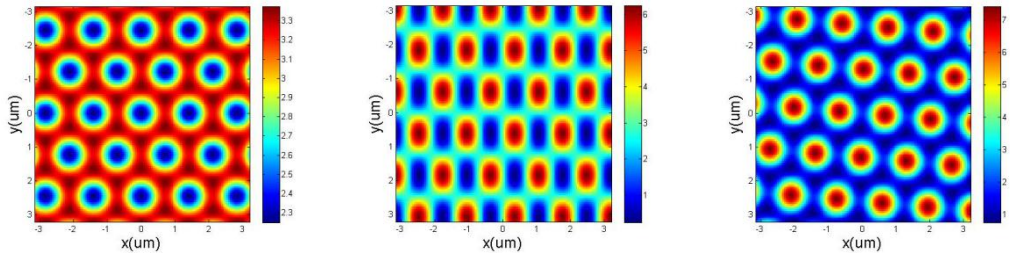

(A) (B) (C)

Fig. 5.1 Three-beam interference intensity distribution patterns under (A) TE-TE-TE mode; (B) TE-TM-TM mode; (C) TE-TE-TM mode.

In order to achieve the uniform dimple structures with the periods of 5 μm and 8 μm, the calculated incident angles of 8° and 5° by Eq. (2.13) were used. For the comparison, the incident angles of 10° was also used. The interference intensity distribution patterns under the TE-TE-TM mode with different incident angles and azimuthal angles were simulated to obtain the uniform circular dimple patterns. Fig. 5.2 shows the simulation results under the TE-TE-TM mode with different incident angles by adjusting the azimuthal angles of three coherent beams. The different incident angles were set with centrosymmetric and non-centrosymmetric coherent beams. Figs. 5.2 (A) and (B) show the intensity distributions with the polarisation angles of $\varphi_1 = 0^\circ$, $\varphi_2 = 100^\circ$ and $\varphi_3 = 240^\circ$ by setting the incident angles of

$\theta_1 = \theta_2 = \theta_3 = 5^\circ$, and $\theta_1 = \theta_2 = 5^\circ$ and $\theta_3 = 8^\circ$, respectively. Figs. 5.2 (C) and (D) are the intensity distribution results of centrosymmetric coherent beams with the azimuthal angles of $\varphi_1 = 0^\circ$, $\varphi_2 = 120^\circ$ and $\varphi_3 = 240^\circ$ by adjusting the incident angles of $\theta_1 = \theta_2 = 5^\circ$ and $\theta_3 = 8^\circ$, and $\theta_1 = 5^\circ$, $\theta_2 = 8^\circ$ and $\theta_3 = 10^\circ$, respectively. Figs. (E) and (F) show the intensity distributions with the azimuthal angles of $\varphi_1 = 0^\circ$, $\varphi_2 = 120^\circ$ and $\varphi_3 = 240^\circ$ by setting the incident angles of $\theta_1 = \theta_2 = \theta_3 = 5^\circ$ and $\theta_1 = \theta_2 = \theta_3 = 8^\circ$, respectively. As shown in Figs. 5.2 (A) and (B), the irregular patterns of intensity distribution with obvious modulations are formed, which are caused by the non-centrosymmetric coherent beams. For the centrosymmetric coherent beams of $\varphi_1 = 0^\circ$, $\varphi_2 = 120^\circ$ and $\varphi_3 = 240^\circ$, the different incident angles induce the triangle distributed elliptical dimpled intensity patterns as shown in Figs. (C) and (D). It can be seen from Figs. (E) and (F), the regular triangle distributed dimpled patterns without modulations are formed due to a perfectly symmetric configuration of interference beams

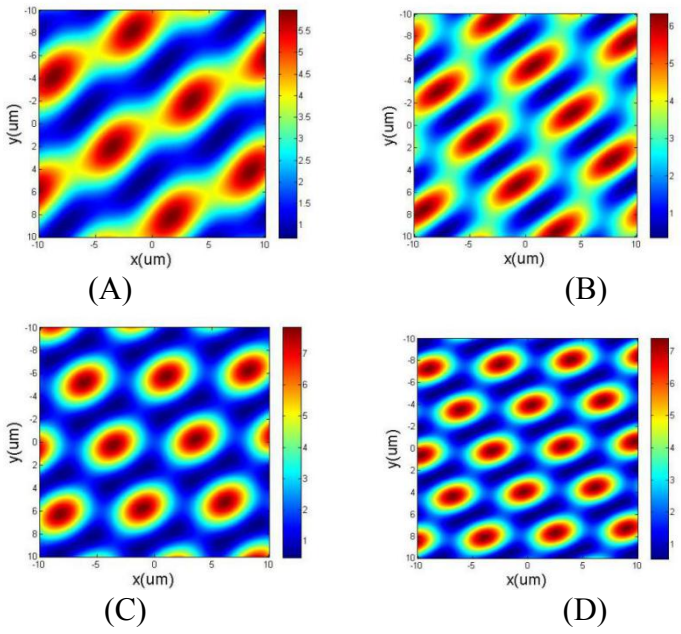

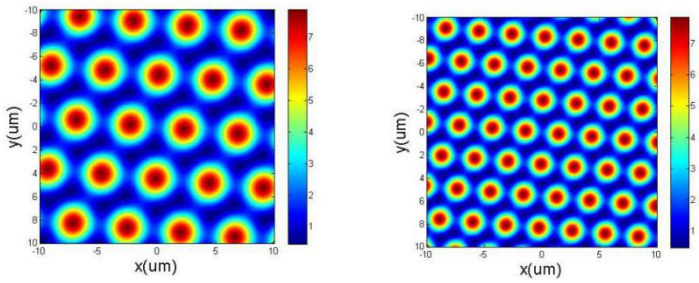

(E) (F)

Fig. 5.2 Three-beam interference simulation results with different incident angles and azimuthal angles in the TE-TE-TM mode.

Different dimple periods and sizes were formed to study the influence of laser fluence and exposure duration on the dimple area density, which can be defined as the ratio of dimple areas and the whole structured area. As shown in Figs. 5.2 (E) and (F), the dimple structures with the periods of 8 μm and 5 μm and the average diameters of dimples of 0.6 μm and 0.3 μm are achieved, respectively. The theoretical values of dimple densities can be calculated as 9.2% and 15.8%.

The simulation results show that the intensity distribution patterns with irregular, elliptical and circular dimple shapes can be obtained by adjusting the incident angles and azimuthal angles of coherent beams. For the three-beam DLIL under the TE-TE-TM mode, the centrosymmetric identical incident angles of each coherent beam can be used to generate the uniform circular dimple structures. The regular triangle distributed dimples of intensity patterns without intensity modulations were formed due to a perfectly symmetric configuration of interference beams. Uniform circular dimple structures with the periods of 8 μm and 5 μm and the dimple densities from 5%-15% were used for the experiments and the optimal settings for fabricating are shown as following:

- The TE-TE-TM mode with polarisation angles: $\psi_1 = \psi_2 = 90^o$ and $\psi_3 = 0^o$.
- The azimuthal angles of three beams interference: $\varphi_1 = 0^\circ, \varphi_2 = 120^\circ, \varphi_3 = 240^\circ$.
- The incident angles of 5° and 8°.

5.2.2 Experiments of Fabrication

The aims of the experiments are to fabricate circular dimpled structures on Co-Cr-Mo implant alloys with the optimal settings obtained from simulations for the purpose of confirming the wear resistant properties of high Vickers hardness and low friction of the structures.

Two sets of experiments were conducted in the fabrication of circular dimpled structures with the periods of 5 μm and 8 μm, respectively. Three-beam DLIL systems were set up using the optimal parameters obtained from the simulations as described above in both sets of experiments. In each set, laser interference experiments were carried out with different laser fluences and exposure durations to achieve the dimple densities from 5% to 15%. Vickers hardness and friction properties of the surfaces were then studied.

The detailed composition information of Co–Cr–Mo implant alloy sample is given in Table 5.1. The Co-Cr-Mo alloy is the commonly used material for the femoral head of artificial hip joint due to its high hardness and good corrosion resistance [141]. The Co–Cr–Mo implant alloy samples used in the experiments were cut from commercial artificial hip joint provided by Jinghang Biotech, China. The samples are of

cylindrical sections, about 2 mm in length and 15 mm in diameter. Before fabrication, they were firstly polished using a grinding machine with the diamond polishing paste, cleaned with a cetone and rinsed in ethanol and then deionized H_2O. When a mirror surface finish was achieved, the samples were patterned by laser interference lithography.

Table 5.1 Detailed composition information of Co-Cr-Mo implant alloy sample.

C%	Cr%	Mo%	Ni%	Fe%	Mn%	Si%	Co%
0.25	28.62	6.46	<0.10	0.12	0.81	0.70	Matrix

A high power nanosecond Nd:YAG laser (Innolas Spitlight 2000) was used in the DLIL system. The laser has the following specifications: 1064 nm wavelength, 10 Hz frequency, 7-9 ns pulse duration, and 2 J pulse energy. Fig. 5.3 illustrates the schematic and setup of a three-beam DLIL system. High-reflective mirrors (M) and beam splitters (B) were used to split the laser beam from the source into three. The polarisation angles are setting with $\phi_1 = 90^\circ$, $\phi_2 = 90^\circ$ and $\phi_3 = 0^\circ$. Laser fluences of 0.15 J/cm^2 and 0.26 J/cm^2 were yielded by placing polarisers together with wave plates at the front of the sample. The azimuthal angles of $\varphi_1 = 0^\circ, \varphi_2 = 120^\circ, \varphi_3 = 240^\circ$ and incident angles of $\theta_1 = \theta_2 = \theta_3 = 5^\circ$ were achieved by adjusting M1-M3 mirrors. Mirrors M4-M6 were used to guide the beam directions in the setup. The laser output energy was measured with a laser power and energy meter.

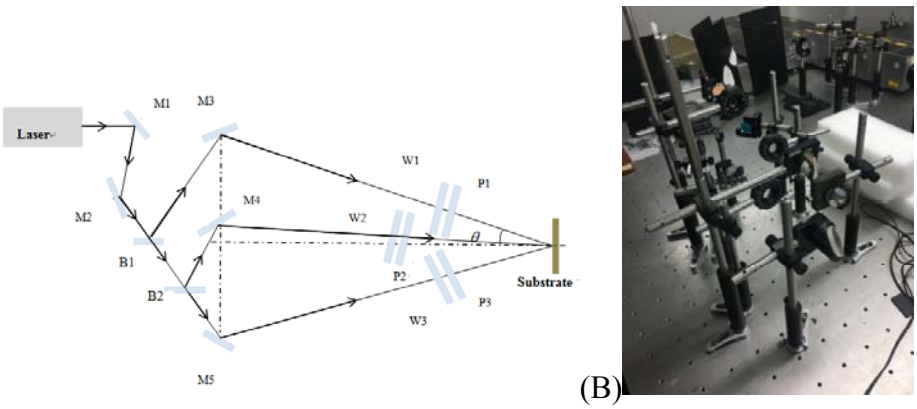

(A) (B)

Fig. 5.3 (A) Schematic of a three-beam DLIL system; (B) Three-beam DLIL setup.

The circular dimple structures with the different dimple densities from 5% to 15% in the periods of 5 μm and 8 μm were fabricated by adjusting the exposure duration and laser fluence. Three groups of samples were processed with three-beam DLIL. In the first group, ten samples with the laser fluences from 0 to 0.3 J/cm^2 and the exposure duration from 20 s to 70 s, as given in Table 5.2, were fabricated to find boundary conditions in terms of the laser fluence and exposure duration that were sufficient for the dimple structures to form and yet not melt the material.

Table 5.2 Settings of samples fabrication of Group 1.

Period (μm)	Sample	Laser fluence (J/cm^2)	Exposure duration (s)
8	1	0.1	60
	2	0.15	60
	3	0.26	60
	4	0.3	60
	5	0.26	20

	6	0.26	30
	7	0.26	40
	8	0.26	50
	9	0.26	60
	10	0.26	70

According to the results of the fabrication of the first group samples, in the second group, four samples (11-14) with the dimple period of 8 μm by setting the laser fluence of 0.15 J/cm^2 and the exposure durations of 30 s, 40 s, 50 s and 60 s were fabricated to investigate the effects of exposure duration and laser fluence on the dimple size for the three-beam DLIL. In the third group, two samples (samples 15 and 16) with the dimple period of 5 μm with the exposure duration of 60 s and the laser fluences of 0.15 J/cm^2 and 0.26 J/cm^2. Details of the second and the third groups are in Table 5.3.

Table 5.3 Settings of samples fabrication of Groups 2 and 3.

Period (μm)	Sample	Laser fluence (J/cm^2)	Exposure duration (s)
8	11	0.15	30
	12	0.15	40
	13	0.15	50

	14	0.15	60
5	15	0.15	60
	16	0.26	60

For the formation of circular dimple structures, different laser fluences and exposure durations were set for the three-beam DLIL. The experimental results of samples 1-4 that show the influences of laser fluence are given in Fig. 5.4. Figs. 5.4 (A) to (D) are the structured surfaces with the laser fluences of 0.1 J/cm^2, 0.15 J/cm^2, 0.26 J/cm^2 and 0.3 J/cm^2 when the exposure duration is 60 s. It can be seen that the dimpled structures are formed when the laser fluence exceeds 0.15 J/cm^2 and the dimple size is increased until 0.26 J/cm^2. When the laser fluence reaches 0.3 J/cm^2, the dimpled structures are destroyed.

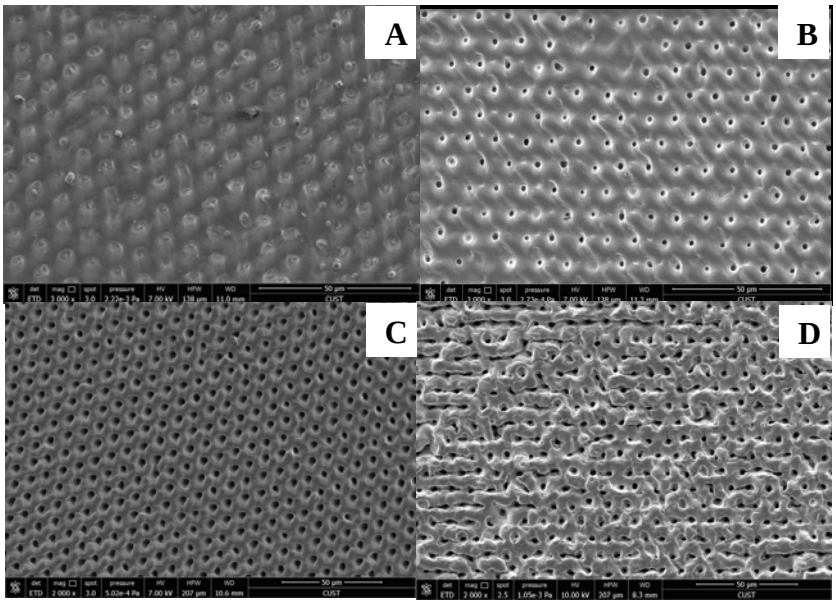

Fig. 5.4 SEM images of structured surfaces fabricated by three-beam DLIL.

Figs. 5.4 (B) and (C) are the SEM images of the dimpled structures formed with the laser fluencies of 0.15 J/cm^2 and 0.26 J/cm^2. As shown in the images, the dimple size increases with the increase of laser fluence. This phenomenon is in line with the heat diffusion as described in Section 2.1. When the laser fluence is 0.26 J/cm^2, approaching to the energy threshold of Co-Cr-Mo alloy, the heat diffusion induces the phase change and the maximum heat-affected zone (HAZ) area is formed.

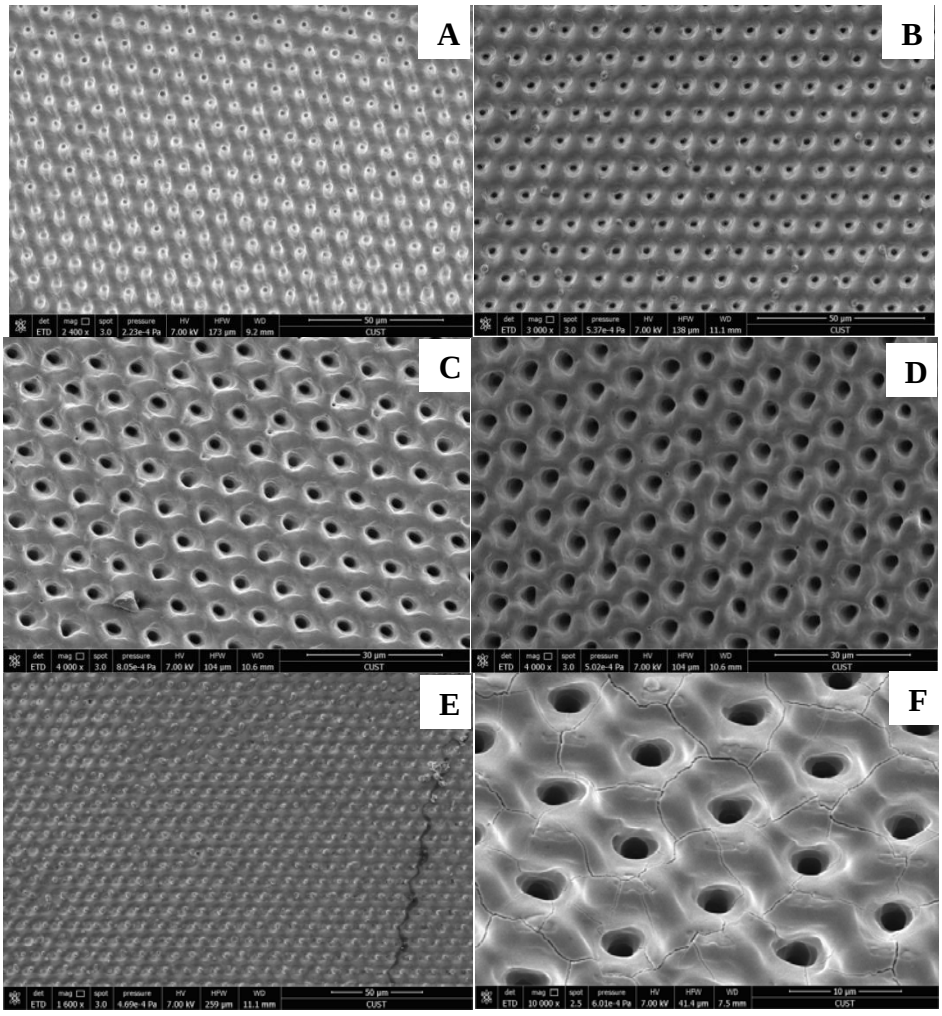

Fig. 5.5 SEM images of dimple structures fabricated by three-beam DLIL with laser fluence of 0.26 J/cm^2; (A) With exposure duration of 30 s; (B) With exposure duration of 40 s; (C) With exposure duration of 50 s; (D) With exposure duration of 60 s; (E) With exposure duration of 20 s; (F) With exposure duration of 70 s.

For samples 5-10, with fixing the laser fluence of 0.26 J/cm^2, the structured surfaces with the exposure durations from 20 s to 70 s are shown in Figs. 5.5 (A)-(F). Figs. 5.5 (A)-(D) show the dimpled structures with the exposure durations of 30 s, 40 s, 50 s and 60 s. The average diameters of circular dimples of (A) to (D) are 1.8 μm, 2.2 μm, 3 μm and 3.6 μm, respectively. The average diameters were calculated by ten random dimples of each dimpled structure. The corresponding values of dimple density of samples 6-9 were calculated as 3.7%, 5.5%, 10.3% and 14.8% which were the ratios of the dimple areas against the entire dimpled structure area. It indicated that the dimple diameter and density were increased along with the increasing exposure duration and the highest dimple density of 14.8% was obtained by setting the exposure duration of 60 s. The dimpled structures were not formed in Fig. 5.5 (E) and the crack was generated on the surface in Fig. 5.5 (F). Therefore, for the three-beam DLIL system, the laser fluences of 0.15 J/cm^2 and 0.26 J/cm^2 and the exposure durations of 30 s, 40 s, 50 s and 60 s were the optimal settings for the formation of dimpled structures.

With respect to the study of the influence and exposure duration, samples (11-16) with different dimple densities in the periods of 5 μm and 8 μm were fabricated, as shown in Fig. 5.6.

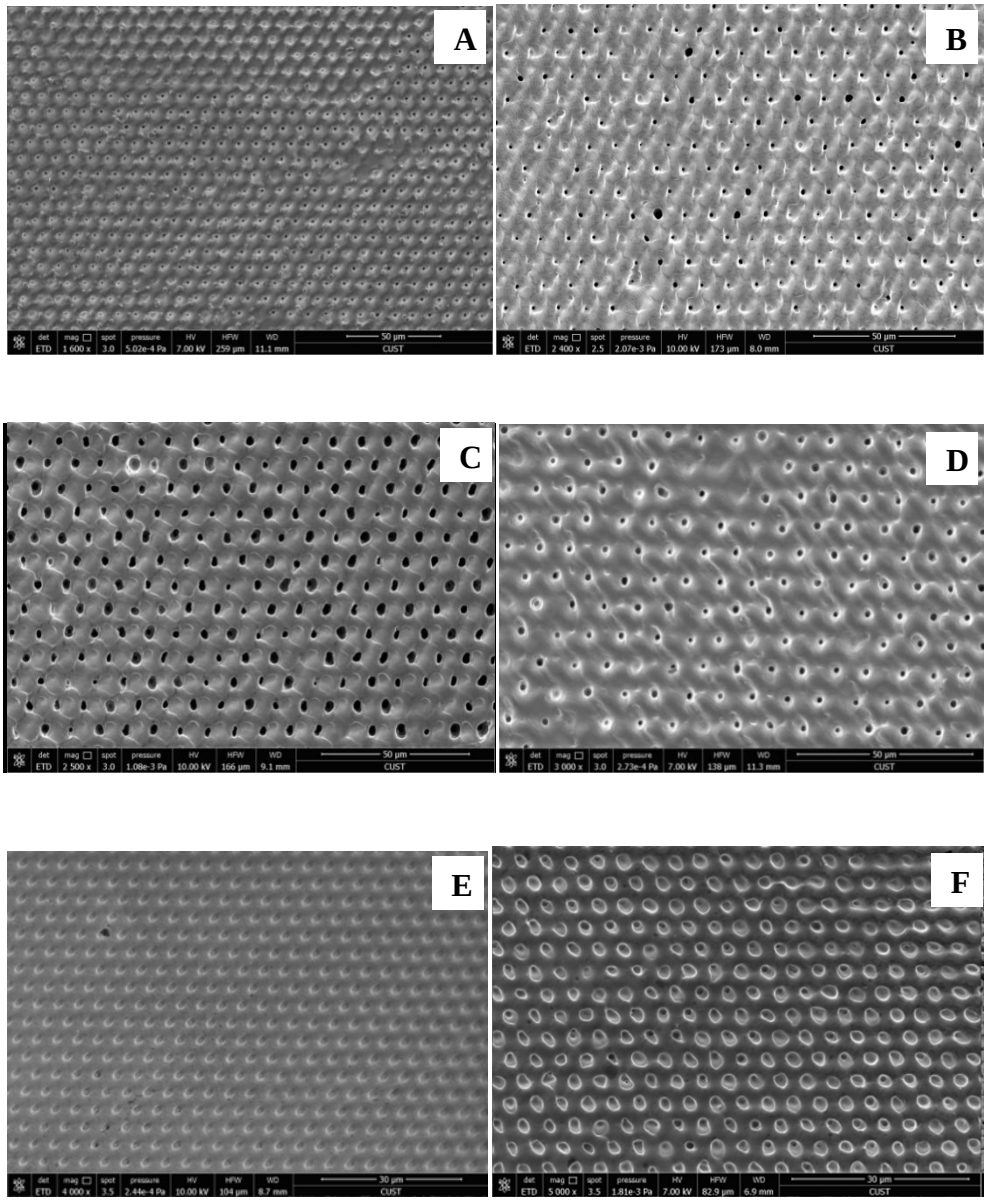

Fig. 5.6 SEM images of circular dimple structures fabricated on Co-Cr-Mo alloy surfaces: (A) With the incident angle of 5°, laser fluence of 0.15 J/cm^2 and exposure duration of 30 s; (B) With the incident angle of 5°, laser fluence 0.15 J/cm^2 and exposure duration of 40 s; (C) With the incident angle of 5°, laser fluence 0.15 J/cm^2 and exposure duration of 50 s; (D) With the incident angle of 5°, laser fluence 0.15 J/cm^2 and exposure duration of 60 s; (E) With the incident angle of 8°, laser fluence 0.15 J/cm^2 and exposure duration of 60 s; (F) With the incident angle of 8°, laser fluence 0.26 J/cm^2 and exposure duration of 60 s

5.3 Tribological Tests [156, 174, 175]

Tribological tests on the fabricated surfaces include the Vickers hardness tests and surface friction tests.

5.3.1 Hardness Tests

Micro hardness tests to measure HV values were carried out using micro hardness tester (MH-60). A diamond square-based pyramid indenter was used for the indentation with the applied load of 200 gf (kilograms-force) for 10 s at room temperature, which would avoid damaging the dimpled structures.

The tests include two steps to investigate the influences of density, laser fluence and exposure duration. In the first step, eight samples (6-9 and 11-14) with the period of 8 μm, fabricated with the laser fluences of 0.15 J/cm^2 and 0.26 J/cm^{2}and the exposure durations of 30 s, 40 s, 50 s and 60 s were used. The use of samples with the period of 8 μm was representative as the same optical components of three-beam DLIL system were used for the samples with the periods of 5 μm. This step aimed to identify the exposure duration resulting in the highest HV value. In the second step, samples 2, 3, 15 and 16 with the periods of 8 μm and 5 μm fabricated using the identified exposure durations with the laser fluences of 0.15 J/cm^2 and 0.26 J/cm^2 were used to identify the laser fluence that resulted in the highest HV value. The dimple densities of the four samples were significantly different based on the different periods which were used to study the influences of dimple density and period.

The results of Vickers hardness tests over one of the eight dimpled structured samples with the period of 8 μm are given in Fig. 5.7.

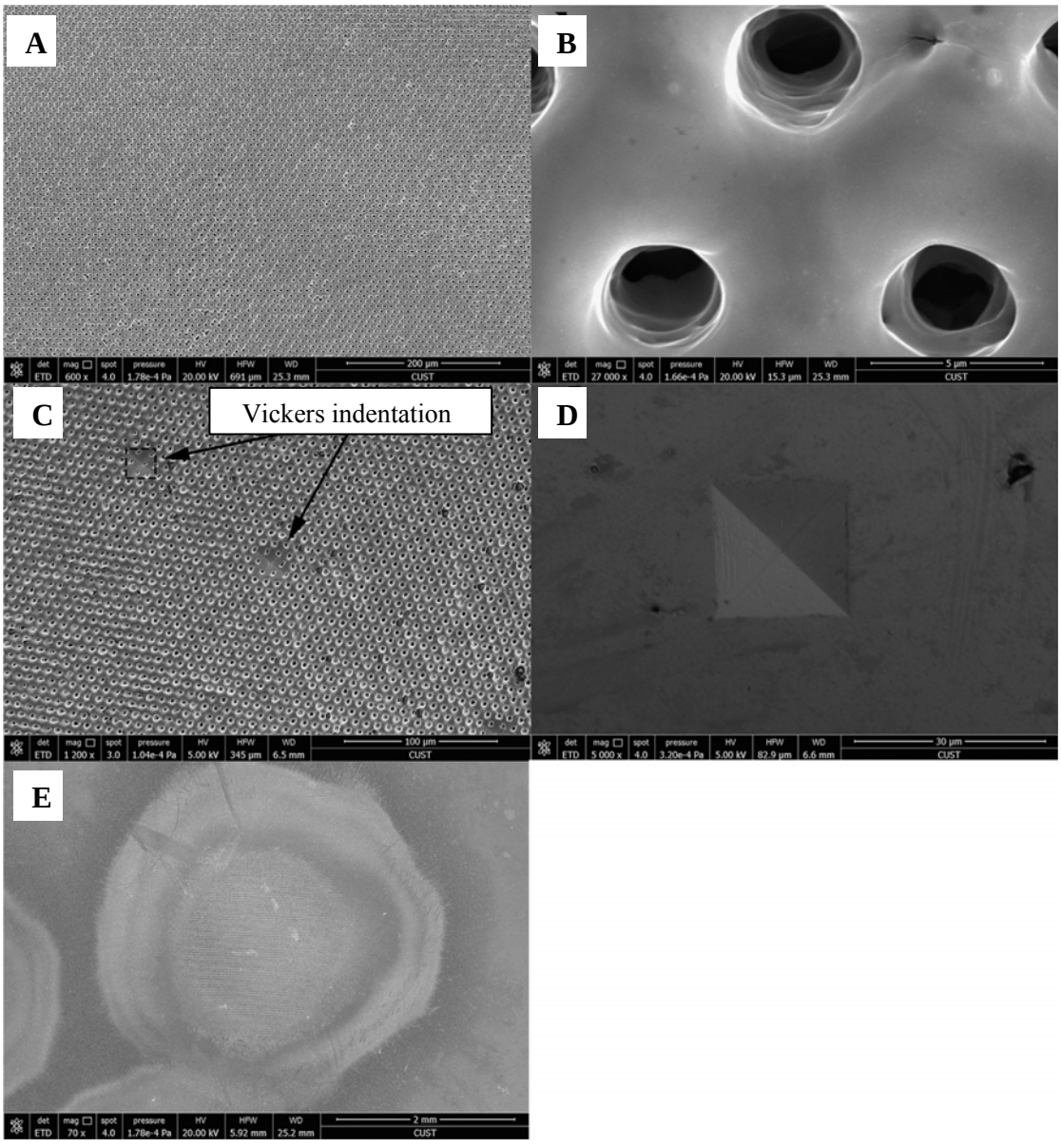

Fig. 5.7 (A) SEM image of the micro structure fabricated by three-beam DLIL; (B) Close-up image of the structured surface; (C) SEM image of Vickers indentation with the applied load of 200 gf for 10 s; (D) SEM image of original material with Vickers indentation; (E) The whole indentation pattern spot.

Fig. 5.8 clearly shows that the dimpled structured surfaces have higher HV values compared with the untreated samples. Four untreated samples were tested for comparison. The black line in the diagram represents their HV values. The blue line shows the HV values of the dimpled structures with the laser fluence of 0.26 J/cm^2, and the red line is corresponding to 0.15 J/cm^2. It can be seen that the blue and red lines are right above the black line.

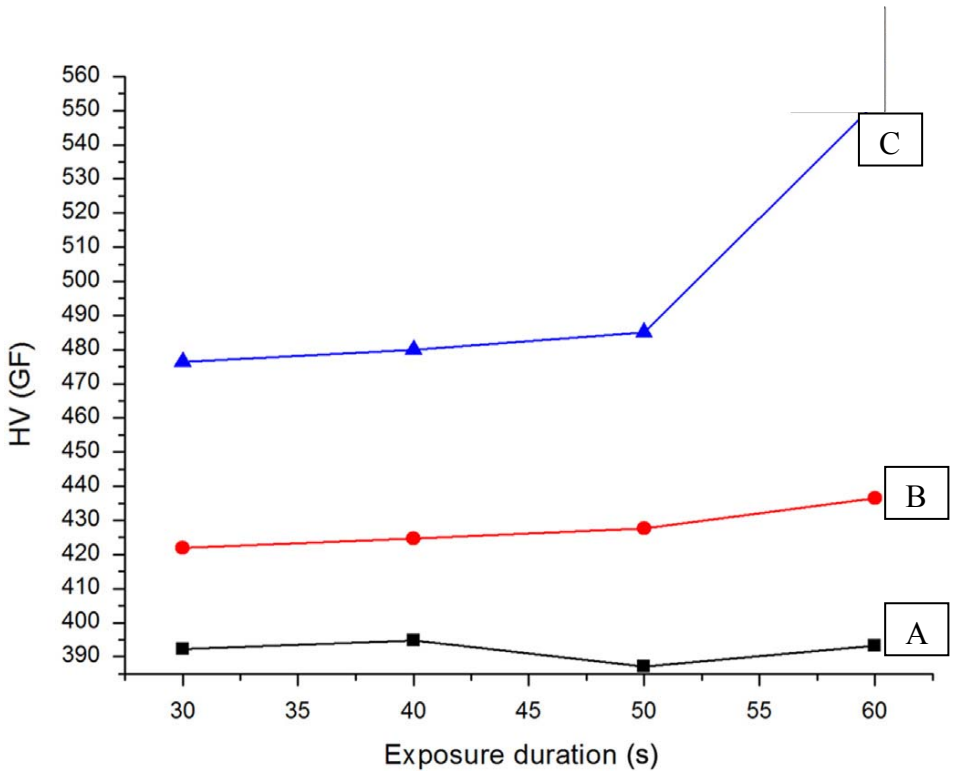

Fig. 5.8 The Vickers hardness curves of Co–Cr–Mo alloy surface: (A) Untreated sample; (B) Laser fluence of 0.15 J/cm^2; (C) Laser fluence of 0.26 J/cm^2.

As described in Section 5.1, the hardness can be increased by the heat diffusion of the laser which depends on both exposure duration and laser fluence. While Fig. 5.8 indicates the increase of hardness with the exposure duration, Table 5.4 clearly shows

the influence of laser fluence on the hardness. As given in the table, among the dimpled structures with different densities and laser fluences in the periods of 5 μm and 8 μm, the HV values of lower laser fluence (0.15 J/cm^2) are much smaller than that of higher laser fluence (0.26 J/cm^2).

Table 5.4 Vickers hardness testing results.

Laser fluence / Exposure duration / Dimple period (J/cm^2/s/μm)	Area density (%)	HV	Increase percentage (%)
Untreated		392.1	
0.15/ 60 / 5	7.7	425.7	8.57
0.15/ 60 / 8	7.7	436.3	11.27
0.26/ 60 / 5	12.1	520.6	32.77
0.26 / 60 / 8	14.8	558.7	42.49

The hardness of dimpled structured surfaces was increased to varying percentages with the increase of dimple period and laser fluence. The structures with the larger dimple period of 8 μm showed the more extend of hardness increases. The increased dimple period caused the increase of the contact stress at the edge of a circular dimple which induced the limit stress concentration effects resulting in the surface deformation and consequently caused the decrease of hardness value. When the laser fluence was 0.26 J/cm^2 and area density was 14.8%, the largest increase was up to 558.7 which was a 42.49% improvement. The heat diffusion will caused the increase of HAZ area and hardening region along with the sample distortion and alloy element vaporisation. Until the threshold of alloy, the larger the laser fluence is, the more the thermal diffusion process will extend in the Co-Cr-Mo alloy with reducing the grain

size and enlarging the hardening region. With respect to the previous experiment results, the optimal value of hardness was achieved with the proper laser fluence of 0.26 J/cm^2 and exposure duration of 60 s in the period of 8μm.

When the laser irradiated on the alloy, the HV value was increased due to the increased heat input. The phenomenon of phase transition was induced by laser heating. In addition, the alloy was heated to very high temperature in an ultra-short time (7-9 ns) which could refine the grain size and increased the number of crystal nuclei. It means that the plastic deformation due to the external force can be spread in more grain particles and reduce the concentration of stress with resulting in the increase of surface hardness. The experiment results of X-ray diffraction (XRD) are given in Fig. 5.9. The results indicate that the grain refinement formed and surface oxidation during the high temperature has enhanced the hardness, which are in accordance with the previously reported results [161].

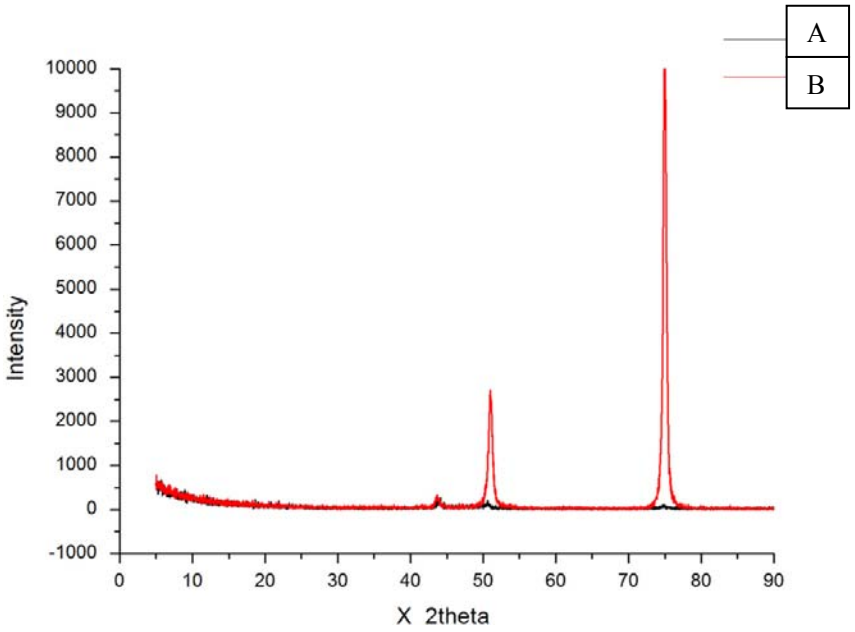

Fig. 5.9 The experimental results of XRD: (A) Untreated sample; (B) Circular dimpled structured surface fabricated by DLIL.

5.3.2 Surface Friction Tests

The surface friction tests were carried out after the hardness testing. In the tests, four samples (6-9) with the period of 8 μm, laser fluence of 0.26 J/cm^2 and exposure durations of 30 s, 40 s, 50 s and 60 s which have high Vickers hardness were used. The surface friction coefficients of the samples were measured. Though the hardness tests confirmed that samples with the period of 8 μm, laser fluence of 0.26 J/cm^{2}achieved the highest hardness, further examination was still needed for the samples with different exposure durations as the durations could have their effect on friction. The friction tests were performed by the RTEC micro friction and wear-test system, as shown in Fig. 5.10, under the dry friction condition. The testing conditions are shown in Table 5.5. In the testing process, the sliding tests were carried out with the 440 C stainless steel-ball, which had the highest hardness value, with the diameter of 40 mm to measure the reciprocating friction coefficient. The use of this smallest probe available of the RTE system was to ensure the accuracy of the tests as the surface structure in the nano scale.

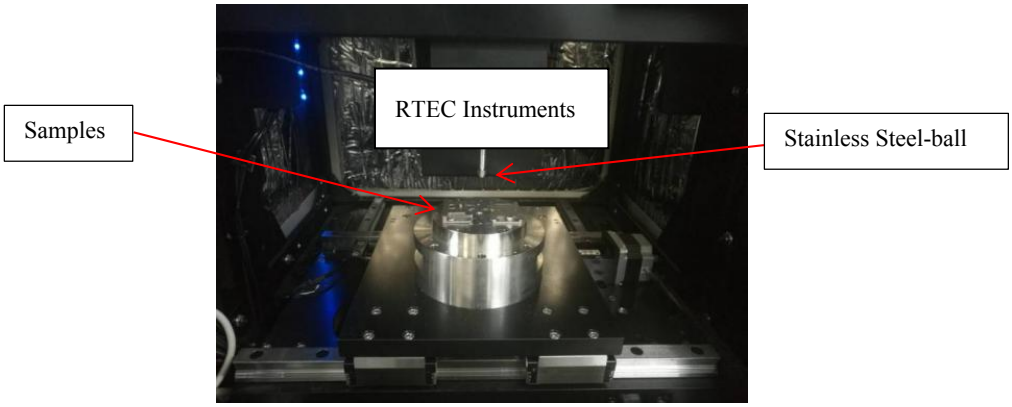

Fig. 5.10 RTEC micro friction and wear-test system.

Untreated samples (four samples) were tested under the same condition for comparison.

Table 5.5 Friction test conditions.

Normal load (N)	Sliding speed (mm/s)	Single trip (mm)	Friction time (min)	Sampling frequency (Hz)	Temperature (°C)	Relative humidity (%)
3	0.5	3	5	5000	25	20

Based on the aforementioned experimental results, the dimpled structured surfaces with the laser fluence of 0.26 J/cm^2 and dimple period of 8 μm showed excellent performance of hardness. Therefore, they also were used to study the effect of the exposure durations on the friction. The friction coefficients were measured using a RTEC micro friction and wear-tester under dry friction conditions. The test conditions with different exposure durations are shown in Table 5.6. Fig. 5.11 shows the curves of Co-Cr-Mo alloy surface friction coefficients as the experimental results.

Table 5.6 Test conditions with different exposure durations.

Sample	Exposure durations (s)	Fluences（J/cm^2）	Temperature (°C)	Conditions
1	0	0	25	clean-room
2	30	0.26		
3	40	0.26		
4	50	0.26		
5	60	0.26		

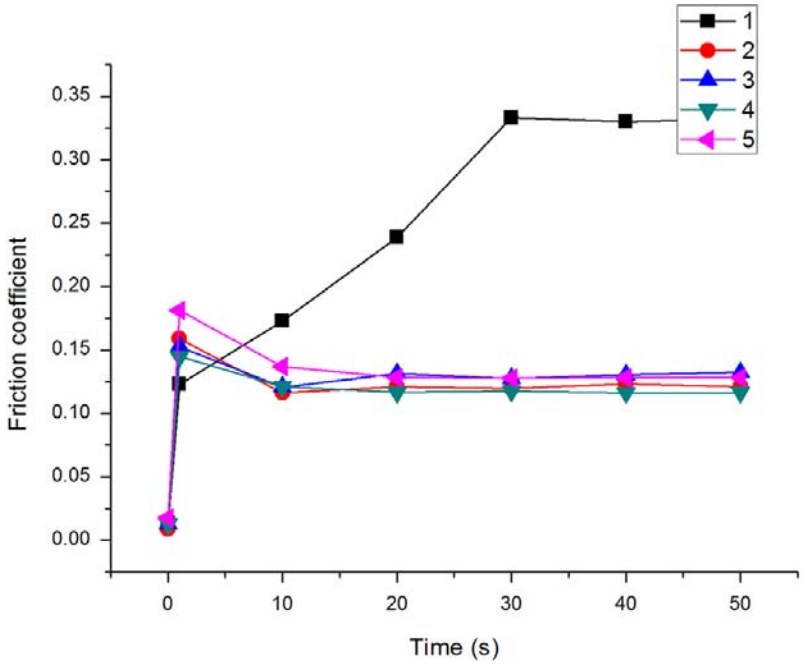

Fig. 5.11 Co-Cr-Mo alloy surface friction coefficients with the sample test time.

The friction coefficients of the untreated samples had a steep slope for the first 30 s. With the accumulation of time, the friction coefficient of untreated sample was increased obviously. However, the sample surface modified with laser interference lithography had a slope for the first 5 s in their respective "run-in" stages and the friction coefficient decreased until 10 s. Then both of the friction coefficients were in their stable stages after 10 s and 30 s, respectively. It was found that the friction coefficients had slightly variation with the increasing exposure durations. The stable friction coefficients at this stage were observed and they were 0.33 and 0.12 for the untreated sample and the sample modified with laser interference lithography, respectively, indicating that they exhibited significant differences. The modified samples with patterned circular dimpled structures showed extremely low friction coefficients. The results indicated that the dimple served as a micro hydrodynamic bearing to create additional hydrodynamic pressure to reduce the friction coefficient.

In addition, every micro dimple provided a pocket for trapping the wear debris during the time accumulation to prevent abrasion wear on bearing surfaces. Fig. 5.12 showed the SEM images of dimpled structured surfaces before and after the friction testing.

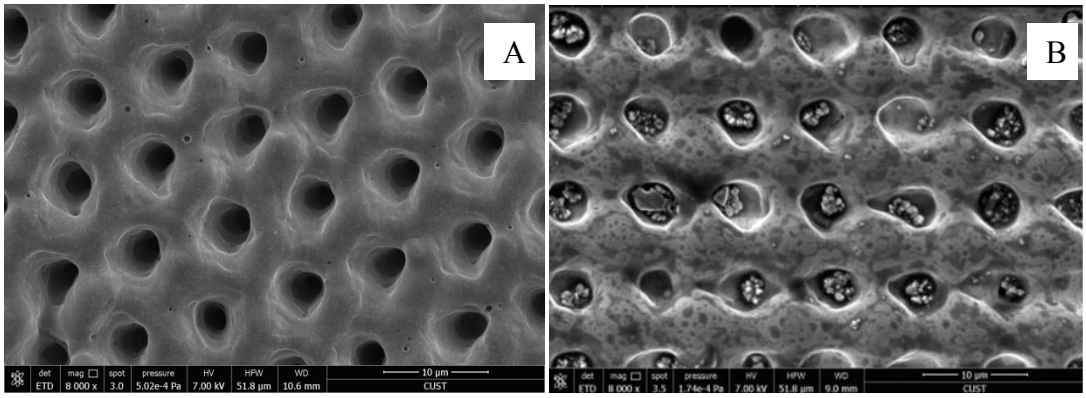

Fig. 5.12 SEM images of dimpled structured surface with the period of 8 μm: (A) Before friction coefficient testing and (B) After testing.

5.4 Summary

In this work, the optimal settings of incident angle, polarisation angle and azimuthal angle were achieved by three-beam interference simulation for setting up DLIL system to fabricate periodic micro circular dimpled structures on the Co-Cr-Mo alloy surfaces. The proper laser fluence and exposure duration for fabricating circular dimpled structures were obtained by three-beam DLIL systems. The optimal wear resistant property with the lowest friction coefficient and highest hardness were achieved on the micro structured surface with the dimple area density of 14.8% which was fabricated through the proper setting with the laser fluence of 0.26 J/cm^2 and exposure duration of 60 s. Experimental results indicate that the sample surface

modified with laser interference lithography presents higher hardness and lower friction properties than those untreated materials, including a 64% friction coefficient reduction and 42% hardness enhancement. This work provides a low cost and high efficient method for the design and fabrication of dimpled structures on the Co-Cr-Mo alloy with the improved hardness and reduced friction coefficient, which is very promising to significantly reduce the mean revision rate of post primary total hip replacements in the future.

CHAPTER 6

IMPROVING BIOCOMPATIBILITY OF TI-6AL-4V IMPLANT ALLOY BY DLIL

This chapter presents the study in the improvement of biocompatibility of Ti-6Al-4V alloy by employing structured surfaces formed using DLIL. Patterns of micro structured grooves, dimples and dots with different periods were designed by DLIL simulations through setting proper parameters including incident angles, azimuthal angles and polarisation angles. Such microstructures with roughness around 1 μm were fabricated by DLIL via adjusting the parameters including laser fluence and exposure duration. The impacts of the microstructures in grooves, dimples and dots with different periods and roughness on the proliferation, spreading and adhesion of Humanosteoblast-like osteosarcoma (MG63) cells were studied on Ti-6Al-4V alloy by multi-beam DLIL.

6.1 Two- and Three- Beam DLIL

The structured surfaces with different topography (grooves, dimples and dots) can be generated by two- and three- beam DLIL. The microstructures of grooves can be obtained by two-beam DLIL. Micro dimples and dots can be achieved by three-beam DLIL. Two-beam DLIL is suitable to fabricate micro grooved structures without modulation due to its simple optical systems. As discussed in Section 2.1.2, three-beam DLIL is suitable for forming dimpled and dotted structures. There are two steps in the process of fabricating the microstructures in grooves, dimples and dots, namely, pattern formation of micro grooves, dimples and dots and microstructures

fabrication in grooves, dimples and dots. Pattern formation refers to the topography and the period of grooves, dimples and dots, and it depends on the DLIL parameters, including azimuthal angle, polarisation angle and incident angle. During the fabrication process, parameters like laser fluence and exposure duration have the effect on the roughness of microstructures.

It is known that multi-beam interference patterns can be considered as superposition of multiple parallel stripes which are cosine distributed. The contrast of stripes can be calculated by Eqs. (2.12 a) and (2.12 b), which are applicable to both two-beam and three-beam LIL.

As studied in Chapter 5, micro dimpled intensity patterns and micro dotted intensity patterns can be generated under TE-TE-TM mode and TE-TE-TE mode, respectively. The azimuthal angles were symmetrically selected with $\varphi_1 = 0^\circ$, $\varphi_2 = 120^\circ$ and $\varphi_3 = 240^\circ$. According to Eqs. (2.1) and (2.11), under TE-TE-TE mode, with setting experimental conditions of $\theta_1 = \theta_2 = \theta_3 = \theta$ and $\psi_1 = \psi_2 = \psi_3 = 90^\circ$, the intensity distribution *I* can be expressed as

$$I_{TE-TE-TE} = A^2 \left[\begin{array}{l} 3 - \cos(k\sqrt{3}\sin\theta \cdot y) - \cos\left(\frac{\sqrt{3}}{2}\sin\theta \cdot y + \frac{3}{2}\sin\theta \cdot x\right) \\ -\cos\left(\frac{\sqrt{3}}{2}\sin\theta \cdot y - \frac{3}{2}\sin\theta \cdot x\right) \end{array} \right] \tag{6.1}$$

In the TE -TE -TM mode under the experimental conditions of three-beam interference, $\theta_1 = \theta_2 = \theta_3 = \theta$, $\psi_1 = \psi_2 = 90^\circ$,and $\psi_3 = 0^\circ$, the intensity distribution *I* can be expressed as

$$I_{TE-TE-TM} = A^2 \left\{ \begin{array}{l} 3 - \sqrt{3}\cos\theta \cdot \cos\left(k\sqrt{3}\sin\theta \cdot y\right) \\ -\sqrt{3}\cos\theta \cdot \cos\left[k\left(\frac{\sqrt{3}}{2}\sin\theta \cdot y + \frac{3}{2}\sin\theta \cdot x \right)\right] \\ -\cos\left[k\left(\frac{\sqrt{3}}{2}\sin\theta \cdot y - \frac{3}{2}\sin\theta \cdot x \right)\right] \end{array} \right\} \tag{6.2}$$

According to Eqs. (6.1) and (6.2), the periods of micro dimples and the periods of micro dots can be calculated by Eq. (2.13), which shows that the periods are the function of incident angle and wavelength.

For the same period, Eq. (6.1) and Eq. (6.2) can be used to compare intensity of dotted and dimpled structures as follow.

$$I_{TE-TE-TE} - I_{TE-TE-TM} = A^2 \left\{ \begin{array}{l} (\sqrt{3}\cos\theta - 1)\cdot\cos\left(k\sqrt{3}\sin\theta \cdot y\right) + \\ -\sqrt{3}\cos\theta \cdot \cos\left[k\left(\frac{\sqrt{3}}{2}\sin\theta \cdot y + \frac{3}{2}\sin\theta \cdot x \right)\right] \\ -\cos\left(\frac{\sqrt{3}}{2}\sin\theta \cdot y + \frac{3}{2}\sin\theta \cdot x \right) \\ +\cos\left[\begin{array}{l} k\left(\frac{\sqrt{3}}{2}\sin\theta \cdot y - \frac{3}{2}\sin\theta \cdot x \right) \\ -\cos\left(\frac{\sqrt{3}}{2}\sin\theta \cdot y - \frac{3}{2}\sin\theta \cdot x \right) \end{array} \right] \end{array} \right\} \tag{6.3}$$

In this case, the incident angle of 4 ^{o} calculated with period of 10 μm was put into Eq. (6.3). The result obviously show that $I_{TE\text{-}TE\text{-}TE} > I_{TE\text{-}TE\text{-}TM}$.

6.2 Fabrication of Microstructures in Grooves, Dimples and Dots [173]

6.2.1 Simulations to Verify the Optimal Settings of Two- and Three- beam DLIL Systems.

For the given setting of azimuthal angles and polarisation angles in Section 2.1.1, the aim of simulation was to obtain the micro intensity patterns in grooves and dimples and dots with required periods according to the proper setting. The groove periods of 10 μm and 20 μm were required for MG63 cells. Fig. 6.1 show the simulation results of the intensity distributions with the calculated incident angles of 3 º and 1.5 º.

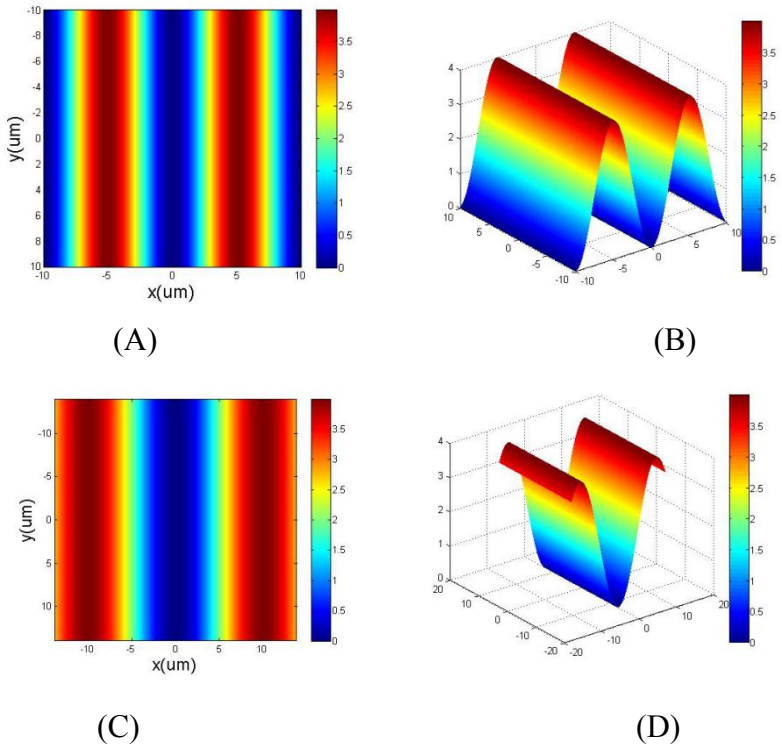

Fig. 6.1 Two-beam interference grooved patterns: (A) With the period of 10 μm in a 2D image and (B) 3D image; (C) With the period of 20 μm in a 2D image and (D) 3D image

As described in Section 2.1.2, the proper settings for micro dimpled patterns were

obtained with $\varphi_1 = 0^\circ$, $\varphi_2 = 120^\circ$ and $\varphi_3 = 240^\circ$ in the TE-TE-TM mode. The micro dotted patterns were achieved with $\varphi_1 = 0^\circ$, $\varphi_2 = 120^\circ$ and $\varphi_3 = 240^\circ$ in the TE-TE-TE mode. For the micro dimpled and dotted structures, the periods of 5 μm and 10 μm were required due to the sizes of MG63 osteoblast cells. Fig. 6.2 shows the simulation results of dimpled and dotted intensity patterns. The periods are calculated when the incident angles are 8° and 4° according to Eq. (2.13).

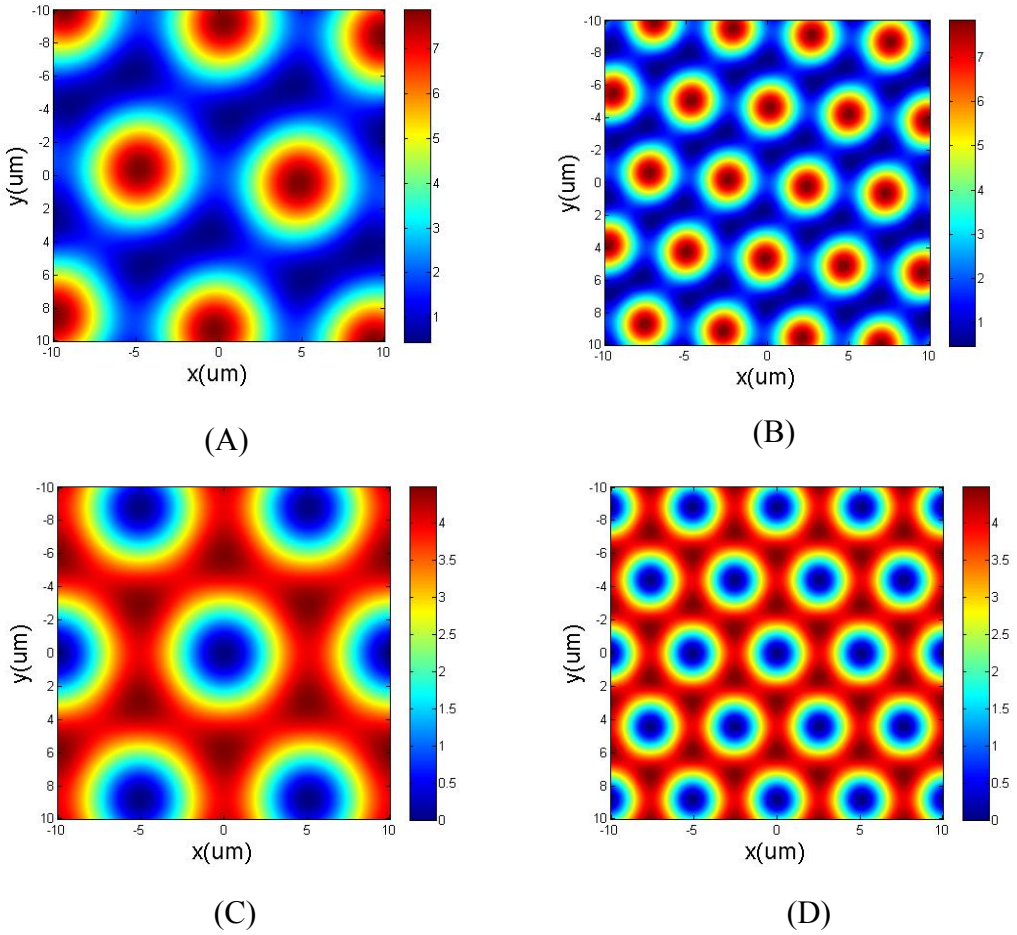

Fig. 6.2 Three-beam interference patterns: (A) Dimpled structure with the period of 10 μm; (B) Dimpled structure with the period of 5 μm; (C) Dotted structure with the period of 10 μm; (D) Dotted structure with the period of 5 μm.

The simulation results are according with the theoretical analysis in Sections 2.1.1 and

2.1.2 and the proper settings are confirmed as shown in Table 6.1.

Table 6.1 Two- and three- beam laser interference settings for micro patterns.

Topography	Polarisation angles (°)	Azimuthal angles (°)	Periods (μm)	Incident angles (°)
Grooves	$\psi_1 = \psi_2 = 90^\circ$	$\varphi_1 = 0^\circ$ and $\varphi_2 = 180^\circ$	10	$\theta = 3^\circ$
			20	$\theta = 1.5^\circ$
Dimples	$\psi_1 = \psi_2 = 90^\circ$, and $\psi_3 = 0^\circ$		5	$\theta = 8^\circ$
		$\varphi_1 = 0^\circ$, $\varphi_2 = 120^\circ$ and $\varphi_3 = 240^\circ$	10	$\theta = 4^\circ$
Dots	$\psi_1 = \psi_2 = \psi_3 = 90^\circ$		5	$\theta = 8^\circ$
			10	$\theta = 4^\circ$

6.2.2 Fabrication of Microstructures in Grooves, Dimples and Dots

The microstructures in grooves, dimples and dots on Ti-6Al-4V alloy were fabricated in three groups of experiments. In Group 1, samples were processed by three-beam DLIL, aiming to identify the boundary conditions of laser fluence and exposure duration for fabricating the expected dimpled and dotted structures. They are sufficient for the interference structures to form and yet not melt the Ti-6Al-4V alloy. In Group 2, fabrication was undertaken to form dimpled and dotted structured surfaces on the samples with the laser fluences and exposure durations determined in Group 1 experiments. In Groups 3, experiments were carried out in the same way as Group 2 but aiming to grooved structures and with two-beam DLIL. In all the experiments, the samples of medical grade Ti-6Al-4V alloy with the size of 10

mm×10 mm×1 mm, provided by Jinghang Biotech, China, were used. They were polished before the experiments, and then ground using emery papers. Finally, they were mechanically polished with nano-alumina polishing powders. Prior to the DLIL treatment, the samples were cleaned using ultrasonic machine (RT400). A confocal scanning microscope (Zeiss CSM700) with×20 magnification was used to examine the sample surfaces to ensure that no particles were left on the sample surface. The experiments were carried out using a pulsed Nd:YAG laser. The laser wavelength was 1064 nm, with the repetition rate of 10 Hz and the pulse duration of 7-9 ns. The laser spot size was 6 mm in diameter.

Dimpled and dotted structures fabrication using a three-beam DLIL system

Experiments that were conducted in the first group focused on the dimpled structures with the period of 10 μm, with the aim of identifying boundary conditions in terms of laser fluence and exposure duration. Eqs. (6.1) and (2.13) demonstrate that the large period of dimpled structures demands small incident angles. The incident angles required by the 10 μm period dimpled structure were 4^o, whilst those required by the 5 μm period dimpled structure were 8^o. As the incident angle is inverse proportional to the intensity of interference laser beam, the boundary conditions of dimpled structures with the period of 10 μm are more restricted than those with the dimpled structures with the period of 5 μm. Therefore, with the samples available, the study of boundary conditions concentrated on the dimpled structures with the period of 10 μm.

For the same period of 10 μm of dimpled (TE-TE-TM mode) and dotted (TE-TE-TE mode) structures, the incident angle was calculated as 4^o. The intensity of dotted structure is higher than that of dimpled structure as compared with Eq. (6.1) and Eq.

(6.2). Therefore, the boundary conditions of dimpled structures with period of 10 μm can be used for the formation of dotted structures with the same period.

The same goes to the grooved structure. First, that the large period of dimpled structures demand small incident angles holds true for grooved structures. Second, the incident angle for the grooved structures with the period of 10 μm is smaller than that for the dimpled structures with the same period. Eq. (2.9) gives the incident angle of 3^o for the grooved structures and Eq. (2.13) gives the incident angle of 4^o for the dimpled structures. This indicates that the intensity of two-beam interference for the grooved structures is higher than that of three-beam interference dimpled structures with the period of 10 μm. Therefore, the boundary conditions of dimpled structures with the period of 10 μm can be also used in the fabrication of grooved structures with the periods of 10 μm and 20 μm.

Three beam splitters (B) were employed to achieve three interference beams and three polarisers P1 to P3 were used for realising the TE-TE-TM mode with $\psi_1 = \psi_2 = 90^\circ$ and $\psi_3 = 0^\circ$. M3-M5 were located to guide the beams with the azimuthal angles of $\varphi_1 = 0^\circ$, $\varphi_2 = 120^\circ$ and $\varphi_3 = 240^\circ$, and the incident angles of $\theta_1 = \theta_2 = \theta_3 = 4^\circ$ for the fabrication of micro dimpled structures with the period of 10 μm. The energy of each coherent beam was measured with a laser power and energy meter. The schematic diagram of three-beam DLIL system is shown in Fig. 6.3 (A) and the DLIL setup is shown in Fig. 6.3 (B). Compared with Fig. 5.3, the incident angles of interference beams were different.

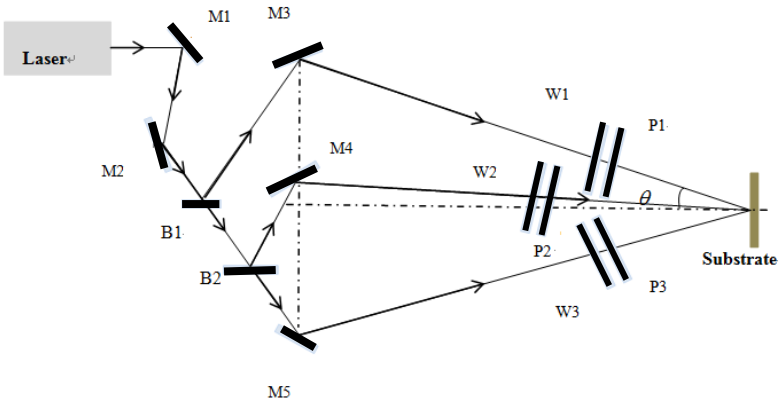

(A)

(B)

Fig. 6.3 (A) Schematic diagram of three-beam DLIL setup; (B) Three-beam DLIL setup.

Six samples (1-6) were processed with the three-beam DLIL with the laser fluence from 0.2 J/cm^2 to 0.36 J/cm^2 and exposure duration from 20 s to 70 s, as shown in Table 6.2.

Table 6.2 Laser parameters for fabrication of Group 1.

Sample	Laser fluence (J/cm^2)	Exposure duration (s)
1	0.200	70
2	0.245	60
3	0.280	40
4	0.315	30
5	0.350	20
6	0.360	20

The fabrication results are shown in Fig. 6.4. The dimples were not formed completely in (A), they were formed in (B) to (E), and they started to melt and be destroyed in (F).

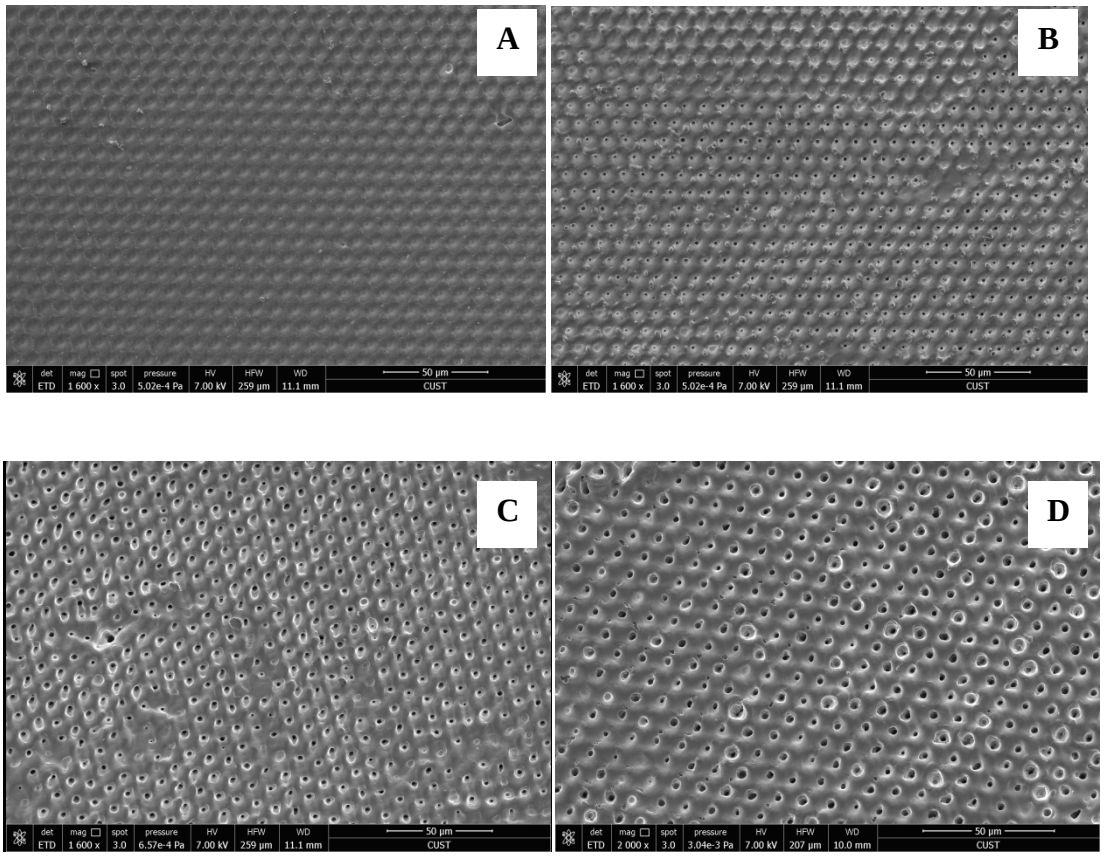

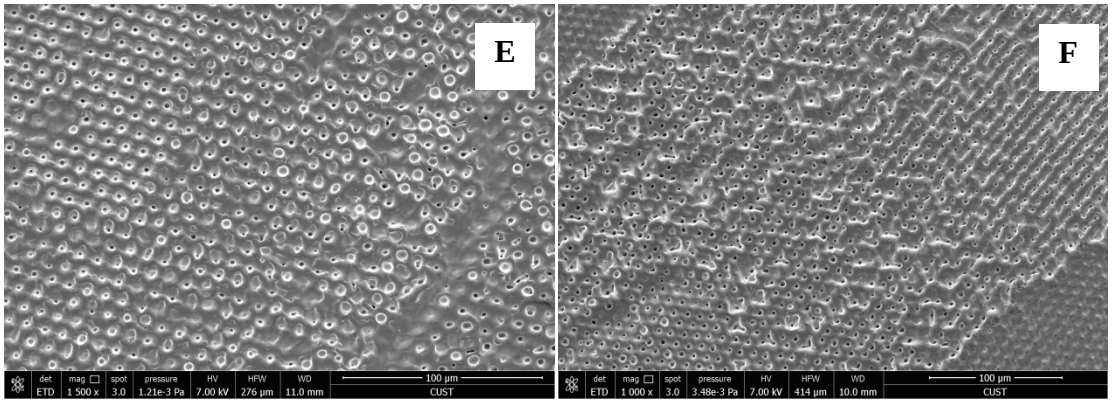

Fig. 6.4 SEM images of three-beam dimple structures: (A) With the laser fluence of 0.2 J/cm^2 and exposure duration of 70 s; (B) With the laser fluence of 0.245 J/cm^2 and exposure duration of 60 s; (C) With the laser fluence of 0.28 J/cm^2 and exposure duration of 40 s; (D) With the laser fluence of 0.315 J/cm^2 and exposure duration of 30 s; (E) With the laser fluence of 0.35 J/cm^2 and exposure duration of 20 s; (F) With the laser fluence of 0.36 J/cm^2 and exposure duration of 20 s.

Therefore, 0.245 J/cm^2 and 0.350 J/cm^2, and 20 s and 60 s were identified as the boundary conditions for the laser influences and exposure durations, respectively, for the fabrication of dimpled structures of periods 5 μm μm or 10 μm. With the same three-beam DLIL system, the boundary conditions are also suitable for the dotted structures with the periods of 5 μm or 10 μm, as explained earlier in this section.

The second group of experiments aims to fabricate dimpled and dotted microstructures on the surfaces of Ti-6Al-4V alloy. In this group, three samples (7-9) of micro dimpled and dotted structures with the period of 5 μm and seven samples (10-16) with the period of 10 μm were fabricated. The fabrication parameters of Group 2 experiments are given in Table 6.3.

Table 6.3 Three-beam DLIL fabrication parameters of samples of Group 2.

Period (μm)	Sample	Laser fluence (J/cm^2)	Exposure duration (s)	Polarisation mode
5	7	0.245	20	TE-TE-TE
	8	0.245	30	
	9	0.350	20	TE-TE-TM
10	10	0.245	30	TE-TE-TE
	11	0.245	50	
	12	0.315	30	
	13	0.280	40	TE-TE-TM
	14	0.315	40	
	15	0.315	50	
	16	0.350	20	

Fig. 6.5 shows the SEM images of samples 7, 9, 12 and 14. The samples were randomly selected with the same period and topography. The experimental results show a good agreement with the simulations.

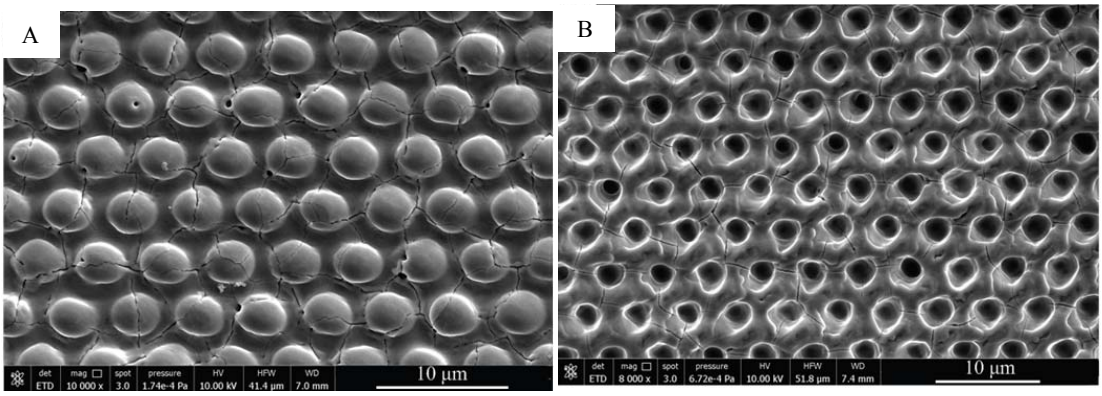

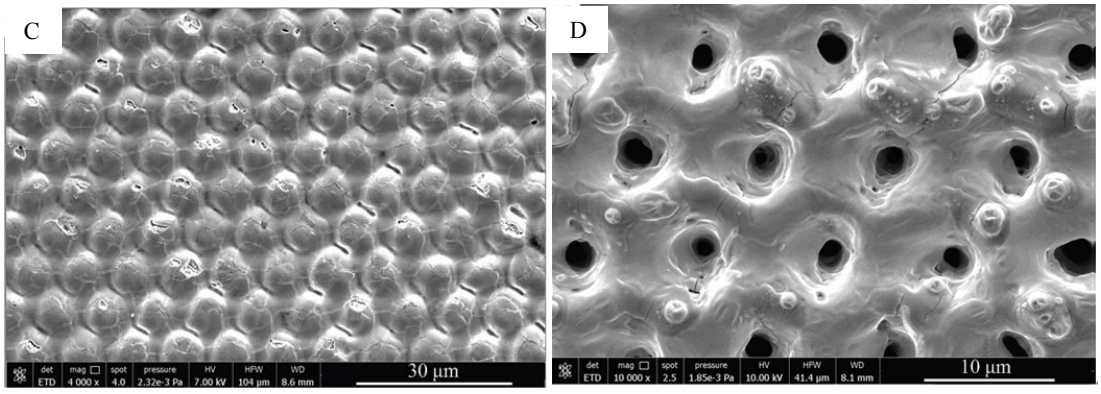

Fig. 6.5 SEM images of Ti-6Al-4V alloy surfaces: (A) Dotted structures with the period of 5 µm; (B) Dimpled structures with period of 5 µm; (C) Dotted structures with the period of 10 µm; and (D) Dimpled structures with the period of 10 µm

Grooved structure surface fabrication using a two-beam DLIL system

Group 3 experiments were designed to fabricate the micro grooved structures with the periods of 10 µm and 20 µm, respectively, using the laser fluences and exposure durations as identified as boundary conditions in the first group of experiments, shown in Table 6.4. Figure 6.6 illustrates the schematic diagram and setup of two-beam DLIL. The half-wave plates W1 and W2 were used to control the laser energy of each coherent beam and the polarisers P1 and P2 were placed between the wave plates and the sample to achieve the TE-TE mode with the polarisation angles of $\psi_1 = \psi_2 = 90^\circ$. Two high-reflective mirrors (M1-M2) and beam splitter (B1) were used to obtain the two interference beams and the locations and angles of M3-M4 were adjusted to guide the beams with the azimuthal angles of $\varphi_1 = 0^\circ$ and $\varphi_2 = 180^\circ$ and incident angles of $\theta = \theta_1 = \theta_2 = 3^\circ$ and $\theta = \theta_1 = \theta_2 = 1.5^\circ$ for the fabrication of micro grooved structures with the periods of 10 µm and 20 µm.

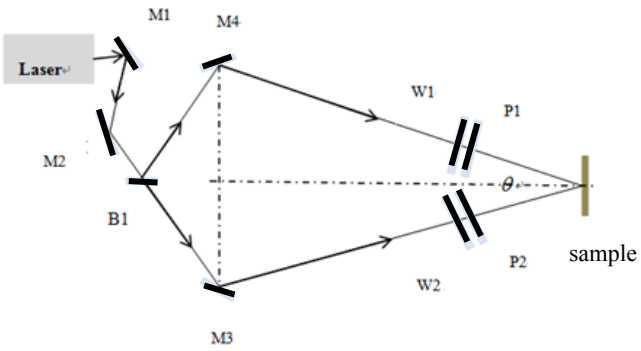

(A)

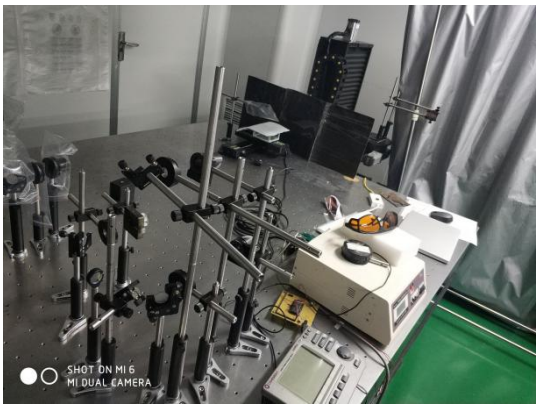

(B)

Fig. 6.6 (A) Schematic diagram of two-beam DLIL system; (B) Two-beam DLIL setup.

In the experiments, nine samples (17-25) with the micro grooved periods of 10 μm and 20 μm by setting the laser fluences of 0.245 J/cm^2 and 0.350 J/cm^2 and the exposure durations of 20 s, 30 s, 35 s, 40 s, 45 s, 50 s and 60 s were fabricated to study the effects of laser flunce and exposure duration on roughness for two-beam DLIL. The fabrication parameters of Group 3 are shown in Table 6.4.

Table 6.4 Two-beam DLIL fabrication parameters of samples of Group 3.

Period (μm)	Sample	Laser fluence (J/cm^2)	Exposure duration (s)
10	17	0.245	30
	18	0.245	40
	19	0.245	50
	20	0.245	35
	21	0.245	45
20	22	0.350	20
	23	0.350	30
	24	0.350	50
	25	0.350	60

Fig. 6.7 shows the SEM images of samples 18 and 23 which were randomly selected to represent the samples with the same period and shape, respectively. Grooved structures with the periods of 10 μm and 20 μm were obtained through adjusting the incident angles in the two-beam DLIL system which was in accordance with the simulation results.

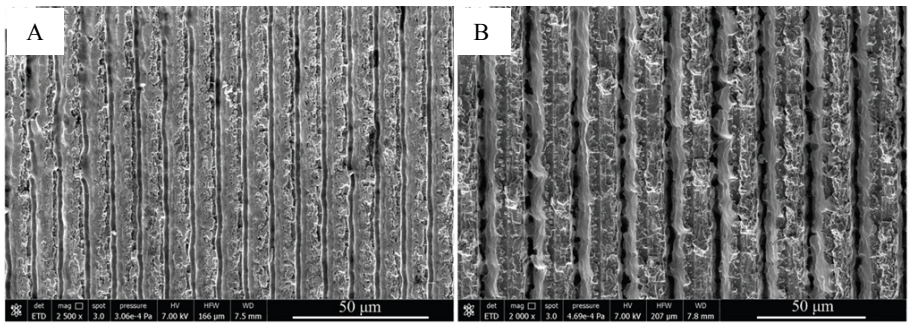

Fig. 6.7 SEM images of Ti-6Al-4V alloy surfaces: (A) Grooved structures with the period of 10 μm; (B) Grooved structures with the period of 20 μm.

6.3 Roughness and Wettability [173]

The roughness and wettability were measured for the biological experiments. Recent work demonstrated that the surface roughness R_a had the impact on the material biological compatibility as it affected the initial cell adhesion [165]. The surface wettability was able to regulate protein behaviours on structured surfaces and adjust the adhesion and function of cells at material interfaces [166].

6.3.1 Roughness

The roughness (R_a) of polished samples 7-25 was measured by a non-contact true colour confocal microscope (Zeiss CSM 700) as shown in Fig. 6.8. In the experiments, eight measurements were performed for each of the samples in an area of 93×117 μm^2. The roughness was characterized with the arithmetic mean surface roughness and calculated from the surface profiles. The value of R_a is the average of the eight measurements taken in eight randomly selected different regions on a sample. The R_a results of Group 2 including the samples with micro dimpled and dotted structures with periods of 5 μm and 10 μm are shown in Tables 6.5.

Table 6.5 Average roughness (R_a) for samples of Group 2.

Sample	7	8	9	10	11
R_a(μm)	0.872±0.133	0.918±0.346	0.987±0.246	0.715±0.171	1.479±0.245
Sample	12	13	14	15	16
R_a(μm)	1.21±0.527	1.30±0.745	1.37±0.759	1.354±0.586	0.656±0.045

In Table 6.5, samples 7-8 are micro dotted structures with the period of 5 μm and samples 10-12 are micro dotted structures with the period of 10 μm. The R_a values, calculated according to Eq. (6.8), indicate that the results are not only depended on the depth/height ratio but also the period of the microstructures. Considering the offset of roughness measurement with the above mentioned equipment is from 1 to 10 nm, the nanostructures formed on microstructures are not taken into account during the measurements.

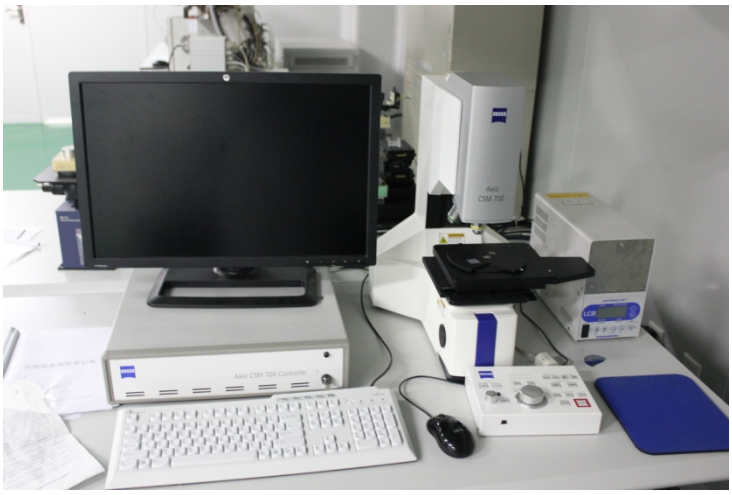

Fig. 6.8 Photograph of true colour confocal microscope.

Theoretical analysis of thermal transportation process during laser ablation has been investigated. It is demonstrated that the laser fluence and exposure duration have an

effect on the heat diffusion of irradiated area which contribute to the formation of vaporisation and plasma plump, leading to the creation of structured surfaces. Therefore, the depth/hight of microstructures and melting materials are depended on the laser fluence and exposure duration. When the laser fluence approaches to the energy threshold of Ti-6Al-4V alloy, the largest heat diffusion area occurs for the maximal depth of microstructures. With the increased fluence, the plasma plump forms and prevent the heat diffusion. For the given laser fluence, the exposure duration has the influence on accumulating the energy for the heat diffusion with resulting in affecting the depth of microstructures.

As discussed in Sections 4.3 and 5.3, the exposure duration and laser fluence have strong influences on the depth and height of the microstructures. According on Table 6.3, the laser fluences of samples 7 and 8 are the same as 0.245 J/cm^2 but the exposure durations are 20 s and 30 s, respectively. The increased exposure duration applied to sample 8 induced the increase of height of micro dotted structures of the sample, which was higher than that of sample 7, leading to the greater R_a value of samples than that of sample 7.

The effect of exposure duration can also be seen when comparing the roughness values of samples 10 and 11. With the same laser fluence of 0.245 J/cm^2 and the increased exposure duration of 50 s, sample 11 (dotted structure with the period of 10 μm) shows the larger R_a value of 1.479 μm compared with that of sample 10.

The effect of laser fluence on the height and depth can be seen when comparing the samples with the same period and exposure duration but different structures. Sample 9 is a micro dimpled structure with the period of 5 μm and sample 7 is a dotted structure

with the same period. The same exposure duration was applied to both samples as well. Its R_a value is greater than that of sample 7. This is because that the absolute value of the depth of this dimpled structure is greater than that of the height of dotted structure (sample 7), resultant from the increased laser fluence. For the same reason, sample 12 (micro dotted structure with the period of 10 μm) processed with the laser fluence of 0.315 J/cm^2 and the exposure duration of 30 s shows the smaller R_a value compared with that of sample 11.

Samples 8 and 10 were created with the same laser fluence of 0.245 J/cm^2 and the same exposure duration of 30 s, but with different periods of 5 μm and 10 μm, respectively. According to Eq. (6.1), the laser intensity corresponding to the dotted structures with the period of 5 μm is larger than that of the dotted structures with the period of 10 μm. The increased laser intensity induced the larger heat diffusion resulting in the increased height of micro dots. The R_a value of sample 10 is lower than that of sample 8 because of the decreased height of micro dots, resulting from the lower laser intensity corresponding to the larger period of sample 10.

Samples 13-16 are of micro dimpled structures with the period of 10 μm. Samples 13 and 14 were processed with the same exposure duration of 40 s and the laser fluences of 0.28 J/cm^2 and 0.315 J/cm^2, respectively. Sample 14 shows the larger R_a value because the increased laser fluence induced the larger depth of dimple. Sample 15 was processed with the same laser fluence of 0.315 J/cm^2 as the same as sample 14 but with a larger exposure duration of 50 s. As shown in Table 6.6, with the increased exposure duration, the R_a value of sample 15 was reduced slightly due to the melted micro dimples caused by the increased exposure duration. Sample 16 was processed with the laser fluence of 0.35 J/cm^2 and the exposure duration of 20 s and had the

smallest R_a value compared with other micro dimpled structures. It means that the depth of micro dimple is quite small due to the relative short exposure duration of 20 s. The roughness of grooved structures with periods of 10 μm and 20 μm (Group 2) and a polished but untreated sample are shown in Table 6.6.

Table 6.6 Testing results of R_a for Group 3 and polished sample.

Sample	17	18	19	20	21
R_a(μm)	0.868±0.298	0.946±0.232	0.891±0.236	0.908±0.177	1.473±0.289
Sample	22	23	24	25	Polished but untreated
R_a(μm)	0.944±0.234	1.541±0.321	1.635±0.382	1.292±0.273	0.019±0.004

In Table 6.6, samples 17-19 are micro grooved structures with the period of 10 μm. They were processed with the same laser fluence of 0.245 J/cm^2 and the exposure durations of 30 s, 40 s and 50 s, respectively. It can be seen in Table 6.6, sample 18 shows the highest R_a value and with the exposure duration increased to 50 s, and the R_a value of sample 19 is reduced due to the melted micro grooves. Samples 20-25 are micro grooved structures with the period of 20 μm. Samples 20 and 21 were processed with the same laser fluence of 0.245 J/cm^2 and the exposure durations of 35 s and 45 s. With the increasing of exposure duration, the depth of micro grooves was increased, resulting in the increased R_a value. Samples 22-25 were processed with the same laser fluence of 0.35 J/cm^2 and the exposure durations of 20 s, 30 s, 50 s and 60 s. Testing results of samples 22-24 show that the R_a value is increased with the increase of exposure duration. And the R_a value obviously is reduced with the exposure duration increased to 60 s. It is indicated that when the exposure duration exceeds 50 s, the micro grooves are melted and the depths decreased.

It can be seen from Tables 6.5 and 6.6, R_a of the micro grooves, dots and dimples structures are around to 1 μm (between 0.6 μm to 1.7 μm) which show that the roughness of the structured surfaces is significantly greater than that of the untreated surface. The results of R_a measurements and calculations show that the variation of height/depth of microstructures highly depends on the laser fluence and exposure duration employed in fabrication. When the laser fluence and exposure duration exceed a certain level, the micro structure is melted and the height and depth are reduced.

Tables 6.5 and 6.6 could be used as the references for the analysis of the experiments of cell proliferation and morphology.

6.3.2 Wettability

The influence of different micro structures (dots, dimples and grooves) on wettability can be indirectly measured via the contact angle of samples 7-25. Prior to the measurements, the samples were ultrasonically cleaned with the acetone solution, ethanol and deionized water. The duration of sonication for all samples was 10 min. The samples were then left to dry in the air at room temperature over night.

The CA values of the micro structures were measured usingthe water CA system, known as JGW-360A, with the same procedure as mentioned in Section 4.3. The average values of at least ten measurements were obtained from different locations.

The measurement process is illustrated in Fig. 6.9, 2.5 μl deionized water was dropped on the substrates using a microliter syringe. The CA was observed with a CCD camera through analysing the images of water droplets. The isosceles right protractor

with the sides of a and b was used to measure the CA in the following three steps. In the first step as shown in Fig. 6.9 (A), the protractor was moved down to make the sides a and b tangent to the edge of the droplet. A and B were the intersection points of right angle sides and solid surface line. In the next step, the protractor was moved lower down to make the triangular point and the highest point C of spherical profile coincided as shown in Fig. 6.9 (B). In the last step, make the protractor anticlockwise rotated around point C until side a went through the intersection of solid/liquid/vapour phases. The rotation angle of protractor was δ . The unit of the protractor rotation angle was 1^{o} and the measurement accuracy was 0.1^{o}.

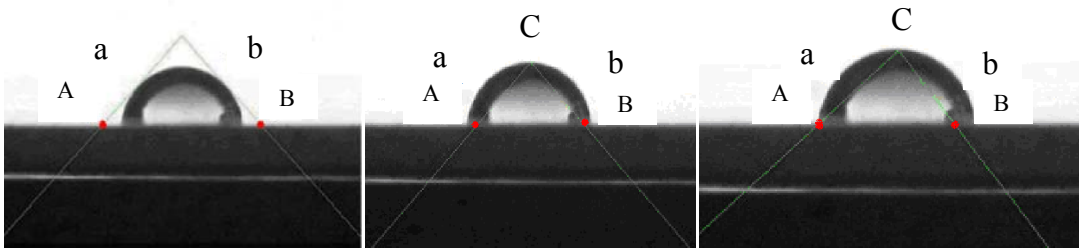

(A) (B) (C)

Fig. 6.9 Contact angle measurement.

During the measurement, the contour curve fitting method was applied to the digital image of a sessile droplet to obtain the contour of droplet which appeared as a part of perfect circle. The schematic diagram of CA measurement is shown in Fig. 6.10.

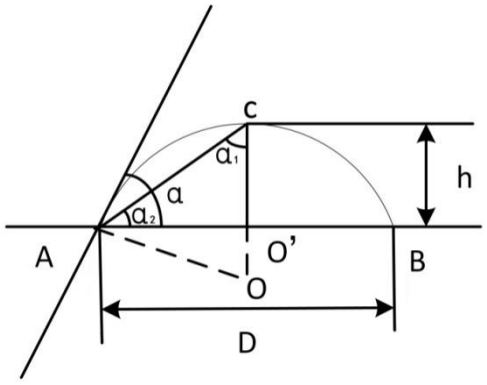

Fig. 6.10 Schematic of CA measurement.

In the diagram, *h* is the height of droplet contour, D is the diameter of the cross-section area of the micro structure and the droplet. As shown in Fig. 6.10, in the right triangle ACO':

$$\alpha_1 + \alpha_2 = 90^\circ \tag{6.4}$$

$$\alpha = 90^\circ - (\alpha_1 - \alpha_2) = (\alpha_2 + \alpha_1) - (\alpha_1 - \alpha_2) = 2\alpha_2 \tag{6.5}$$

$$\tan\alpha_2 = \frac{h}{r}, \quad \alpha_2 = \arctan\frac{h}{r} = \arctan\frac{2h}{D} \tag{6.6}$$

The CA can be calculated by $\alpha = 90^\circ - 2\delta$ and $\alpha_2 = 45^\circ - \delta$ .The value of δ is positive when $\alpha > 90^o$ and negative when $\alpha < 90^o$.

As presented in Fig. 6.6, the CA values of all samples are below 90^o and the samples modified with the structures of micro grooves show the lower CA values compared with untreated sample which makes the surfaces more hydropholic. The CA values of samples with the micro dotted and dimpled structures were higher than that of the untreated sample. The CA value of 58^o of the untreated sample was also measured for comparison. The letters before the sample index were used to identify the samples

with different microstructures that the letters D, d and G represented the dotted, dimpled and grooved micro structured samples, respectively.

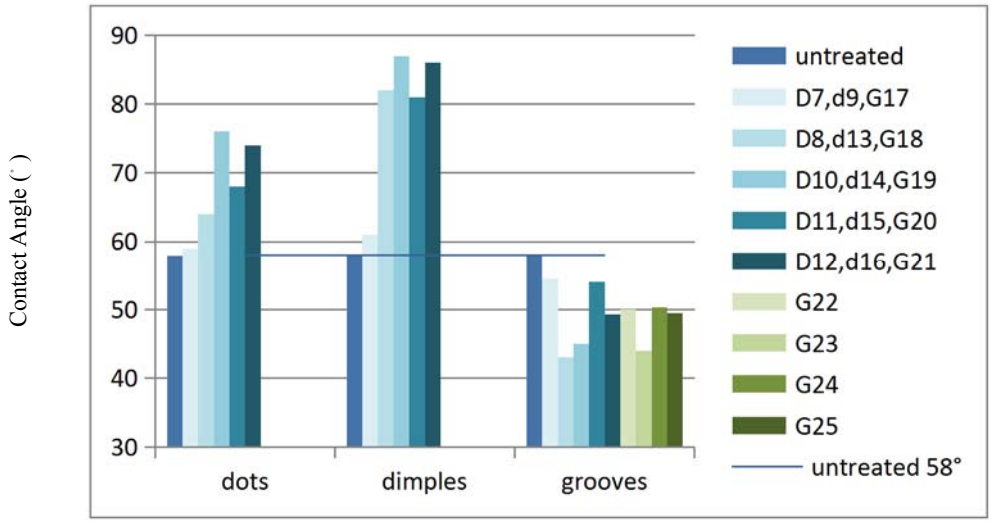

Fig. 6.11 CA measurements of the samples with the microstructures in dots, dimples and grooves.

It can be seen that the CA value of micro grooved structures in the periods of 10 μm and 20 μm are significantly smaller than that of untreated sample. With CA < 58°, the structures have a more pronounced hydrophilic behaviour. The grooved distribution of roughness with the average value from 0.8 μm to1.7 μm may explain the observed decrease of CA. Compared with the roughness of the untreated surface, which is 0.019, the grooved structures with the hydropholic property are more hydropholic if their roughness is greater.

As described in Section 3.2, the Cassie-Baxter model shown in Eq. (6.7) represents the relationship between CA, roughness and the factional solid-liquid area.

$$\cos\alpha = R_f \cos\alpha_0 - f_{lv}(R_f \cos\alpha_0 + 1) = R_f(f_{sl}\cos\alpha_0 - f_{sl} + 1) \qquad (6.7\ a)$$

where f_{sl} is the factional solid-liquid area and R_f, which is defined as the ratio of the contact area of solid and liquid to its flat projection, represents the roughness factor of the top of the structures.

Equation (6.7 a) can be simplified as

$$\cos\alpha = R_f^{"}(1 - C \times f_{sl}) \tag{6.7 b}$$

where $C = 1 - \cos\alpha_0$ is a constant when α_0 is given. $R_f^{"}$ represents R_f for the grooved structures. It can be seen that the CA of rough micro structured surface depends on $R_f^{"}$.

As shown in Fig. 6.12, the grooves are distributed with the width of d and the period of p.

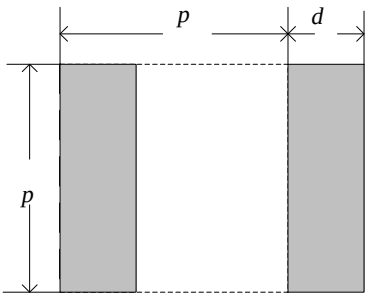

Fig. 6.12 Top views of micro grooved structures.

With the geometric parameters d and p, $R_f^{"}$ can be expressed as

$$R_f^{"} = \frac{A_g}{A_f^{"}} = \frac{d}{p} \tag{6.8}$$

Where A_g is the top area of micro grooved in its flat projection area $A_f^{"}$. For the micro

grooved structures with p= 10 μm and p=20 μm, $R_f^{''}$ was calculated as 20.3% and 17.2%, respectively. With respect to Eq. (6.13), the greater p leads to a smaller $R_f^{''}$, which results in a greater CA. The experimental results are in line with this analysis.

CA values of dotted and dimpled structures are greater that of the untreated sample, as shown in Fig. 6.11. The dotted and dimpled distribution of roughness with the average value from 0.6 μm to 1.7 μm were greater than that of untreated samples with 0.019, which may contribute to the decrease of CA values. However, the increased values of CA were observed in Fig. 6.12 which was account for the creation of air pockets between the solid structures and droplet. As discussed in Section 3.2, the presence of air pockets reduced the real contact area of solid and liquid which induced the increase of CA value.

Refer to the early discussion, it can be seen that the CA of rough micro dotted and dimpled structure surfaces depend on R_f and R_f', respectively. As shown in Fig. 6.13, the micro dots and dimples are in the triangular distribution and the top of micro dots and dimples are assumed to be circles with a radius r and p is the period, it means the distance between the dots and dimples.

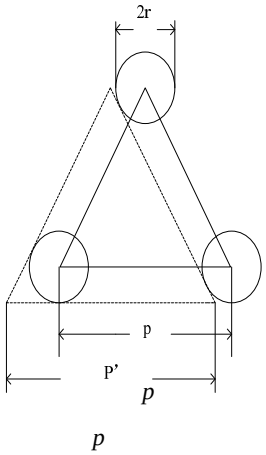

Fig. 6.13 Top views of micro dots and dimples.

For micro circular dots arranged as shown in Fig. 6.13, R_f can be calculated as

$$p' = \frac{\sqrt{3}(r + \sqrt{3}p)}{3} \tag{6.9}$$

$$A_f = \frac{1}{2} \cdot \frac{\sqrt{3}(r + \sqrt{3}p)}{3} \cdot (r + \sqrt{3}p) = \frac{\sqrt{3}(r + \sqrt{3}p)^2}{6} \tag{6.10}$$

$$R_f = \frac{A_d}{A_f} = \frac{6\pi r^2}{\sqrt{3}(r + \sqrt{3}p)^2} \tag{6.11}$$

Where A_d is the top area of single micro dot and its flat projection A_f is the area of dotted triangle. The R_f of micro dotted structures with the periods (p) of 5 μm and 10 μm was calculated as 23.7% and 38.3% according to Eq. (6.11) by measuring the average radius (r) of dots with 1.5 μm and 4 μm based on Figs. 6.5 (A) and (C). It can be seen that the micro dotted structures with a larger period and radius induced a greater R_f', which leads to a greater CA value.

Figure 6.13 can also be used for micro dimpled structures and the dimples are assumed to be circles with the radius r and p is the period. The parameter R_f' of micro dimpled structures can be calculated as

$$R_f' = 1 - R_f = 1 - \frac{6\pi r^2}{\sqrt{3}(r + \sqrt{3}p)^2} \tag{6.12}$$

The R_f' of micro dimpled structures with the period (p) of 5 μm and 10 μm were calculated as 76.3% and 88.3% according to Eq. (6.12) by measuring the average radius (r) of dimples with 1.5 μm and 2 μm as observed in Figs. 6.5 (B) and (D). With respect to Eq. (6.3), the greater period and radius lead to the greater R_f', which induces

a greater CA value as described in Fig. 6.11.

The microstructures in dots, dimples and grooves have their influence on wettability which is directly measured by CA values. The micro grooved structures with the periods of 10 μm and 20 μm exhibited the more hydropholic property with the decreased CA values, and the micro dotted and dimpled structures with the periods of 5 μm and 10 μm had the negative effect on the hydropholic property with the increased CA values.

6.4 Biological Experiments [173]

The aim of the experiments is to investigate the impacts of microstructures in grooves, dimples and dots on the proliferation, morphology, spreading and adhesion of cells.

6.4.1 Cell Culture

MG63 osteoblast cells (CTCCBIOSCIENCE Inc (China Tech)) were cultured on the structured samples. Total eighty samples divided in four groups with samples 1-19 and 1 untreated sample in each group were used for culturing MG63 osteoblast cells for 4 h, 48 h, 72 h and 144 h [167], respectively. The untreated polished samples were used in each group as the control sample. In order to simulate the growth environment of MG63 osteoblast cells, they were incubated in 25 cm^2 flasks and maintained under

the incubation conditions (37 °C and 5% CO_2). Minimum essential media with 10% fetalbovine serum and 1% ampicillin and streptomycin sulphate were prepared for culturing cells. The cells were passaged before the confluence. In the experiments, the cells were used between passages 10 and 15 which were easy to observe.

Before seeding, the total 80 (four groups) Ti-6Al-4V samples were cleaned for cell proliferation. The ultrasonic method was used to clean the samples. Acetone, ethanol and deionized water were sequentially employed for 30 min cleaning. All samples were dried in the air in a clean room. The samples were then placed in two 48-well plates. The well plates with the samples were sterilized for 12 h using ultraviolet light. After the sterilization treatment, the phosphate buffer saline (PBS) was used to rinse the impurities. MG63 osteoblast cells were trypsinized and cultured on the samples with the concentration 4×10^5 cells·ml^{-1} in the ratio of 0.2 ml·well^{-1}for the hemocytometer count. After the cells were seeded for 4 h, most cells were attached on the samples. For comparison, four polished untreated Ti-6Al-4V alloy samples were seeded with MG63 osteoblast cell at the same density. The multi-well plates were incubated with 5% CO_2 at 37 °C. The culture media were changed every two days to prevent the contamination of growth environment.

6.4.2 Cell Proliferation

The 3- (4, 5-dimethyl-2-thiazolyl) -2, 5-diphenyl-2-H-tetrazolium bromide (MTT) method was used to evaluate cell proliferation with the advantages of high accurate, simplicity and repeatability of results [168, 169]. The mitochondrial activity of the

MG63 osteoblast cells seeded on the samples in different culture time periods (4 h, 48 h, 72 h, and 144 h) was determined with the MTT colorimetric assay. At the end of each period, the media were removed, and the samples were rinsed with PBS. The cells were cultured in the MTT bromide medium and culture medium at 5% CO_2 (37 °C, 4 h) to allow the formation of formazan crystals. The ratio of the MTT bromide medium and culture medium was 1:5. After the removal of the medium, the dimethylsulfoxide solution was added to the wells. After 20 min, the dark-blue crystal of MTT formazan was completely dissolved, and the solution was transferred to the 96-well plates. The absorbance measurements of contents in each well were made at the wavelength 498 nm with the 96-well microplate reader of a spectrophotometer. Each experiment was performed in triplicates, and the data were presented as average optical density (OD) values.

MTT assays at the 4 h, 48 h, 72 h and 144 h post seeding were performed to evaluate the attachment and proliferation of cells. The experiment results are shown in Fig. 6.14. Table 6.7 presents the proliferation rates of osteoblast cells on the untreated polished and structured samples, calculated using the following equation.

$$R = \frac{OD_2 - OD_1}{OD_1} \times 100\% \tag{6.13}$$

where R is the proliferation rate, OD_2 is the optical density at the end of culture time, OD_1 stands for the optical density at the beginning of culture time. The number of cells showed a rising trend with the increase of time. The MTT assays showed that the cells were almost not affected in the culturing stage for 4 h. Samples 11-15, 23 and 24 with greater roughness showed significant and positive effects on the cell initial stage of adhesion. After 48 h, the cells with similar activities were adhered to the

microstructures in grooves, dimples and dots structures and the polished untreated surfaces. After 72 h, all textured surfaces had positive effects on the cell proliferation, and micro dotted structures with the period of 5 μm showed the significant increase. The obvious cell proliferation increase of micro dimpled structures with the period of 10 μm (samples 13-16) and micro grooved structures with the period of 20 μm (samples 22- 25) were observed after 144 h.

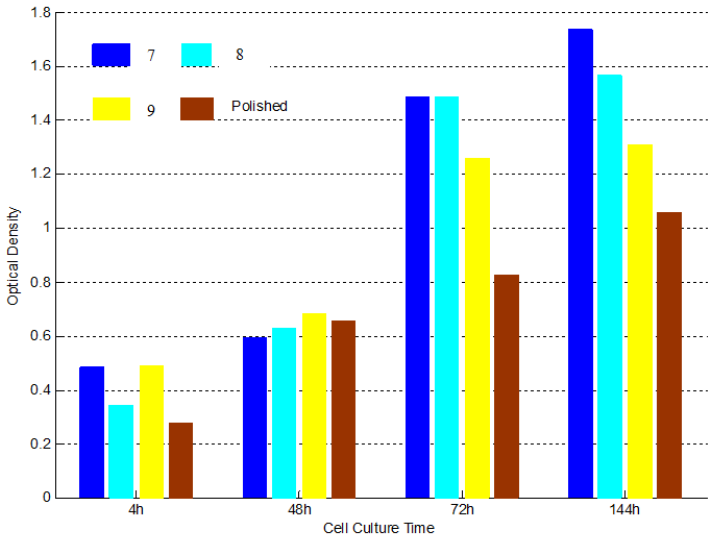

(A)

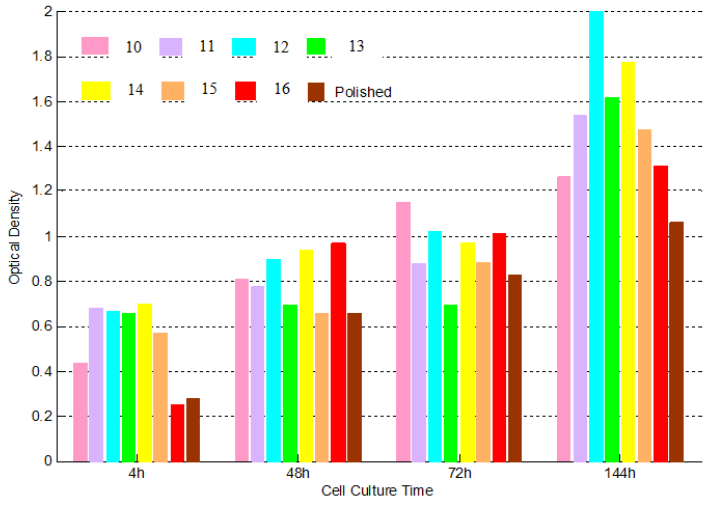

(B)

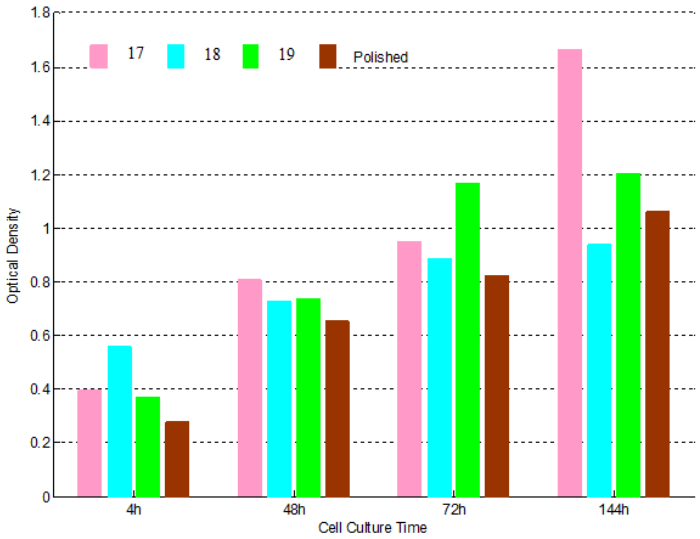

(C)

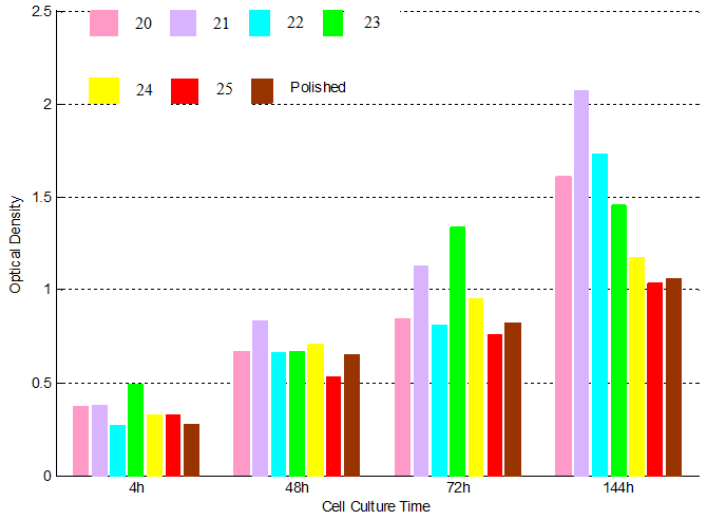

(D)

Fig. 6.14 Proliferation of MG-63 osteoblast cells on the textured surfaces after 4 h, 48 h, 72 h and 144 h.

It can be seen from Table 6.7 that the proliferation rates of the structured surfaces are higher than those of the polished untreated surfaces which are attributed to the increasing roughness. Micro dotted structures (samples 7, 8, 10, 11 and 12) with the roughness from 0.8 μm to 1.5 μm had the greater proliferation rate and sample 12 with the roughness of 1.21 μm presented the greatest proliferation rate of 5.48. As shown in Fig. 6.14, samples with greater roughness show the better initial response of cell.

However, with the increase of culture time, the cell proliferation is not only depended on the roughness but also the microstructures. For the similar degree of roughness and same periods, the micro dotted structure (samples 8 and 12) showed the greater proliferation rate than those of micro dimpled structures (samples 9 and 13), respectively. This phenomenon could be explained that the micro dotted structures induced the increase of contact areas of cells and solid surfaces which had the positive effect for cell proliferation. For the micro grooved structures with the roughness from 0.8 μm to 1.7 μm, samples with the period of 10 μm showed the greater proliferation of cells attributed to the reduction of contact area of cells and micro grooved structures.

The microstructures in dots, dimples and grooves have their effect on cell proliferation. The micro dotted structures presented the best cell proliferation and the micro grooved structures with the period of 10 μm exhibited the greater cell proliferation compared with that of grooved structures with the period of 20 μm.

Table 6.7 Proliferation rates of osteoblast cells on the polished and structured substrates.

Sample	7	8	9	10	11
Proliferation rate (×100%)	4.26	3.56	1.68	3.28	4.46
Sample	12	13	14	15	16
Proliferation rate (×100%)	5.48	1.97	2.61	2.53	2.61
Sample	17	18	19	20	21

Proliferation rate (×100%)	3.19	2.34	2.23	1.91	1.27
Sample	22	23	24	25	Polished
Proliferation rate (×100%)	2.01	1.46	1.54	1.59	1.18

6.4.3 Cell Spreading and Attachment

Because of their higher cell proliferation rates, samples 17, 19, 9, 7, 14, 12 and 16 were selected to evaluate cell spread and attachment using the typical morphology of MG63 osteoblast cells. The culturing of cells was completed by following the method described above on the seven samples and one untreated polished sample. When the cell culture completed, the culture media were removed, and the samples were rinsed three times using the PBS solution. Then the cells were fixed with 4% paraformaldehyde for 20 min. Then, the PBS solution and deionized water were used to rinse the samples three times. These procedures provided maximum protection of cell morphology. When the samples were dried at room temperature, cell morphologies were examined with a SEM (FEI QUANTA-250 FEG) at 5 kV. The cells cultured on polished untreated surfaces were also examined with the SEM.

The attachment and spreading of cells on untreated polished samples and samples 17, 19, 9, 7, 14, 12 and 16 were then evaluated by the typical morphology of MG63 osteoblast cells as shown in Fig. 6.15. The cells were spread on the surfaces and the growing status was good. The sizes of cells were different after spreading, and they were about 50 μm in diameter on the DLIL structured surfaces. The cells on the

untreated polished surfaces were a little smaller than those on the structured surfaces. The cells on the structured surfaces were more extended than those on the polished surfaces. Especially, the cells cultured on the grooved structure surfaces were aligned in the groove direction. The most of cells presented elongated spindle shapes and good conditions. On the other hand, the cells on the dotted and dimpled structure surfaces and polished surfaces did not align in any particular direction unless the modulation grooved structure occurred in the isotropic structure. The cells aligned in aparticular direction in Fig. 6.15 (G) because the modulation grooved structure existed among the dimpled structures. It was demonstrated that the micro grooved structures with the periods of 10 μm and 20 μm promoted cells' growth aligning in groove directions.

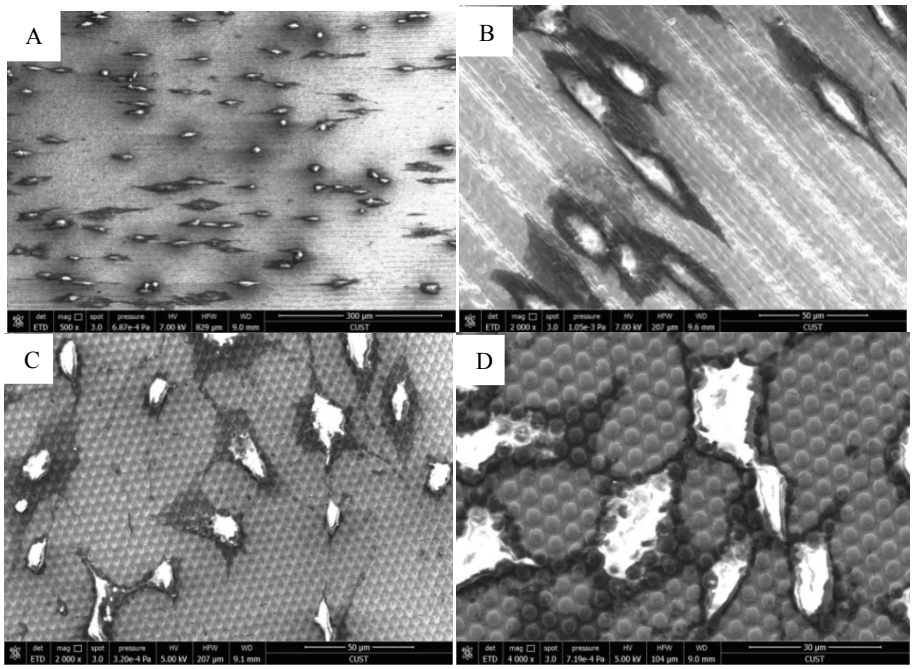

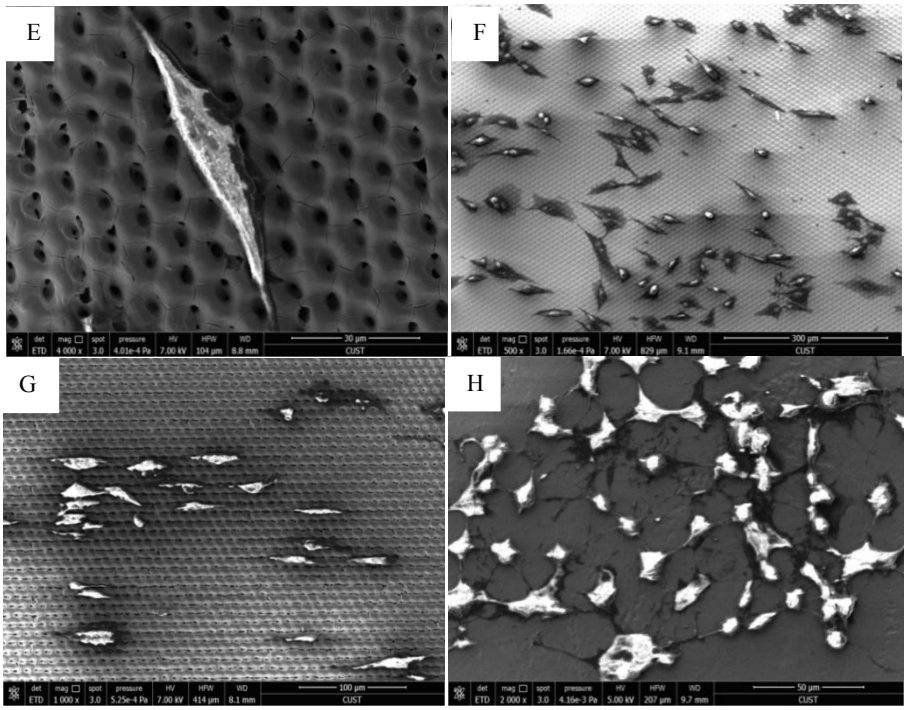

Fig. 6.15 SEM images of MG-63 osteoblast cells cultured for 48 h on microstructures: (A) Grooved structures with period of 10 μm; (B) Grooved structures with period of 20 μm; (C) Dimpled structures with period of 5 μm; (D) Dotted structures with period of 5 μm; (E) Dimpled structures with period of 10 μm; (F) Dotted structures with period of 10 μm; (G) Dimpled structures with period of 10 μm; (H) Untreated polished structures.

6.4.4 Cell Adhesion

The enzymatic detachment is often used to study the adhesion properties of biomaterials [170,171]. Due to the relative lower CA, the adhesive properties of MG63 osteoblast cells on structured samples 18, 23, 7, 9, 10 and 15 for 48 h were assessed [147]. In this work, enzymatic detachments were carried out with 0.25% (w/v) trypsin solutions. Three groups with the same six samples (18, 23, 7, 9, 10 and

15) were exposed totrypsin solutions at room temperature. They were then rinsed with 1 ml PBS, and the liquids were collected. The procedure was repeated four times. The liquids were then examined for counting cell numbers by hemocytometer. Three groups with the same samples (18, 23, 7, 9, 10 and 15) were carried out for the experiments for the trypsin treatment time durations of 6 min, 12 min and 18 min. The data obtained were employed for the establishment of the relationship between the trypsin treatment time and the percentage of cells detached.

The enzymatic detachment results presented the relationships between the cell adhesion and surface topography. Fig. 6.16 shows the percentage number of detachment cells with different treatment time durations. The sample surfaces with microstructures in dimples and dots had steep slopes for the first 6 min and the slopes of grooved structures were relatively moderate. It was demonstrated that the cell detachment rates of dotted and dimpled structures were higher than those of grooved structures. For the grooved structures, the percentage numbers of detachment cells were always less than dimpled and dotted structures. The higher percentage number of detachment cells means the weaker adhesion. It is more obvious on the 20 μm grooved surfaces, provided the best cell adhesion performance. The phenomenon can be explained that the size of cells has a significant influence on the optimal groove spacing [172]. The diameter of osteoblast cells used in this research was about 20 μm before spreading so that the micro grooved structure with the period of 20 μm performed the best cell adhesion.

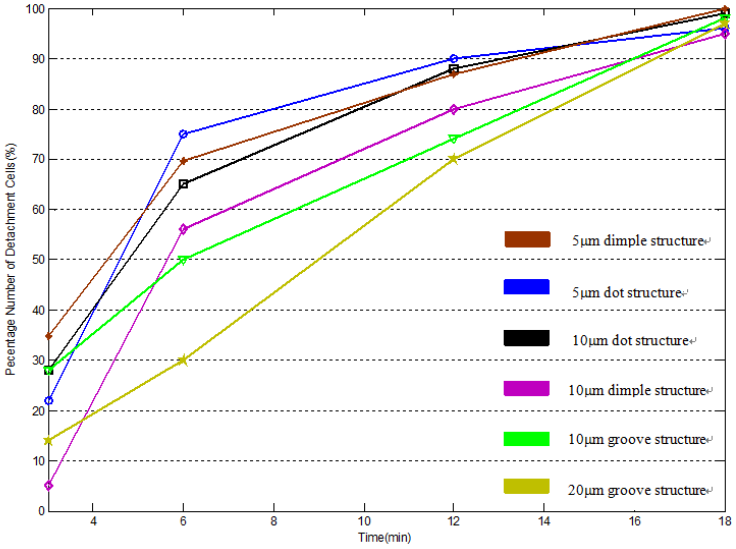

Fig. 6.16 Enzymatic detachment curves for the MG63 osteoblast cells on structured surfaces for 48 h.

6.5 Summary

The incident angle, polarisation angle and azimuthal angle were adjusted by simulations to design micro structures in periods of 5 μm, 10 μm and 20 μm. According to simulation results, microstructures in grooves, dimples and dots were fabricated on the Ti-6Al-4V implant alloy by two- and three- beam DLIL systems to improve the biocompatibility of cell proliferation, spreading and adhesion of MG-63 osteoblast cells.

- The optimal settings of incident angle, polarisation angle and azimuthal angle were obtained for the formation of grooved patterns with the periods of 10 μm and 20 μm and dimpled and dotted patterns with the periods of 5 μm and 10 μm.

- The proper laser fluence and exposure duration were achieved for the fabrication

of microstructures in grooves, dimples and dots with the roughness from 0.6 μm to 1.7 μm to improve the cell proliferation of MG-63 osteoblast cells and the micro dotted structures showed the best performance in cell proliferation, especially, the dotted structure with the roughness of 1.473 μm had the best proliferation rate. The cell spreading on microstructures was evaluated by the morphology of MG63 osteoblast cells which were observed by SEM. The SEM results indicated that the cells had their great orientation on the grooved structured surfaces or the modulation grooved structures occurred in the isotropic structures. However, the cell spreading on the polished, dotted and dimpled structure surfaces exhibited random orientations. The cells cultured on the DLIL grooved surfaces appeared to align in the directions of grooves, which promoted the contact guidance to avoid scar tissue formation.

- The optimal setting of laser fluence and exposure duration were also obtained for the fabrication of microstructures in grooves, dimples and dots with hydropholic properties to promote the cell adhesion. The hydropholic grooved structures with the period of 20 μm and lower CA had better cell adhesion of MG-63 osteoblast cells.

- The micro dotted and dimpled structures with the periods of 5 μm and 10 μm, and the grooved structures with the periods of 10 μm and 20 μm showed the significant greater R_a ranged from 0.6 μm to 1.7 μm compared with that of untreated surface. The micro grooved structures with the periods of 10 μm and 20 μm exhibited the more hydropholic property with the decreased CA values and the micro dotted and dimpled structures with the periods of 5 μm and 10 μm had the negative effect on the hydropholic property with the increased CA values.

- In this work, It was observed that the surface with the microstructures of grooves, dots and dimples were capable of promoting cell proliferation, spreading and adhesion. The surfaces with such microstructures can be used to influence the cellular activities and enhance the biocompatibility in order to reduce the formation of scar tissue and promote bone bonding degree. DLIL provide a highly controllable, multi-scale and defect-free fabrication technology to create microstructures for the biocompatible surfaces of implant materials.

CHAPTER 7

CONCLUSIONS AND FUTURE WORK

7.1 Conclusions

DLIL as a highly controllable method was developed to fabricate well-designed micro and nano structures with optimal feature sizes for realising superhydrohpobic, wear resistance and biocompatibility in implant biomaterials including silicon, Co-Cr-Mo alloy and Ti alloy. This work provides the potential of DLIL in surface modification and the innovative approaches are highlighted in the following:

- Four-beam laser interference was developed to design and fabricate hierarchical micro and nano structures in the period of 5.5 μm and the aspect ratio of 2-3. The optimal settings of process parameters including incident angle, azimuthal angle, polarize angle, laser fluence and exposure duration were obtained by simulation and fabrication processes to achieve the superhydrophobic property.

- Three-beam laser interference was developed to fabricate periodic micro circular dimpled structures on artificial hip joints (Co-Cr-Mo alloy) with improving wear resistant property including a 64% friction coefficient reduction and 42% hardness enhancement. The dimpled structures with the period of 8 μm and the dimple area densities of 14.8% were achieved by the proper settings of process parameters..

- Two- and three-beam DLIL were developed to form micro grooved structures with periods of 10 μm and 20 μm and micro dimpled/dotted structures with the

periods of 5 μm and 10 μm respectively on Ti-6Al-4V implant alloys to improve biocompatibility by promoting the proliferation, spreading and adhesion of MG-63 osteoblast cells.

7.2 Future Work

In this work, DLIL was developed to improve the biocompatibility to MG-63 osteoblast cells (10 μm-20 μm) on Ti-6Al-4V implant alloy. However, it is not sufficient for long-life implantation due to the bacterial infection of staphylococcus aureus (100 nm-800 nm) occurred during the interaction of materials and biological surroundings. Due to the feature sizes of MG-63 osteoblasts and staphylococcus aureus, the following issues need to be further explored to achieve the structures on Ti-6Al-4V implant alloy with biocompatibility and antibacterial property. Finally, the multi-objective optimization solutions will be developed.

- To simulate interference cross-scale patterns with the periods of 100 nm to 800 nm in modulation periods from 10 μm to 20 μm by MATLAB with multi-beam laser interference by adjusting the laser beam number, incident angle, azimuthal angle and polarisation direction.

- To fabricate nano structures with the periods from 100 nm to 800 nm in modulation periods of 10 μm and 20 μm to achieve cross-scale structures by adjusting the laser fluence and exposure duration. Staphylococcus aureus will be cultured to study bacterial proliferation, spread and adhesion to evaluate

antibacterial properties.

- The multi-objective optimization solutions will be developed between the process parameters of DLIL and surface functionalities including wear resistant property, biocompatibility and antibacterial property.

REFERENCES

[1] A. Unsworth. (1981) In an introduction to the bio-mechanics of joints and joint replacement. *Mechanical Engineering Publications Limited, London*, 134-139.

[2] H. Sawano, S. Warisawa and S. Ishihara. (2009) Study on long life of artificial joints by investigating optimal sliding surface geometry for improvement in wear resistance. *Precision Engineering,* 33, 492-498.

[3] J. Wang, J. Diaz, A. Sabokbar, N. Athanasou, F. Kjellson, K. Tanner, I. McCarthy and L. Lidgren. (2005) In vitro and in vivo biological responses to a novel radiopacifying agent for bone cement. *Journal of The Royal Society Interface,* 2, 71-78.

[4] A. Chyr, M. Qiu, J. Speltz, R. Jacobsen, A. Sanders and B. Raeymaekers. (2014) A patterned microtexture to reduce friction and increase longevity of prosthetic hip joints.*Wear,* 315, 51-57.

[5] G. Labek, M. Thaler, W. Janda, M. Agreiter and B.Stöckl. (2011) Revision rates after total joint replacement cumulative results from worldwide joint register data sets. *The Journal of Bone and Joint Surfery,*93, 293-297.

[6] A. Rajpura, D. Kendoff and T. Board. (2014) The current state of bearing surfaces in total hip replacement. *The Bone& Joint Journal,* 96, 147-156.

[7] K. Bozic, S. Kurtz, E. Lau, K. Ong, T. Vail and D. Berry. (2009) The epidemiology of revision total hip arthroplasty in the United States. *The Journal of Arthroplasty,* 24, 128-133.

[8] J. Resendiz, E. Graham, P. Egberts and S. Park. (2015) Directional friction surfaces through a symmetrically shaped dimpled surfaces patterned using inclined flat end milling. *Tribology International,* 91, 67-73.

[9] L. Mattei, F. DiPuccio, B. Piccigallo and E. Ciulli. (2011) Lubrication and wear modeling of artificial hip joints: are view. *Tribology International,* 44, 532-549.

[10] G. Wu, P. Li, H. Feng, X. Zhang and P. Chu. (2015) Engineering and functionalization of biomaterials via surface modification. *Journal of Materials Chemistry,* 3, 2024-2042.

[11] S. Watari, K. Hayashi, J. Wood, P. Russell, P. Nealey, C. Murphy and D. Genetos. (2012) Modulation of osteogenic differentiation in hMSCs cells by submicron topographically-patterned ridges and grooves. *Biomaterial,* 33, 128-136.

[12] A. Ross, A. Jiang, M. Bastmeyer and J. Lahann. (2012) Physical aspects of cell culture substrates: topography, roughness, and elasticity. *Small,* 8,336-355.

[13] E. Ivanova, J. Hasan, H. Webb, G. Gervinskas, S. Juodkazis, V. Truong, A. Wu, R. Lamb, V. Baulin, G. Watson, J. Watson, D. Mainwaring and R. Crawford. (2013) Bactericidal activity of black silicon. *Nature Communications,*4, 1-7.

[14] T. Lu, Y. Qiao and X. Liu. (2012) Surface modification of biomaterialsusing plasma immersion ionimplantation and deposition. *Interface Focus,* 2, 325-336.

[15] P. Chu, J. Chen, L. Wang and N. Huang. (2002) Plasma-surface modification of biomaterials. *Materials Science and Engineering: R: Reports,* 36, 143-206.

[16] G. Lamour, A. Eftekhari-Bafrooei, E. Borguet, S. Soues and A. Hamraoui. (2010) Neuronal adhesion and differentiation driven by nanoscale surface free-energy gradients. *Biomaterials,* 31, 3762-3771.

[17] G. Bendas and L. Borsig. (2012)Cancer cell adhesion and metastasis: selectins, integrins,and the inhibitory potential of heparins. *International Journal of Cell Biology,* 1-10.

[18] D. Hoffman-Kim, J. Mitchel and R. Bellamkonda. (2010) Topography, cell response,and nerve regeneration. *Annual Review of Biomedical Engineering,* 12, 203-231.

[19] C. Yang, L. Huang, T. Shen and J. Yeh. (2010) Cell adhesion, morphology and biochemistry on nanotopographic oxidized silicon surfaces. *European Cells and Materials,* 20, 415-430.

[20] T. Ko, E. Kim, S. Nagashima, K. Oh, K. Lee, S. Kim and M. Moon. (2013) Adhesion behavior ofmouse liver cancer cells on nanostructured superhydrophobic and superhydrophilic surfaces. *Soft Matter,* 9,8705-8711.

[21] L. Han, Z. Mao, J. Wu, Y. Guo, T. Ren and C. Gao. (2013) Unidirectional migration of single smooth muscle cells under the synergetic effects of gradient swelling cur and parallel groove patterns. *Biointerfaces,*111, 1-6.

[22] E. Chikarakara, S. Nather and D. Brabazon. (2010) Process mapping of laser surface modification of AISI 316L stainless steel for biomedical applications. *Applied Phsics A,* 101, 367-371.

[23] A. Lasagni, C. Gachot, K. Trinh, M. Hans, A. Rosenkranz, T. Roch, S. Eckhardt, T. Kunze, M. Bieda, D. Günther, V. Lang, and F. Mücklich. (2017) Direct laser interference patterning, 20 years of development: from the basics to industrial applications. *Proceeding. SPIE: Laser-based Micro- and Nanoprocessing*, 10092, 1-11.

[24] J. Berger, T. Roch, N. Pistillo, and A. F. Lasagni. (2016) Multiple-beam laser patterning on aluminum oxide, zirconium oxide, andhydroxyapatite ceramic materials using a microlens array. *Journal of Laser Applications,* 28, 042003-1-042003-8.

[25] F. Roßler, D. Gunther and A. Lasagni. (2016) Fabrication of hierarchical micro patterns on PET substrates using direct laser interference patterning. *Advanced Engineering Materials,* 18, 1755-1762.

[26] V. Lang, T. Roch and A. Lasagni. (2016) High-speed surface structuring of polycarbonate using direct laser interference patterning: toward $1m^2$ min^{-1} fabrication speed barrier. *Advanced Engineering Materials,* 18, 1342-1348.

[27] T. Schiefer, I. Jansen, M. Bieda, J. Pap and A. Lasagni. (2015) Large area

surface structuring by direct laser interference patterning for adhesive bonding applications. *Journal of The Adhesion Sciety of Japan,* 51, 223-224.

[28] Y. Zabila, M. Perzanowski, A. Dobrowolska, M. Kac, A. Politand M. Marszałek. (2009) Direct laser interference patterning: theory and application. *Acta Physica Polonica A,* 115, 591-593.

[29] G. Liu, J. Zhang and C. Zhou. (2011) Implementation method for three-beam laser interference lithography. *High Power Laser and Particle Beams,* 23, 3250-3254.

[30] X. Wu. (2015) Influence study of polarization on three-beam interference. *ACTA Optica Sinica,* 35, 1012002-1.

[31] L. Zhao, Z. Wang, J. Zhang, M. Yu, S.Li, D. Li and Y. Yue. (2015) Effects of laser fluence on silicon modification by four-beam laser interference. *Journal of Applied Physics,* 118, 233106.

[32] S. Tao, Y. Zhou, B. Wu and Y. Gao. (2012) Infrared long nanosecond laser pulse ablation of silicon: Integrated two-dimensional modeling and time-resolved experimental study. *Applied Surface Science*, 258, 7766-7773.

[33] S. Xia, X. Lv, X. Wang, J. He, W. Wang and Z. Dou. (2016) Research advance of measurement of thermo-physical property of micro-nano material with femtosecond laser. *Laser Technology,* 40, 506-511.

[34] D. Liu and D. Zhang. (2007) Vaporization and Plasma Shielding during high power nanosecond laser ablation of silicon and Nickel. *Chinese Physical Letter,* 25, 1368-1371.

[35] X. Tan, D. Zhang, B. Yu, Z. Li, G. Li and L. Li. (2005) Vaporization effect studying on high-power nanosecond pulsed laser deposition. *Physica B,* 358, 86-92.

[36] X. Wu. (2015) Influence study of polarization on three-beam interference. *ACTA Optica Sinica,* 35, 1012002-1.

[37] J. Park, W. Leung, K. Constant, S. Chaudhary, T. Kim and K. Ho. (2011) Laser interference lithography for fabricating nanowires and nanoribbons. *Nanowires-Implementations and Applications,* 21,471-484.

[38] B. Valamehr, S. Jonas, J. Polleux, R. Qiao, S. Guo, E. Gschweng, B. Stiles, K. Kam, T. Luo, O. Witte, X. Liu, B. Dunn and H. Wu. (2008) Hydrophobic surfaces for enhanced differentiation of embryonic stem cell-derived embryoid bodies. *Proceedings of the National Academy of Sciences,* 105, 14459-14464.

[39] D. Dowling, I. Miller, M. Ardhaoui and W. Gallagher. (2011) Effect of surface wettability and topography on the adhesion of osteosarcoma cells on plasma-modified polystyrene. *Journal of Biomaterials Applications,* 26, 327-347.

[40] W. Tsai and J. Lin. (2009) Modulation of morphology and functions of humanhepatoblastoma cells by nano-grooved substrata. *Acta Biomaterialia,* 5, 1442-1454.

[41] D. Wu, S. Wu, Q. D. Chen, S. Zhao, H. Zhang, J. Jiao, J. A. Piersol, J. N. Wang, H. Sun and L. Jiang. (2011) Facile creation of hierarchical PDMS microstructures with extreme underwater superoleophobicity for anti-oil application in microfluidic channels. *Lab on a Chip,* 11, 3873-3879.

[42] E. Yim, R. Reano, S. Pang, A. Yee, C. Chen, and K. Leong. (2005) Nanopattern-induced changes in morphology and motility of smooth muscle cells. *Biomaterials,* 26, 5405-5413.

[43] Y. Song, Y. Ju, Y. Morita, and G. Song. (2013) Effect of the nanostructure of porous alumina on growth behavior of MG63 osteoblast-like cells. *Journal of Bioscience and Bioengineerin,* 116, 509-515.

[44] S. Watari, K. Hayashi, J. Wood, P. Russell, P. Nealey, C. Murphy and D. Genetos. (2012) Modulation ofosteogenic differentiation in hMSCs cells by submicrontopographically-patterned ridges andgrooves. *Biomaterials,* 33, 128-136.

[45] G. Lamour, A. Eftekhari-Bafrooei, E. Borguet, S. Soue, and A. Hamraoui. (2010) Neuronal adhesion and differentiation driven by nanoscale surfacefree-energy gradients. *Biomaterials,* 31, 3762-3771.

[46] D. Coblas, A. Fatu, A. Maoui and M. Hajjam. (2014) Manufacturing textured surfaces:State of art and recent developments. *Journal of Engineering Tribology,* 229, 3-29.

[47] J. Park, J. Moon, H. Shin, D. Wang and M. Park. (2006) Direct-write fabricationof colloidal photonic crystal microarrays by ink-jetprinting. *Journal of Colloid Interface Science,* 298, 713-719.

[48] M. Myint, R. Kitsomboonloh, S. Baruah and J. Dutta. (2011) Superhydrop50hobic surfaces using selected zinc oxidemicrorod growth on ink-jetted patterns. *Journal of ColloidInterface Science,* 354, 810-815.

[49] N. Tay, M. Minn and S. Sinha. (2011) Polymer jet printingof SU-8 micro-dot patterns on Si surface: optimizationof tribological properties. *Tribology Letters,* 42, 215-222.

[50] N. Tay, M. Minn and S. Sinha. (2011) A tribological study of SU-8 micro-dots printed on Si surface in flat-on-flatreciprocating sliding test. *Tribology Letters,* 44,167-176.

[51] K. Gangopadhyay, P. Willermet, W. Vassell and M. Tamor. (1997) Amorphous hydrogenated carbon films for tribologicalapplications. II. Films deposited on aluminum alloysand steel. *Tribology International,*30, 19-33.

[52] M. Hua, H. Tam, H. Ma and C. Mok. (2006) Patterned PVDTiN spot coatings on M2 steel: tribological behaviorsunder different sliding speeds. *Wear,* 260, 1153-1165.

[53] M. Hua, H. Ma, J. Li and C. Mok. (2006) Tribological behaviours of patterned PVD TiN spot coatings on M2 steel coatedwith different bias voltages. *Surface &Coatings Technology,*200, 3612-3625.

[54] J. Lin, M. Liu and J. Wu. (1996) Analysis of the frictionand wear mechanism

of structural ceramic coatings. Part 2: the effect of operating conditions and substratematerial. *Wear,* 198, 7-14.

[55] J. Li and X. Liu. (2015) Chemical surface modification of metallic biomaterials. *Surface Coating and Modificaiton of Metallic Biomaterials,* 159-183.

[56] J. Li, X. Liu, Y. Qiao, H. Zhu and Ding C. (2014) Antimicrobial activity and cytocompatibilityof Ag plasma-modified hierarchical TiO_2 film on titanium surface. *Colloids and Surfaces B:Biointerfaces,* 113,134-145.

[57] J. Rieu, A. Pichat, L.Rabbe, A. Rambert, C. Chabrol and M. Robelet. (1991) Ion implantation effects on friction and wear of joint prosthesis materials. *Biomaterials,* 12, 139-143.

[58] V. Kalita, D. Komlev, V. Komlev, and A. Radyuk. (2016) The shear strength of three-dimensional capillary-porous titanium coating for intraosseous implants. *Materials Science and Engineering C,* 60, 255-259.

[59] Y. Uyama, K. Kato and Y. Ikada. (1998) Surface Modification of Polymers by Grafting. *Advances in Polymer Science,* 137.

[60] D. Falconnet, G. Csucs, H. Grandin, and M. Textor. (2006) Surface engineering approaches to micropattern surfaces for cell-based assays. *Biomaterials,* 27, 3044-3063.

[61] T. Minamizato. (1990) Slip-cast zirconia dental roots with tunnels drilled by laser process. *The Journal of Prosthetic Dentistry,* 63, 677-84.

[62] B. Kasemo and J. Gold. (1999) Implant surfaces and interface processes. *Advances in Dental Research,* 13, 8-20.

[63] J. Norton, K. Malik, J. Darr, and I. Rehman. (2006) Recent developments in processing and surfacemodification of hydroxyapatite. *Advances in Applied Ceramics,* 105, 113-139.

[64] J. Berger and T. Roch. (2016) Multiple-beam laser patterning on aluminum

oxide, zirconium oxide, and hydroxyapatite ceramic materials using a microlens array. *Journal of Laser Applications,* 28, 042003.

[65] J. Parreira, C. Gallo and H. Costa. (2012) New advances onmaskless electrochemical texturing (MECT) for tribologicalpurposes. *Surfaceand Coatings Technology,* 212, 1-13.

[66] N. Pugno. (2007) Toward a Spiderman Suit: large invisible cables and self-cleaning releasable super adhesive materials. *Journal of Physics-Condensed Matter,* 19,395001.

[67] H. Costa and I. Hutchings. (2006) Reciprocating lubricatedsliding on textured steel surfaces. *Cie ˆncia eTecnologia dos Materiais,*18,1-2.

[68] X. Wang, K. Kato, K. Adachi and K. Aizawa. (2003) Loads carrying capacitymap for the surface texture design of SiC thrustbearing sliding in water. *Tribology International,* 36, 189-197.

[69] Y. Zheng, D. Banerjee and H. Fraser. (2016) A nano-scale instability in the β phase of dilute Ti-Mo alloys. *Scripta Materialia,* 116,131-134.

[70] A. Hayama, P. Andrade, A. Cremasco and R. Caram. (2013) Effects of composition and heat treatment on the mechanical behavior of Ti-Cu alloys. *Materials & Design,* 55, 1006-1013.

[71] Y. Mantani and M. Tajima. (2006) Phase transformation of quenched α'' martensite by aging in Ti-Nb alloys. *Materials Science and Engineering A,* 438-440, 315-319.

[72] F. Cardoso, P. Ferrandini, S. Eder, A. Cremasco and R. Caram. (2014) Ti–Mo alloys employed as biomaterials: Effects of composition and aging heat treatment on microstructure and mechanical behavior. *Journal of the Mechanical Behavior of Biomedical Materials,* 32, 31-38.

[73] D. Wang, Z. Wang, Y. Yue, J. Yu, C. Tan, D. Li, R. Qiu, and C. Maple. (2015) Determination of beam incidence conditions based on the analysis of laser

interference patterns. *Optik-International Journal for Light and Electron Optics,* 126, 2902-2907.

[74] D. Wang, Z. Wang*, Z. Zhang, Y. Yue, D. Li, and C. Maple. (2013) Effects of polarization on four-beam laser interference lithography. *Applied Physics Letters,* 102, 0819031-5.

[75] J. Xu, Z. Wang, Z. Zhang, D. Wang, and Z. Weng. (2014) Fabrication of moth-eye structures on silicon by direct six-beam laser interference lithography. *Journal of Applied Physics,* 115, 2031011-5.

[76] Z. Zhang, Z. Wang, D. Wang, and Y. Ding. (2014) Periodic antireflection surface structure fabricated on silicon by four-beam laser interference lithography. *Journal of Laser Applications,* 26, 0120101-6.

[77] D. Acevedo, H. Salavagione, A. Lasagni, E. Morallon, F. Mucklich, and C. Barbero. (2009) Fabrication of highly ordered arrays of platinum nanoparticles using direct laser interference patterning. *ACS Applied Materials & Interfaces,* 1, 549-551.

[78] M. Castro, A. Lasagni, H. Schmidt, and F. Mucklich. (2008) Direct laser interference patterning of multi-walled carbon nanotube-basedtransparent conductive coatings. *Applied Surface Science,* 254, 5874-5878.

[79] M. Hans, C. Gachot, F. Muller, and F. Mucklich. (2009) Direct laser interference structuring as a tool to gradually tune the wetting response of titanium and polyimide surfaces. *Advanced Engineering Materials,* 11, 795-800.

[80] A. Lasagni, M. Bieda, and A. Wetzig. (2011) Direct laser interference systems for the surface functionalization of powertrain components. *Global Powertrain Congress,* 64, 167-197.

[81] A. Lasagni, D. Langheinrich and S. Eckhardt. Direct fabrication of periodic patterns on polymers using laser interference. *Society of Plastics Engineers,* 28, 04203.

[82] D. Langheinrich, E. Yslas, M. Broglia, V. Rivarola, D. Acevedo and A. Lasagni. (2011) Control of cell growth direction by direct fabrication of periodic micro- and submicrometerarrays on polymers. *Journal of Polymer Science Part B: Polymer Physics,*50, 415-422.

[83] W. Barthoott and C. Neinhuis. (1997) Purity of the sacred lotus, or escape from contamination in biological surfaces. *Planta,* 202, 1-8.

[84] C. Neinhuis and W. Barthlott. (1997) Characterization and distribution of water-repellent, self-cleaning plant surfaces. *Ann Bot-london,*79, 667-677.

[85] N. Wanasekara and V. Chalivendra. (2011) Role of surface roughnesson wettability and coefficient of restitution in butterfly wings. *Soft Matter,* 7, 373-379.

[86] P. Ball (1999) Engineering shark skin and other solutions. *Nature,* 400, 507-509.

[87] L. Feng, S. Li, Y. Li, H. Li, L. Zhang, J. Zhai, Y. Song, B. Liu, L. Jiang and D. Zhu. (2002) Super-hydrophobic surfaces: from nature to artificial. *Advance Materials,* 14, 1857-1860.

[88] T. Young. (1805) An essay on the cohesion of fluids. *Philosophical Transactions of the Royal Society of London,* 95, 65-87.

[89] R. Wenzel. (1936) Risistance of solid surfaces to wetting by water. *Industrial & Engineering Chemistry,* 28, 988-994.

[90] M. Nosonovsky and B. Bhushan. (2005) Roughness optimization for fiomimetic superhydrophobic surfaces. *Microsystem Technologies,* 11, 535-549.

[91] A. Cassie and S. Baxter. (1944) Wettability of porous surfaces. *Transactions of the Faraday Society,* 40, 546-551.

[92] B. Bhushan, Y. Jung, and K. Koch. (2009) Micro-, nano- and hierarchicalstructures for superhydrophobicity, self-Cleaning and low

adhesion. *Philosophical Transactions. Series A, Mathematical, Physical, and Engineering Sciences,* 367, 1631–1672.

[93] R. Gittens and L. Scheideler. (2014) A review on the wettability of dental implant surfaces: Biological and clinical aspects. *Acta Biomaterialia,* 10, 2907-2918.

[94] X. Zhang, L. Wang and E. Levanen. (2013) Superhydrophobic surface for the reduction of bacterial adhesion. *RSC Advances,* 3, 12003-12020.

[95] Z. She, Q. Li, Z. Wang, L. Li, F. Chen and J. Zhou. (2013) Research the fabrication of anticorrosion superhydrophobic surface on magnesium alloy and its mechanical stability and durability. *Chemical Engineering Journal,* 228, 415-424.

[96] C. Vasak, D. Busenlechner, U. Schwarze, H. Leitner, F. Guzon, T. Hefti, F. Schlottig and R. Gruber. (2014) Early bone apposition to hydrophilic and hydrophobic titanium implant surfaces: a histologic and histomorphometric study in minipigs.*Clinical Oral Implants Research,* 25, 1378-1385.

[97] L. Freschauf, J. Mclane, H. Sharma and M. Khine. (2012) Shrink-induced surperhydrophobic and antibacterial surfaces in consumer plastics. *PLOS One,* 7, e40987.

[98] T. An, S. Cho, W. Choi, J. Kim, S. Lim and G. Lim. (2011) Preparation of stable superhydrophobic mesh with a biomimetichierarchical structure. *Soft Matter,*7, 9867-9870.

[99] L. Huang, S. Lau, H. Yang, E. Leong and S. Yu. (2005) Stable superhydrophobic surface via carbon nanotubescoated with a ZnO thin film. *The Journal of Physical Chemistry B,* 109, 7746-7748.

[100] T. Yanagisawa, A. Nakajima, M. Sakai, Y. Kameshima and K. Okada. (2008) Preparation and abrasion resistance of transparent super-hydrophobic coating by combining crater-like silica films with acicular boehmite powder. *Materials Science and Engineering B,* 161, 36-39.

[101] F. Shi, Y. Song, J. Niu, X. Xia, Z. Wang and X. Zhang. (2006) Facile method to fabricate a large-scale superhydrophobic surface by galvanic cell reaction. *Chemistry of Materials,* 18, 1365-1368.

[102] B. Qian and Z. Shen. (2005) Fabrication of superhydrophobic surfaces by dislocation-selective chemical etching on aluminum, copper, andzinc substrates. *Langmuir,* 21, 9007-9009.

[103] E. Hosono, S. Fujihara, Itaru Honma and H, Zhou. (2005) Superhydrophobic perpendicular nanopin film bythe bottom-up process. *Journal of the American Chemical Society,* 127, 13458-13459.

[104] L. Zhu, Y. Xiu, J. Xu, P. Tamirisa, D. Hess and C. Wong. (2005) Superhydrophobicity on two-tier rough surfaces fabricatedby controlled growth of aligned carbon nanotube arrays coated with fluorocarbon. *Langmuir,* 21, 11208-11212.

[105] N. Shirtcliffe, G. McHale, M. Newton and C. Perry. (2005) Wetting and wetting transitions on copper-basedsuper-hydrophobic surfaces. *Langmuir,* 21, 937-943.

[106] Z. Guo, J. Fang, J. Hao, Y. Liang and W. Liu. (2006) A novel approach to stable superhydrophobic surfaces. *ChemPhysChem,* 7, 1674-1677.

[107] Y. Liu, X. Yin, J. Zhang, S. Yu, Z. Han and L. Ren. (2014) A electro-deposition process for fabrication of biomimetic super-hydrophobic surface and its corrosion resistance on magnesium alloy. *Electrochimica Acta,* 125, 395-403.

[108] M. Yoldi, J. Garcia, R. Rodriguez, A. Martinez and M. Rico. (2010) Fabrication of superhydrophobic nanostructured films by physical vapour deposition. *Nanotechnology,* 600-603.

[109] D. Wu, Q. Chen, J. Yao, Y. Guan, C. Wang, J. Niu and H. Sun. (2010) A simple strategy to realize biomimetic surfaces withcontrolled anisotropic wetting. *Applied Physics Letters,* 96, 053704.

[110] B. Raeymaekers, I. Etsion and F. Talke. (2007) A model for magnetic tape/guide friction reduction by laser surface texturing. *Tribology Letters,* 28, 9-17.

[111] X. Wang, J. Wang, B. Zhang and W. (2015) Huang. Design principles for the area density of dimple patterns. *Journal of Engineering Tribology,* 229, 538-546.

[112] M. Duarte, A. Lasagni, R. Giovanelli, J. Louis and F. Mucklich. (2008) Increasing lubricant film lifetime by grooving periodical patterns using laser interference metallurgy. *Advanced Engineering Materials,* 10, 554-558.

[113] M. Wakuda, Y. Yamauchi, S. Kanzaki and Y. Yasuda. (2003) Effect of surface texturing on friction reduction between ceramic and steel materials under lubricated sliding contact. *Wear,* 254, 356-63.

[114] M. Khruschov and M. Babichev. Resistance to abrasive wear and the hardness of metals. 1953

[115] H. Archard. (1953) Contact and rubbing of flat surface. *Journal of Applied Physics,* 24, 981-988.

[116] T. Hu and L. Hu. (2012) The study of tribological properties of laser-textured surface of 2024 aluminium alloy under boundary lubrication. *Lubrication Science,* 24, 84-93.

[117] F. Wataria, A. Yokoyamaa, M. Omorib, T. Hiraic, H. Kondoa, M. Uoa and T. Kawasakia. (2004) Biocompatibility of materials and development to functionallygraded implant for bio-medical application. *Composites Science and Technology,* 64, 893-908.

[118] L. Gao, P. Yang, I. Dymond, J. Fisher and Z. Jin. (2010) Effect of surface texturing on the elastohydro dynamic lubrication analysis of metal-on-metal hip implants. *Tribology International,* 43,1851-60.

[119] H. Zhang, L. Qin, M. Hua, G. Dong and K. Chin. (2015) A tribological study of the petaloid surface texturing for Co–Cr–Mo alloy artificial joints. *Applied*

Surface Science, 332, 557-64.

[120] H. Ito, K. Kaneda, T. Yuhta and T. Nishimura. (2000) Reduction of polyethylene wear by concave dimples on the frictional surface in artificial hip joints. *The Journal of Arthroplasty,* 15, 332-338.

[121] T. Roy, D. Choudhury, S. Ghosh, B. Mamat. (2015) Improved friction and wear performance of micro dimpled ceramic-on-ceramic interface for hip joint arthroplasty. *Ceramics International,* 41, 681-690.

[122] D. Choudhury, H. Ching, A. Mamat, J. Cizek, N. Osman, M. Vrbka, M. Hartl, I. Krupka. (2014) Fabrication and characterization of DLC coated micro dimples on hip prosthesis heads. *Journal of Biomedical Materials Research,* 103, 1002-1012.

[123] A. Mallik, S. Shivashanka, and S. Biswas. (2009) Highvacuum tribology of polycrystalline diamond coatings. *Sadhana,*34, 811-821

[124] A. Simoes. (2008) Tribological properties of CVD diamond coated ceramic surfaces. *PhD Thesis, University of Minho, Portugal.*

[125] A. Amanov, R. Tsuboi, H. Oe, and S. Sasaki. (2013) The influence of bulges produced by laser surface texturing on the sliding friction and wear behavior. *Tribology International,* 60, 216-223.

[126] X. Jia, S. Jung, W Haas, and R. Salant. (2011) Numerical simulationand experimental study of shaft pumping by laserstructured shafts with rotary lip seals. *Tribology International,* 44, 651-659.

[127] H. Yamakiri, S. Sasaki, T. Kurita, and N. Kasashima. (2011) Effects of lasersurface texturing on friction behavior of silicon nitrideunder lubrication with water. *Tribology International,* 44, 579-584.

[128] Y Gao, B Wu, Y Zhou, and S. Tao. (2011) A two-step nanosecond laser surface texturing process with smooth surfacefinish. *Applied Surface Science,* 257, 9960-9967.

[129] C. Pypen, H. Plenk, M. Ebel, R. Svagera and J. Wernisch. (1997) Characterization of microblasted and reactive ion etched surfaces on the commercially pure metals niobium, tantalum and titanium. *Journal of Material Science. Materials in Medicine,* 8, 781-4.

[130] A. Gaggl, G. Schultes, W. Muller and H. Karcher. (2000) Scanning electron microscopical analysis of laser-treated titanium implant surfaces: a comparative study. *Biomaterials,* 21, 1067-73.

[131] F. Intranuovo, P. Favia, E. Sardella, C. Ingrosso, M. Nardulli, R. Agostino, R. Gristina. (2011) Osteoblast-like cell behavior on plasma deposited micro/nanopatterned coatings. *Biomacromolecules,* 12, 380-387.

[132] S. Kumar and S. Sen. (2014) Wear and friction in journal bearing: a review. *International Journal of Engineering and Management Research,* 4, 250-263.

[133] S. Bauer, P. Schmuki, K. Mark and J. Park. (2013) Engineering biocompatible implant surfaces Part I: *Materials and surfaces. Progress in Materials Science,* 58, 261-326.

[134] E. Burger and J. Klein-nulend. (1999) Mechanotransduction in bone-role of the lacunocanalicular network. *The FASEB Journal,* 13, 101-112.

[135] C. Yan, L. Hao, A. Hussein and P. Young. (2015) Ti–6Al–4V triply periodic minimal surface structures for bone implants fabricated via selective laser melting. *Journal of the Mechanical Behavior of Biomedical Materials,* 51, 61-73.

[136] D. Oliveira, A. Palmieri, F. Carinci and C. Bolfarini. (2015) Gene expression of human osteoblasts cells on chemically treatedsurfaces of Ti–6Al–4V–ELI. *Materials Science and Engineering C,* 51, 248-255.

[137] R. Kumari, T. Scharnweber, W. Pfleging, H. Besser and J. Majumdar. (2015) Laser surface textured Titanium alloy (Ti-6Al-4V)-part II-Studies on bio-compatibity. *Applied Surface Science,* 357, 750-758.

[138] W. Soboyejo, B. Nemetski, S. Allameh, N. Marcantonio, C. Mercer and J.

Ricci. (2002) Interactions between mc3t3-e1 cells and textured Ti-6Al-4V surfaces. *Journal of Biomedical Materials Research,* 62, 56-72.

[139] E. DeGarmo, J. Black, R. Kohser and B. Klamecki. (2003) Materials and process in manufacturing. *Wiley & Sons Inc*.

[140] D. Pioletti. (2013) Integration of mechanotransduction concepts in bone tissue engineering. *Computer Methods in Biomechanics and Biomedical Engineering,* 16, 1050-1055.

[141] A. Maniotis, C. Chen and D. Ingber. (1997) Demonstration of mechanical connections between integrins, cytoskeletal filaments, and nucleoplasm that stabilizenuclear structure. *Cell Biology,* 94, 849-854.

[142] X. Walboomers, W. Monaghan, A. Curtis, J. Jansen. (1999) Attachment of fibroblasts on smooth and micro grooved polystyrene. *Journal of Biomedical Material Research,* 55, 212-220.

[143] G. Schneider, H. Perinpanayagam, M. Clegg, R. Zaharias, D. Seabold, J. Keller, C. Stanford. (2003) Implant surface roughness affects osteoblast gene expression. *Journal of dental research,* 82, 372-376.

[144] M. Kantlehner, P. Schaffner, D. Finsinger, J. Meyer, A. Jonczyk, B. Diefenbach, B. Nies, G. Hölzemann, S. Goodman and H. Kessler.(2000) Surface coating with cyclic RGD peptides stimulates osteoblast adhesion and proliferation as well as bone formation. *Chembiochem,* 1, 107-114.

[145] M. Ball, D. Grant, W. Lo, C. Scotchford. (2007) The effect of different surface morphology and roughnesson osteoblast-like cells. *Journal of Biomedical Materials Research Part A,* 86A, 637-647.

[146] O. Rivera-Denizard, N. Diffoot-Carlo, V. Navas, P. Sundaram. (2007) Biocompatibility studies of humanfetal osteoblast cells culturedon gamma titanium aluminide. *Journal of Materials Science Materials in Medicine,* 19 153-158.

[147] J. Chen, S. Mwenifumbo, C. Langhammer, J. McGovern, M. Li, A. Beye and

W. Soboyejo. (2007) Cell/surface interactions and adhesion on Ti-6Al-4V: effectsof surface texture. *Journal of Biomedical Materials Research Part B: Applied Biomaterials,* 82, 360-373.

[148] J. Havlikova, J. Strasky, M. Vandrovcova, P. Harcuba, M. Mhaede, M. Janecek, L. Bacakova. (2014) Innovative surface modification of Ti–6Al–4V alloy with a positive effecton osteoblast proliferation and fatigue performance. *Materials Science and Engineering C,* 39, 371-379.

[149] M. Dalby, M. Riehle, D. Sutherland, H. Agheli and A. Curtis. (2003) Fibroblast response to a controlled nano environment produced by colloidal lithography. *Journal of Biomedical Materials Research Part A,* 69A, 314-322.

[150] K. Matsuzaka, M. Yoshinari, M. Shimono and T. Inoue. (2004) Effects of multigrooved surfaces on osteoblast-like cells in vitro: Scanning electron microscopic observation and mRNA expression of osteopontin and osteocalcin. *Journal of Biomedical Materials Research Part A,* 68, 227-234.

[151] W. Meng, Y. Zhou, Y. Zhang, Q. Cai, L. Yang, J. Zhao and C. Li. (2011) Osteoblast behavior on hierarchical micro-/nano-structured titanium surface. *Journal of Bionic Engineering,* 8, 234-241.

[152] H. Li, S. Yu, X. Han, S. Zhang and Y. Zhao. (2016) A simple method for fabrication of bionic superhydrophobic zinc coating with crater-like structures on steel substrate. *Journal of Bionic Engineering*, 13, 622-630.

[153] W. Li, Z. Wang, D. Wang, Z. Zhang, L. Zhao, D. Li, R. Qiu and C. Maple. (2014) Superhydrophobic dual micro- and nanostructures fabricated by direct laser interference lithography. *Optical Engineering,* 53, 034109-1-034109-6.

[154] B. Kim, S. Seo, K. Bae, D. Kim, C. Baek and H. Kim. (2013) Stable superhydrophobic Si surface produced by using reactive ion etching process combined with hrdrophobic coatings. *Surface & Coatings Technology,* 232, 928-935.

[155] M. Kafshgari, N. Voelcker and F. Harding. (2015) Applications of zero-valent

silicon nanostructures in biomedicine. *Nanomedicine,* 10, 2553-2571.

[156] X. Wei， W. Li, B. Liang, B. Li, J. Zhang, and Z. Wang. (2016) Surface modification of Co-Cr-Mo implant alloy by laser interference lithography. *Tribology International,* 97, 212-217.

[157] Y. Hu, Z. Wang, Z. Weng, M. Yu, and D. Wang. (2016) Bio-inspired hierarchical patterning of silicon by laser interference lithography. *Applied Optics,*5, 3226-3232.

[158] Q. Liu, W. Li, B. Liang, L. Cao, J. Wang, Y. Qv, X. Wang, J. Yan, Z. Wang, X. Di and R. Qiu. (2016) Ti-6Al-4V Alloy modification by laser interference lithography. *Proceeding of IEEE 3M-NANO2016*.

[159] D. Wang, Z. Wang, Z. Zhang, Y. Yue, D. Li, and C. Maple. (2013) Direct modification of silicon surface by nanosecond laser interference lithography. *Applied Surface Science,* 282, 67-72.

[160] T. Tavera, N. Perez, A. Rodriguez, P. Yurrita, S. Olazola and E. Castano. (2011) Periodic patterning of silicon by direct nanosecondlaser interference ablation. *Applied Surface Science,* 258, 1175-1180.

[161] B. Chichkov, C. Momma, S. Nolte, F. Alvensleben and A.Tünnermann. (1996) Femtosecond, picoseconds and nanosecond laser ablation of solids. *Applied Physics A,*63, 109-15.

[162] E. Gualtieri, A. Borghi, L. Calabri, N. Pugno and S. Valeri. (2009) Increasing nano hardness and reducing friction of nitride steel by laser surface texturing.*Tribology International,* 42, 699-705.

[163] M. Furukawa, Z. Horita, M. Nemoto, R. Valiev and T. Langdon. (1996) Micro hardness measurements and the Hall–Petch relationship in an Al–Mg alloy with sub- micro meter grain size. *ActaMater,* 44, 4619-29.

[164] P. Bazarnik, Y. Huang, M. Lewandowska and T. Langdon. (2015) Structural impact on the Hall-Petch relationship in an Al–5Mg alloy processed by

high-pressure torsion. *Materials Science and Engineering: A,* 626, 9-15.

[165] K. Anselme, P. Davidson, A. Popa, M. Giazzon, M. Liley and L. Ploux. (2010) The interaction of cells and bacteria with surfaces structured at the nanometre scale. *Acta Biomaterialia,* 6, 3824-3846.

[166] S. Bagherifard, D. Hickey, A. Luca, V. Malheiro, A. Markaki, M. Guagliano and T. Webster. (2015) The influence of nanostructured features on bacterial adhesion andbone cell functions on severely shot peened 316L stainless steel. *Biomaterials,* 73, 185-197.

[167] P. Lucker, S. Javaherian, J. Soleas, D. Halverson, P. Zandstra and A. McGuigan. (2014) A microgroove patterned multiwall cell culture plate for high-throughput studies of cell alignment. *Biotechnology and Bioengineering,* 111, 2537-2548.

[168] L. Qin, Q. Zeng, W. Wang, Y. Zhang, G. Dong. (2013) Response of MC3T3-E1 osteoblast cells to the microenvironmentproduced on Co–Cr–Mo alloy using laser surface texturing. *Journal of Material Science,* 49, 2662-2671.

[169] K. Popat, K. Chatvanichkul, G. Barnes, J. Latempa, C. Grimes and T. Desai. (2007) Osteogenic differentiation of marrow stromal cellscultured on nanoporous alumina surfaces. *Journal of Biomedical Materials Research Part A,* 80, 955-964.

[170] T. Schmalzried, L. Kwong, M. Jasty, R. Sedlacek, T. Haire, D. Connor, C. Bragdon, J. Kabo, A. Malcolm and W. Harris. (1992) The mechanism of loosening of cemented acetabular componentsin total hip arthroplasty. Analysis of specimens retrieved atautopsy. *Clinical Orthopaedics,* 274, 60-64.

[171] J. Bobyn, J. Jacobs, M. Tanzer, R. Urban, R. Aribindi, D. Sumner, T. Turner and C. Brooks. (1995) The susceptibility of smooth implantsurfaces to peri-implant fibrosis and migration of polyethylenewear debris. *Clinical Orthopaedics,* 311, 21-39.

[172] P. Clark, P. Connolly, A. Curtis, J. Dow and C. Wilkinson. (1987) Topographical control of cell behavior. I. Simple stepcues. *Development,* 99, 439-448.

[173] Q. Liu, W. Li, L. Cao, J. Wang, Y. Qu, X. Wang, R. Qiu, X. Di, Z. Wang and B. Liang. (2017) Response of MG63 osteoblast cells to surface modification of Ti-6Al-4V implant alloy by laser interference lithography, *Journal of Bionic Engineering,* 14, 448-458.

[174] X. Wei, B. Li, Z. Wang and W. Li. (2015) Reducing friction of an artificial hip joint by laser surface texturing, *Proc. 3M-NANO 2015*, 282-285.

[175] B. Li, X. Wei, X. Di, L. Zhang, Z. Wang and W. Li. (2015) Effects of laser interference parameters on surface modification of Co-Cr-Mo implant alloy, *Proc. 3M-NANO 2015*, 325-328.